ABSTRACT

Title of dissertation: PANDAX-II DARK MATTER DETECTOR AND ITS FIRST RESULTS

Andi Tan
Doctor of Philosophy, 2019

Dissertation directed by: Professor Xiangdong Ji
Department of Physics

The particle physics nature of dark matter (DM) is one of the most fundamental scientific questions nowadays. The leading candidates, weakly interacting massive particles (WIMPs), can be directly detected by looking for WIMP-nucleus scattering events in deep underground laboratories. Since the 1980s, physicists have improved the sensitivity of direct DM detection by about seven orders of magnitude. In the last decades, dual-phase xenon detectors exhibit their advantages in background rejection and scalability and lead the sensitivity in high mass WIMP direct searches. Experiments in XENON and LUX projects have been continuously pushing the exclusion limits of the elastic WIMP-nucleon scattering cross section into the parameter space predicted by various theoretical models.

The Particle and astrophysical Xenon (PandaX) project is a series of xenon-based ultra-low background experiments in the China Jinping Underground Laboratory (CJPL) targeting the unknown physics of DM. The first stage of the project, the PandaX-I experiment, with a 120 kg sensitive liquid xenon (LXe) target, performed

the WIMP search in 2014 with a 54×80.1 kg-day exposure. PandaX-I reported a strong limit on the WIMP-nucleon cross section for a WIMP mass of less than 10 GeV/c^2, strongly disfavoring all positive claims from other experiments.

The construction and installation of the second stage, PandaX-II experiment, with a half-ton scale LXe target, commenced after PandaX-I. In 2015, PandaX-II reported a WIMP search result with a 306×19.1 kg-day exposure from a short physics commissioning run with a notable ^{85}Kr background. With 580 kg LXe in the sensitive region, PandaX-II was the largest running dual-phase xenon detector before the XENON1T detector in 2017. PandaX-II reported the most stringent limit on the WIMP-nucleon scattering cross section at 2.5×10^{-46} cm^2 for the WIMP mass 40 GeV/c^2 with a total exposure of 33 ton-day in 2016 and updated the limit to 8.6×10^{-47} in 2017 with a total exposure of 54 ton-day. In this dissertation, I will focus on the PandaX-II experiment, data analysis and its constraints on theoretical models.

After a distillation campaign for krypton removal in 2017, the PandaX-II experiment achieved a background level of 0.8×10^{-3} event/kg/day/keV which was the lowest among similar detectors at the time. Compared to other dual-phase xenon detectors, we drift electrons by applying bias voltages on the electrodes which producing a stronger uniform electric field at a strength about 400 V/cm. After running for more than three years, more than 97% of 110 3″ photomultiplier tubes (PMTs) perform stably.

The analysis processes are continuously improved in various run periods in PandaX-II. The recorded waveforms were processed using a custom-developed soft-

ware through several steps including hit finding and calculation, signal clustering, and so on to the final pairing analysis of scintillation and ionization signals. In this dissertation, I shall cover some topics in these steps as following. The amplification factors (gains) of the PMTs are calibrated using Light Emitting Diode (LED) light periodically for transforming the recorded waveform to the number of photon electrons (PE) and energy. An inefficiency raised from zero length encoding (ZLE), a data suppression firmware of the data acquisition system, is investigated in run periods with relatively low PMT gain. A data-driven algorithm is developed for the X-Y position reconstruction using the hit pattern of the proportional scintillation on the top PMT array. The mono-energetic events from xenon isotopes are studied to correct the non-uniformity of the detector response, and key parameters are extracted to reconstruct the deposited energy of events. The background analysis is critical for rare-event search experiments. I will present the study on the intrinsic electron recoil backgrounds from krypton, radon and xenon isotopes. The constraints of PandaX-II data on various theoretical models are investigated.

PANDAX-II DARK MATTER DETECTOR AND ITS FIRST RESULTS

by

Andi Tan

Dissertation submitted to the Faculty of the Graduate School of the
University of Maryland, College Park in partial fulfillment
of the requirements for the degree of
Doctor of Philosophy
2019

Advisory Committee:
Professor Carter Hall, Chair
Professor Zackaria Chacko
Professor Xiangdong Ji, Advisor
Professor Eun-Suk Seo
Professor Da-lin Zhang

Acknowledgments

I am so fortunate to have a graduate experience at the University of Maryland and with the PandaX Collaboration. I owe my deepest gratitude to all the people who have guided and supported my research and made this dissertation possible.

First and foremost, I would like to thank my advisor, Professor Xiangdong Ji, for giving me a precious opportunity to work on such an exciting and challenging project. I still remember the first time learning a paper sentence by sentence with him, the scenario that I held an ISO200 tube and he tightened clamp screws of flanges seven years ago when we first moved to the underground lab, and those enlightening words from him when I lost myself in frustration and trivial matters. He also encouraged me to bear the big picture of physics frontiers in mind all the time. Besides our close collaboration on scientific research, we share opinions on social science problems, culture, and life. It has been a great pleasure to work and learn from such an extraordinary individual.

I would also like to thank Professor Jianglai Liu at Shanghai Jiao Tong University. In 2015, we talked over the phone almost every night. Without his patience guidance and instructions, we won't be about to make the PandaX-II detector work. It is my fortune to learn both instrumentations and data analysis from Prof. Liu who is an excellent example of being an experimental physicist.

I would like to appreciate Professor Carter Hall, Professor Eun-Suk Seo, Professor Zackaria Chacko and Professor Da-lin Zhang for serving on my thesis committee and spending their time reviewing the manuscript.

I thank other collaborators with the PandaX experiment who have enriched my research experience in various aspects. I want to thank Dr. Mengjiao Xiao for setting the tone of the highest level of self-discipline, responsibility, commitment, and scientific spirit for other students in the PandaX-I experiment. In the early stages of the PandaX-II experiments, Dr. Xiang Xiao led the design of PandaX-II Time Projection Chamber (TPC) and provided invaluable advises for me on the design of feedthroughs. I want to thank Dr. Pengwei Xie and Dr. Chen Xun for their patience help on data analysis and software tools. Xiangyi Cui, Dr. Xiaopeng Zhou, Binbin Yan, and Qiuhong Wang deserved special mention. As the onsite team, we have overwhelmed setbacks and frustrations during the assembly and commissioning of the PandaX-II detector. It's a great honor working with them shoulder-by-shoulder, and our friendship is an enormous fortune to me. Dr. Li Zhao taught me so much about vacuum technology and cryogenic system. Dr. Tao Zhang provided much help on mechanical design and infrastructures.

Financial support from the University of Maryland is acknowledged for my experimental involvement. Support from the Department of Energy on a theoretical grant enables me to participate in the analysis and interpretation of PandaX-II data.

Lastly, I would like to acknowledge my family. My parents always inspired me to think about my dream career and lifestyle since high school. When I devoted myself to experimental physics, they supported me without any reservation. I could not imagine life without my wife, Dianna Liu. Her love never fades during the long-distance relationship period. Without their love and encouragement, this thesis will be an untouchable dream.

Table of Contents

List of Tables

List of Figures

List of Abbreviations

ADC	Analog Digital Converter
ADMX	Axion Dark Matter eXperiment
ALP	Axion Like Particle
AMS	Alpha Magnetic Spectrometer
ARGO-YBJ	the Yang-Ba-Jing Cosmic Ray Observatory
BAO	Baryon Acoustic Oscillations
BBN	Big Bang Nucleosynthesis
BUL	Boulby Underground Laboratory
CAST	CERN Axion Solar Telescope
CBRD	Compton scattering, Bremsstrahlung, Recombination and Deexcitation
CERN	Conseil Europeen pour la Recherche Nucleaire
CJPL	China Jinping Underground Laboratory
CMB	Cosmic Microwave Background
CoG	Center of Gravity
CP	Charge Parity
CY	Charge Yield
DAMPE	DArk Matter Particle Explore
DAQ	Data Acquisition
DM	Dark Matter
DPE	Double Photon Emission
EC	Electron Capture
EEE	Electron extraction efficiency
EFT	Effective Field Theory
FEA	Finite Element Analysis
FermiLAT	Fermi Large Area Telescope
FoS	Factor of Safety
FV	Fiducial Volume
GN_2	Gaseous Nitrogen
H.E.S.S.	High Energy Stereoscopic System
HV	High Voltage
IV	Inner Vessel

JINST	Journal of Instrumentation
LED	Light Emitting Diode
LET	Linear Energy Transfer
LHC	Large Hadron Collider
LN_2	Liquid Nitrogen
LNGS	Laboratori Nazionali del Gran Sasso
LSC	Laboratorio Subterraneo de Canfranc
LSM	Laboratoire Souterrain de Modane
LSP	Lightest Super Particle
LXe	Liquid Xenon
LY	Light Yield
MC	Monte Carlo
MSSM	Minimal Supersymmetric Standard Model
MWPC	Multi-Wire Proportional Chambers
PAMELA	Payload for Antimatter Matter Exploration and Light-nuclei
PAF	Photon Acceptance Function
PandaX	Particle and astrophysical Xenon
PDE	Photon Detection Efficiency
PDF	Probability Density Function
PE	Photon Electron
PEEK	Polyetheretherketone
PLB	Physics Letters B
PMT	Photo Multiplier Tube
ppb	parts per billion
ppm	parts per million
ppt	parts per trillion
PRD	Physical Review D
PRL	Physical Review Letters
PTFE	Polytetrafluoroethylene
PTR	Pulse Tube Refrigerator
QCD	Quantum Chromodynamics
SD	Spin Denpendent
SEG	Single Electron Gain
SI	Spin Indenpendent

SLPM	Standard Liter Per Minute
SM	Standard Model
SNOLab	Sudbury Neutrino Observatory Laboratory
SPE	Single Photon Electron
SURF	Sanford Underground Research Facility
SUSY	Supersymmetry
TBA	Top-Bottom Asymmetry
TPC	Time Projection Chamber
WMAP	Wilkinson Microwave Anisotropy Probe
WIMP	Weakly Interacting Massive Particle
Y2L	Yangyang Laboratory
ZLE	Zero Length Encoding
ΛCDM	Lambda-Cold Dark Matter

Chapter 1: Introduction

Dark Matter (DM) is one of the most important puzzles in physics today. As it usually told, the dark matter was proposed by Swiss astronomer Fritz Zwicky in 1933 [1]. In the 1970s, Vera Rubin and her colleagues established the flat galactic rotation curves indicating that most galaxies must contain more dark as visible mass. Since then a large amount of evidence supports the existence of DM from astrophysical and cosmological observations, such as large-scale structure, gravitational lensing, Bullet Cluster, cosmic microwave background (CMB) anisotropy, and Big Bang nucleosynthesis (BBN). In cosmology, the Lambda-Cold Dark Matter (ΛCDM) model is developed which provides the best description of the universe and its evolution. Today, the study of CMB [2] shows that our universe is made of 4.9% of ordinary matter, 26.2% dark matter and 68.8% dark energy. The history of the hypothesis of DM is evolving as people digging more early historical literature. The actual storyline is more complicated. The pioneering work of Kapteyn and Oort along with the key developments that took place from the 1930s to 1970s were systematically reviewed in [3].

Though we do not know what DM is made of, we know several properties of DM particles. Physicists have proposed many models as the DM candidates

such as Weakly Interacting Massive Particles (WIMPs), Axion, sterile neutrino. WIMPs are a generic class of DM candidates favored by many theoretical models. The measurement of the Milky Way's rotation curve indicates a constraint on the local DM density profile [4] and numbers of experiments are carried out or under construction to detect DM particle in different approaches.

In recent years, direct detection experiments using liquid xenon time projection chamber (TPC) are the most sensitive WIMP detectors especially for WIMP mass over 10 GeV/c^2. The monolithic detectors using liquid xenon TPC are scalable to a larger mass and reducing the instrumental background simultaneously. Among various targets as the detector medium, xenon has a massive nucleus, and it is an efficient scintillator. It produces signals in multiple channels, i.e., photons, electrons, and heat. Excellent self-shielding and its stable isotopes make it an excellent medium for rare event search experiments for background rejection. The dual-phase TPCs collect two channels of signals, i.e., light and charge. The time and space profile of two signals provides access to the three-dimensional position of each event which can be used to set a fiducial volume with a reduced instrumental background. In liquid xenon, the ratio between the two signals also depends on the interaction type, i.e., electron or nuclear recoils (ER or NR), which provide excellent suppression on the background since WIMPs produce NR signals and most backgrounds are ER.

In this chapter, I will discuss some evidence supporting the existence of DM and introduce some of the well-motivated candidates as the DM particles at first. I will describe the detection strategies of WIMPs including the collider, indirect and direct searches. The properties of xenon as the medium for direct detection exper-

iments will be discussed. Finally, I will introduce the principle of dual-phase TPC with its access to information of events allowing a strong background suppression.

1.1 Evidence for dark matter

Ample evidence from astrophysical and cosmological observations support the existence of DM. In this section, I will outline some of the most prominent cases including the galactic rotation curve problem, the large-scale structure of the universe, Bullet Cluster, and the power spectrum of CMB.

Galactic rotation curve

The mass of stars and galaxy mass distribution were obtained through astrophotometry traditionally, and the velocities of stars can be inferred using the redshift. A typical spiral galaxy will have the majority of mass in the center and starts moving around the center in elliptical orbits. Applying Newtonian dynamics, the starts' rotation velocity to radius relationship, namely the rotation curve, will fall as $1/\sqrt{r}$. The same feature holds for galaxy clusters. However, almost all galaxies and galaxy clusters have flat rotation curves. Fig 1.1 shows the observed rotation curve (black dots) of the spiral galaxy cluster NGC 6503 [5]. The dashed line is the rotation curve based on the visible mass of the galaxy "disk". The "gas" distribution can be measured by X-ray imaging and gives the rotation curve as shown by the light dashed line. In order to hold the cluster from falling apart, there has to be a third component dominated by "dark" matter, "halo" marked as the dash-dotted curve, which provided additional gravitational force. The total velocity curve com-

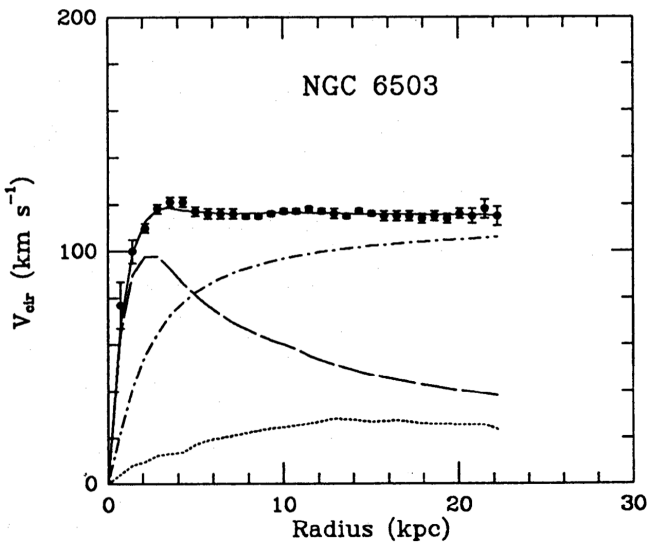

Figure 1.1: Rotation curve of NGC6503 [5]. See in the text for details.

bines disk, gas, and halo is labeled by the black curve, and it fits the observed data well.

Large-scale structure

The large-scale structure of the universe has been investigated in various redshift survey projects. They measure the three-dimensional distribution of matter by counting galaxy numbers per unit of solid angle in redshift bins [6]. One can observe a vast "foam-like" structure with alternative hierarchical concentrated and empty zones, known as walls, filaments, nodes, and voids.

On the other hand, high-resolution N-body simulations of the evolution of large-scale structure were performed for different flavors of DM. Relativistic and non-relativistic DM particles in the early universe result in different evolutionary histories. Non-baryonic hot, warm and cold DM were proposed with different velocity distributions. Cold DM does not dissolve the primordial density fluctuations

of baryonic matter and leads to a hierarchical structure formation [7] ,and it gives a consistent picture with the result of the redshift survey.

Bullet Cluster

The well-known Bullet cluster (1E 0657-56) refers to two colliding clusters of galaxies observed using optical and X-ray in 1998 [8]. Later in 2004, a weak lensing mass reconstruction indicates that the mass distribution of the DM is very different from the baryonic one from X-ray observation [9]. Fig 1.2 shows three layers of

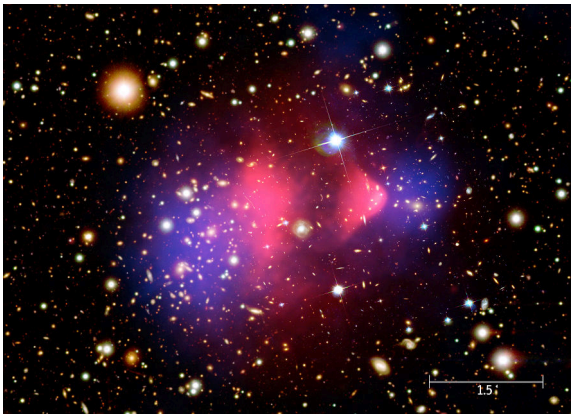

Figure 1.2: The Bullet cluster. Two clusters of galaxies are overlaid with the mass distributions from the X-ray and gravitational lensing effect.

the mass distribution. The optical galaxies were bright spots in the picture. The Chandra X-ray Observatory reconstructed the mass distribution of hot gas as shown in pink. The total mass of the hot gas was estimated to be ∼10 times more than galaxies. The gravitational lensing effect indicates an additional ∼70 times mass of galaxies other than the hot gas attributing to the DM shown in blue. Significant displacement of the baryonic and DM mass distribution was due to the difference in the interaction strength. The hot gas suffered stronger interaction and slowed down while the galaxies and DM passed each other without significant disruption. This

observation provides an upper limit on the self-interaction cross section [10]:

$$\frac{\sigma}{m} < 1\text{cm}^2/g \tag{1.1}$$

Cosmic microwave background (CMB)

CMB is the relic radiation at 380000 years after the big bang when the plasma of electron and proton cooled down into binding states and decoupled photons. This radiation then redshifted down to the microwave temperature as the expansion of the universe. Nowadays, the CMB is made up of photons as a black body with T = 2.7255K [2]. It is homogeneous and isotropic on a large scale. However, it has minute relic fluctuation from the early universe known as the CMB anisotropy. The best fit model of Plank 2018 gives the content of the universe which is consisting of 68.78% dark energy, 26.19% dark matter and 4.92% baryon matter.

1.2 Dark matter as WIMPs

Possible candidates for dark matter may be a new type or new types of elementary particles beyond SM. They are long-lived, and they do not involve in the electromagnetic or strong interaction. Neutrinos in SM (ν_e, ν_μ, and ν_τ) are particles meet those properties. However, neutrinos are moving too fast to enable the collapse of matter for structure formation. Relativistic particles, i.e., hot DM, are disfavored by the simulation. Moreover, the critical density of the total neutrino density is too small [2, 11]. Therefore, neutrinos are ruled out as dominating DM particles. There are many candidates proposed by particle physicists such as gravitinos, sterile neutrinos, neutralinos, axions, WIMPs. In this section, I will discuss briefly sterile

neutrinos, axions and, WIMPs below.

1.2.1 Sterile neutrino

The sterile neutrino was introduced to extend the SM in 1993 as a dark matter candidate [12]. These neutrinos are with right-handed chirality, and they do not directly interact with SM particles. However, they may mix with active neutrinos and can be detected indirectly. The mass of sterile neutrino can vary from 1 eV to 10^{15} GeV.

In May 2018, MiniBooNE (Mini Booster Neutrino Experiment) reported a stronger neutrino oscillation signal than expected [13]. The MiniBooNE data are consistent in energy and magnitude with the excess of events reported by the Liquid Scintillator Neutrino Detector (LSND) [14]. A two-neutrino oscillation interpretation of the data would require at least four neutrino types and indicate physics beyond the three-neutrino paradigm. Although the data are fit with a two-neutrino oscillation model, other models may provide better fits to the data. More efforts will be made to probe if the sterile neutrino is a dominating DM candidate [15].

1.2.2 Axion

Axion was proposed in 1978 [16, 17] as a solution to the strong Charge Parity (CP) problem in Quantum Chromodynamics (QCD) by the breaking of the Peccei-Quinn $U(1)$ symmetry [18]. Axion may have weak coupling to the photon, electron or nucleon. The coupling strength is model dependent. The sun is an active

source of axions in several ways, and various experiments were designed to search solar axions. Axions can be produced in the center of the sun by photons, and the coherent Primakoff effect can convert solar axions into photons in the detector. The coupling factor is denoted as $g_{A\gamma\gamma}$. Axions can be created in the sun through Compton scattering, Bremsstrahlung, Recombination, and Deexcitation (CBRD) mechanism (g_{Ae}) or with the ^{57}Fe excited state (g_{AN}). For more details, I refer to two review articles [19, 20].

Many experiments are aiming at hunting axions using different technologies including microwave resonance cavity, Telescope, Light-Shining-Through-Walls, and underground DM detectors [21]. The Axion Dark Matter eXperiment (ADMX) was carried out in 1995 to search for axion with microwave resonance cavity. Their new result reports the limit for dark matter axions with masses between 2.66 and 2.81 μeV and excludes the range of axion-photon couplings predicted by plausible models of the invisible axion [22]. CERN Axion Solar Telescope (CAST) uses a 9T refurbished Large Hadron Collider (LHC) test magnet directed towards the sun. In the strong magnetic field, solar axions can be converted to X-ray photons which can be recorded by X-ray detectors. Their recent results set the best limit on the axion-photon coupling strength 0.66×10^{-10} GeV^{-1} at a 95% confidence level [23]. Most underground DM detectors were designed for WIMPs search. However, they can be used for axion search as well. CDMS [24], XMASS [25], XENON100 [26], CDEX-1 [27], and LUX [28] all reported their results on axions coupling strength.

In 2017, the PandaX-II collaboration reported searches for solar axions and galactic ALPs using data with an exposure of about 27 ton-day [29]. No solar axion

or galactic ALP candidate has been identified. The upper limit on the axion-electron coupling (g_{Ae}) from the solar flux is found to be about 4.35×10^{-12} in the mass range from 10^{-5} to 1 keV/c^2 with a 90% confidence level. The best limit at the time from the ^{57}Fe-deexcitation was set as well [29]. On the other hand, the upper limit from the galactic axions is on the order of 10^{-13} in the mass range from 1 to 10 keV/c^2 with a 90% confidence level [29].

1.2.3 WIMPs

WIMPs are the most desirable candidates to explain the abundance of DM. The freeze-out mechanism predicts that WIMPs have mass and coupling strength with a similar strength of the weak interaction. Physicists designed many experiments to search for WIMPs.

The Minimal Supersymmetric Standard Model (MSSM) [30] introduces a discrete symmetry. The massive super particles may decay to lighter super particles that emit SM particles, and the lightest super particle (LSP) will be stable. The LSP is called Neutralino which is a mixture of super partners of Z-boson, photon and Higgs boson. Neutralino is a well-motivated WIMP candidate. Supersymmetry contains a vast catalog of specific models all involves numbers of free parameters. Different beyond SM theories predict various WIMP candidates such as lightest Kaluza-Klein particles from universal extra dimensions [31], little T-odd particles from little Higgs theory [32].

The WIMP freeze-out mechanism is proposed as an explanation of the abun-

dance of DM observed today [33–35]. In the early universe, the temperature is much higher than the WIMP mass ,and WIMPs were in thermal equilibrium with SM particles through a high rate of annihilation and production processes. The universe then cools to temperatures T below the mass of WIMPs. At low temperatures, the number density of DM particles would drop to zero, except that, in addition to cooling, the universe is also expanding. Eventually, the universe becomes so large, and the DM particles become so dilute that they cannot find each other to annihilate. The DM particles start to "freeze-out" when the annihilation rate is equal to the expansion constant. Their comoving number density is asymptotically approaching a constant, i.e., their thermal relic density. After thermal freeze-out, the density of DM particles approaches constant, but interactions that mediate energy exchange between dark matter and other particles may remain efficient. Measurements of CMB provide a density of cold DM [2] and requires the cross section of WIMP $\langle v\sigma_A \rangle$ is 2.5×10^{-26} cm^{3}s^{-1}, or 2.15×10^{-9} GeV^{-2}. This cross section is remarkably close to the cross section at the electroweak scale ($\sim 10^{-8}$ GeV^{-2}) and often called a WIMP miracle. The coincidence led many experiments to detect WIMPs.

Detection of WIMPs

There are three approaches to detect WIMPs as shown in Fig 1.3: production at colliders, indirect and direct detection. The collider physicists are trying to accelerate SM particles to very high energy and collide them. They are looking for any missing energy or momentum which may be taken away by WIMPs. The indirect search is looking for the excess of SM particles in the space which may be the product of DM annihilation. The direct detection is searching for the interaction between

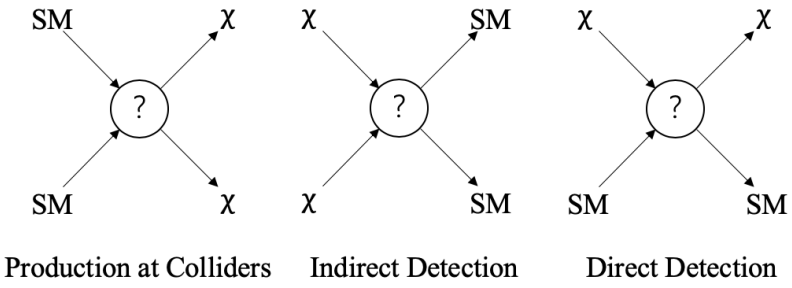

Figure 1.3: Three approaches to detect WIMPs: production at colliders, indirect and direct detection. "χ" stands for generic WIMPs and "SM" is any SM particle.

DM and SM particles. Fig 1.4 from [36] exhibits the distribution of terrestrial experiments for DM search. All three approaches are looking for events from rare

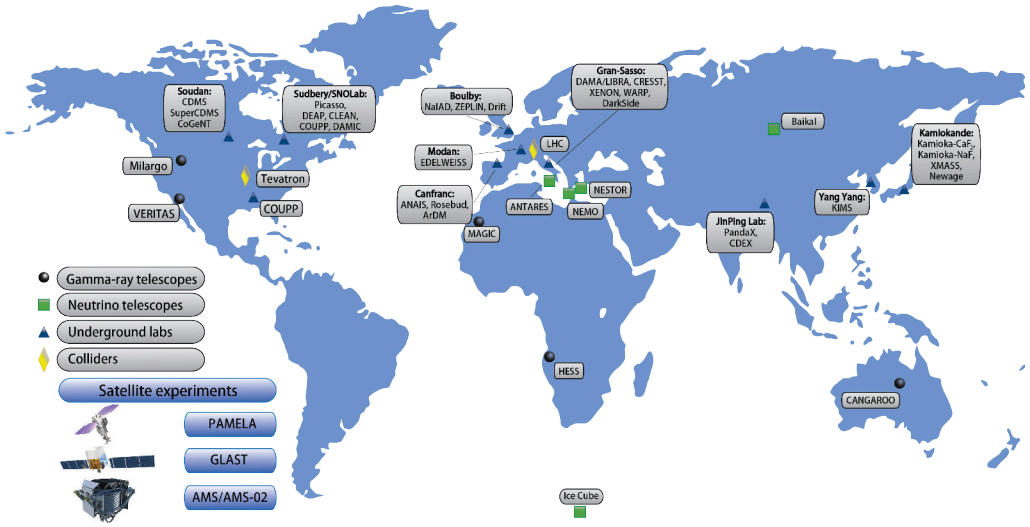

Figure 1.4: Geographical location of the terrestrial experimental sites hunting for DM [36]. Gamma-ray telescopes (black circle), neutrino telescopes (green box) - indirect searches, which have tried to catch some bumps in the SM particle spectrum in cosmic rays with ground-based or space observatories. The underground labs (magenta pyramid) - direct searches: DM-SM scattering, looking for the nuclear recoil from galactic DM scattering, due to weak signals the experiments are located deep underground. Colliders (yellow diamond) - production of the DM particles via SM interactions. Also, satellite experiments are shown, which continue to explore the nature of DM.

processes between DM and SM particles. If DM particles interact with SM particles other than the gravitational force, three methodes should observe consistent results.

Collider searches

The first approach to detect WIMPs is to collide high energy hadron beam and carefully counting the products looking for missing energy or momentum. LHC reached the energy level of 6.5 TeV per beam (13 TeV total) in 2015. Both ATLAS [37] and CMS [38] experiments carried out an analysis of collision products for the searches on DM in 2017 as shown in Fig 1.5. No significant excess over the expected background is observed. Collider search has better sensitivity in the low mass region.

DM density profile in the Milky Way

The knowledge of DM density profile in the Milky Way is essential for the design of indirect and direct search experiments. Indirect search on annihilation products will anticipate signals proportional to the square of the number density of DM particles. Indirect search which looking for decay products from DM particles and direct search will have signals proportional to the number density. The DM density profiles vary among different galaxies. As mentioned in Sec 1.1, there has to be a DM dominating halo to make the rotation curve flatten out at large radiuses r, and the halo density should obey:

$$\rho_\chi(r) \propto \frac{1}{r^2}, \tag{1.2}$$

at large r. In the center of the halo, the density must be finite, and it is crucial for indirect search. The Milky Way is a medium barred spiral galaxy of total mass about $10^{12} M_\odot$ and a diameter about 31 kpc. The solar system is located about 8 kpc to the galactic center. N-body simulation of DM halos from dwarf galaxies of

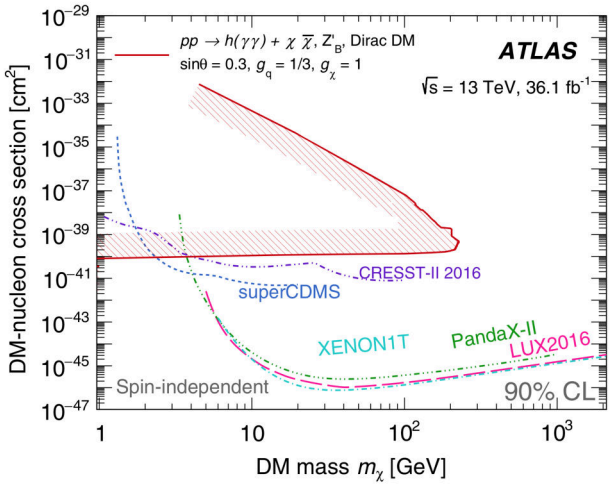

(a) ATLAS

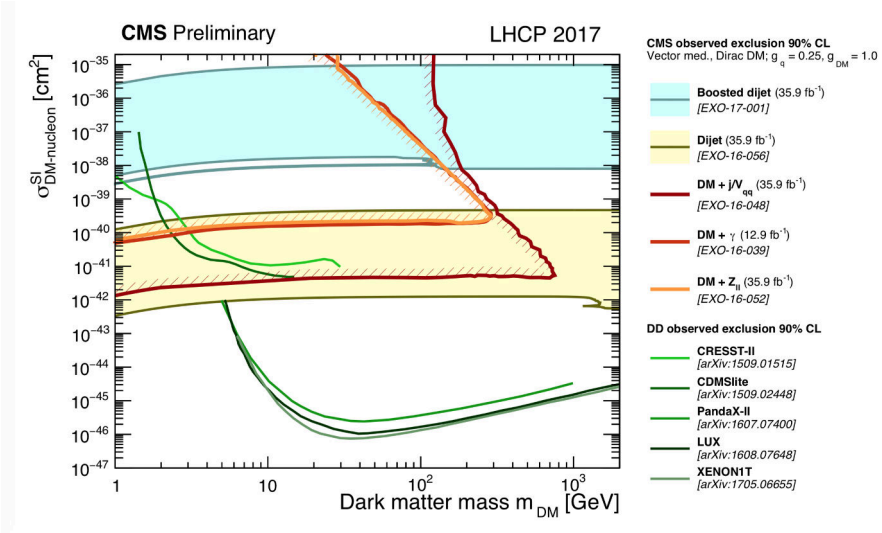

(b) CMS

Figure 1.5: Upper limits on WIMP-nucleon cross section from ATLAS (a) [37] and CMS (b) preliminary [38].

about $10^{11} M_\odot$ to galaxy clusters of about $10^{15} M_\odot$ has been fit well with analytical functions such as the NFW [39] and Einasto [40] profiles. Terrestrial and space telescopes like LAMOST [4] and Gaia [41] measured the rotation curve of the Milky Way. Using the NWF profile and ΛCDM model, LAMOST reported a local dark

matter density

$$\rho_{\chi,\odot} = 0.32 \pm 0.02 \text{ GeV/cm}^3. \tag{1.3}$$

Indirect searches

WIMPs can be detected indirectly via the products from their annihilation or decay, it.e. positrons, antiprotons, photons or neutrino. Worldwide experiments were carried out to search for these products from DM annihilation. Payload for Antimatter Matter Exploration and Light-nuclei (PAMELA) [42] and DArk Matter Particle Explore (DAMPE) [43] reported the spectrums of electrons and positions. Besides, Alpha Magnetic Spectrometer (AMS-02) [44–46] measured the spectrums of proton and antiproton as well. Fermi Large Area Telescope (FermiLAT) [47], High Energy Stereoscopic System (H.E.S.S.) [48] and the Yang-Ba-Jing Cosmic Ray Observatory (ARGO-YBJ) [49] detected the anomalous photon over the cosmic background. Moreover, IceCube [50] searched for neutrinos from decaying DM.

With the first 530 days of scientific observations in 2017, DAMPE detected about 1.5 million cosmic ray electrons and positrons in the energy range 25 GeV to 4.6 TeV with high energy resolution and low background. Fig 1.6 shows the corresponding high-energy cosmic-ray electrons and positrons spectrums measured from the DAMPE data. Previously published results from the space-borne experiments AMS-02 and Fermi-LAT, as well as the ground-based experiment of the H.E.S.S. collaboration, are overlaid. The spectrum reveals a spectral break at around 0.9 TeV and an excess at about 1.4 TeV. The 1.4 TeV excess stirred much interest in the explanations with DM annihilation [51, 52].

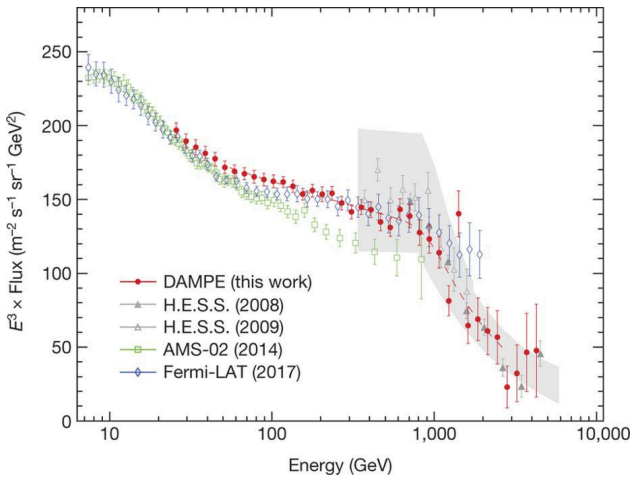

Figure 1.6: High-energy cosmic-ray electrons and positrons spectrums from the DAMPE data [43]. The red dashed line represents a smoothly broken power-law model that best fits the DAMPE data in the range 55 GeV to 2.63 TeV. Also shown are the direct measurements from AMS-02 and Fermi-LAT, and H.E.S.S. (the grey band represents its systematic errors apart from the approximately 15% energy scale uncertainty).

AMS-02 has reported data of position and antiproton with the largest statistics. They have found significant excesses to the known background on both spectra as shown in Fig 1.7. Many studies find indications of an excess of antiprotons that may correspond to a DM particle with a mass of several tens of GeV/c^2 [53, 54].

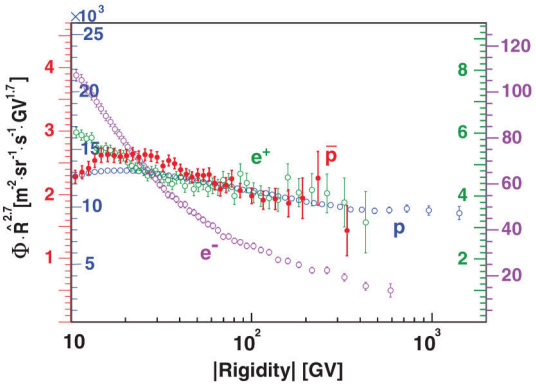

Figure 1.7: The measured antiproton flux (red, left axis) compared to the proton flux (blue, left axis), the electron flux (purple, right axis), and the positron flux (green, right axis) in AMS-02. All the fluxes are multiplied by $\hat{R}^{2.7}$.

In early 2019, AMS Collaboration studied the significant excess on the spectrum of 1.9 million positrons as shown in Fig 1.8 [55]. The high energies excess very likely originate either from dark matter annihilation or from other astrophysical sources.

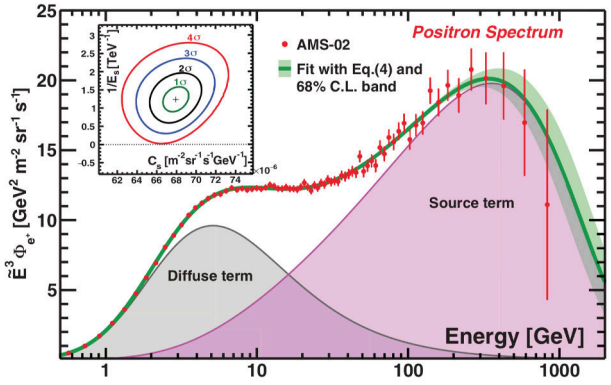

Figure 1.8: The fit of a diffusion and a source term to the positron flux in the energy range from 0.5 GeV to 1 TeV together with the 68% C.L. interval (green band) in AMS-02 [55]. The exponential cutoff of the source term is determined to be 810^{+310}_{-180} GeV from the fit. The red data points represent the measured positron flux values scaled by E^3. The source term contribution is represented by the magenta area and the diffuse term contribution by the gray area.

Let us quote from Ting's talk [56] to summarize the indirect detection:

To identify the Dark Matter signal we need more:

1. Measurement of e^+, e^- and $\bar{p}$.

2. Precise knowledge of the cosmic ray fluxes (such as p, He, C).

3. Propagation and Acceleration (such as Li, B/C).

1.3 Direct WIMP searches

DM particle may only have a very weak interaction with SM baryons besides their gravitational coupling. I refer to review articles for detailed discussion [57–59]. Direct search experiments detect such signals between DM and SM particles, i.e., atoms of the detection medium. More specifically, the nuclear recoils signal will be generated from the nucleus scattered off by DM particles [60]. WIMPs can in principle scatter off electrons, but the recoil energy would be much smaller due to the electron mass and hence would require a more sensitive detection technology [61]. The sensitivities of rare process search experiments such as WIMP direct detection rely on background suppression and large exposure.

Direct Detection Principle

Let us consider an elastic scattering with a recoil angle θ_r between a WIMP particle, χ of mass m_χ, and a nucleus with the number of nucleons A and mass m_A. The recoil energy of the target nucleus is given by:

$$E_r = \frac{4 m_\chi m_A}{(m_\chi + m_A)^2} \cos^2 \theta_r E_\chi. \tag{1.4}$$

The galactic rotation of the solar system dominates the relative velocity of χ to the detector (or target nucleus). The speed of the earth can be added on for annual modulation signal search. For simplicity, let us take v_χ to be about 220 km/s [62], i.e., v_χ/c is about 10^{-3}. From Eq 1.4, for a WIMP with $m_\chi = 100$ GeV, the maximum of the expected recoil energy will be about 100 keV when the target nucleus has similar mass.

The expected event rate R can be expressed in a differential form as:

$$\mathrm{d}R(t) = \frac{\rho_\chi}{m_\chi}\frac{v_\chi(t)}{m_A}\frac{\mathrm{d}\sigma(E_r)}{\mathrm{d}E_r}\mathrm{d}E_r f\Big(\vec{v}_\chi(t)\Big)\mathrm{d}^3v \tag{1.5}$$

where ρ_χ is the local DM density given in Eq 1.3, and $f\Big(\vec{v}_\chi(t)\Big)$ is the velocity distribution in the lab (earth) frame. One can consider $f(\vec{v}')$ to obey the Maxwellian distribution in the rest (galactic) frame of the Milky Way and take the vector sum of the motion of solar system $\vec{v}_\odot(t)$ and $\vec{v}'$. Note that $\vec{v}_\odot(t)$ contributes to the annual modulation signals but $\vec{v}_\odot(t) \ll \vec{v}'$. Besides, daily modulation signal can be added.

The differential cross-section term, $\mathrm{d}\sigma(E_r)/\mathrm{d}E_r$, can be written as the sum of a spin-independent (SI) and a spin-dependent (SD) contribution:

$$\frac{\mathrm{d}\sigma(E_r)}{\mathrm{d}E_r} = \frac{m_A}{2m^2v_\chi^2}\Big(\sigma_0^{\mathrm{SI}}F_{\mathrm{SI}}^2(E_r) + \sigma_0^{\mathrm{SD}}F_{\mathrm{SD}}^2(E_r)\Big) \tag{1.6}$$

where σ_0^{SI} and σ_0^{SD} are the cross-section at zero momentum transfer for SI and SD parts. $F_{\mathrm{SI}}(E_r)$ and $F_{\mathrm{SD}}(E_r)$ are the form factors for SI and SD parts respectively which normalized to unity at zero momentum transfer. For SI interaction, σ_0^{SI} can be expressed as:

$$\sigma_0^{\mathrm{SI}} \propto [Z\cdot f_{\mathrm{p}} + (A-Z)\cdot f_{\mathrm{n}}]^2 \tag{1.7}$$

where Z is the number of protons. f_{p} and f_{n} are the contributions of protons and neutrons respectively. The assumption of $f_{\mathrm{p}} = f_{\mathrm{n}}$ was adopted in most models. Therefore, the SI cross-section is proportional to A^2. On the other hand, the form factor is given in terms from nuclear shell model calculation for SD interaction [63,64] as:

$$\sigma_0^{\mathrm{SD}} \propto [\langle S_{\mathrm{p}}\rangle\cdot g_{\mathrm{p}} + \langle S_{\mathrm{n}}\rangle\cdot g_{\mathrm{n}}]^2\cdot\frac{J+1}{J} \tag{1.8}$$

where $\langle S_{\mathrm{p(n)}} \rangle$ is the expectation of the nuclear spin of proton (neutron) group, and $g_{\mathrm{p(n)}}$ is the coupling strength of proton (neutron). J is the total nuclear spin.

For a DM particle with mass m_χ, the direct detection experiments are expecting an energy spectrum in the form of:

$$\frac{\mathrm{d}R(E_r)}{\mathrm{d}E_r} \sim \mathrm{e}^{-E_r/E_0} F^2(E_r), \tag{1.9}$$

where E_0 is a characteristic energy scale depending on m_χ and target A.

Detection technologies

Nuclear and electrical recoil energy may deposit into three channels, photon (scintillation), phonon (heat), and electron (ionization). Experiments using different technologies can readout different channels of signals. The early solid-state experiments readout a single channel of signal such as germanium, silicon, and sodium iodide detectors. Later the cryogenic detector was designed to be able to read out two channels which improved the background suppression a lot by discrimination of the electronic recoil type signals. Recently, the cutting-edge detectors using dual-phase TPC on a large size to increase the probability of discovery with even stronger background rejection. Fig 1.9 summarized the categories of different detection technologies [58]. With the development of detection technologies, strong background reduction and larger exposure lead to an improvement of the sensitivity by about seven orders of magnitude in past decades (Fig 1.10).

Neutron may produce a similar nuclear recoil signal as the DM particle and become the background signal. Energetic neutron is a primary background source produced by the cosmic ray. Thus, all WIMP direct detection experiments are

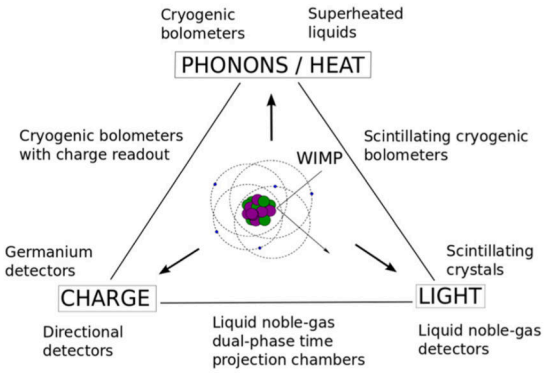

Figure 1.9: Illustration of dark matter detection technologies [58]. They are categorized based on the read-out signals. Representative experiments are listed.

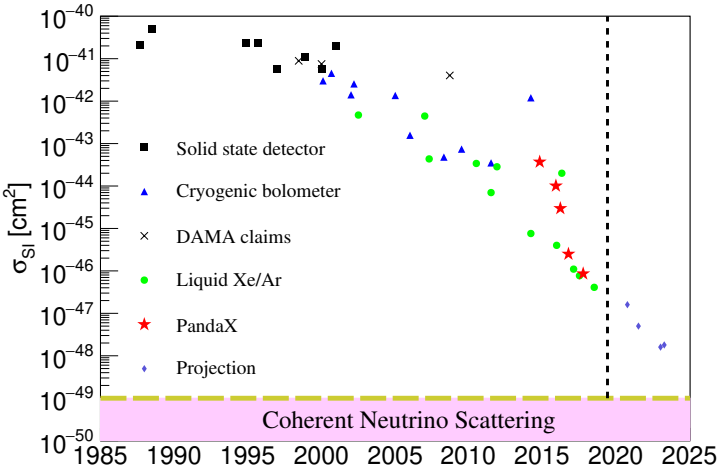

Figure 1.10: Evolution/projection of limits on the DM-nucleon SI cross section. Different shapes represent different technologies: solid state detectors (black square), cryogenic semiconductor detectors (blue triangles), and liquid noble gas detectors (green circles except that red starts for PandaX results). The claims from DAMA and DAMA/LIBRA are indicated in black crosses. The azure diamonds indicate the progression from PandaX-4T, XENONnT, and LZ. Most of the data are achieved from dmtools.brown.edu. The yellow dashed line is the coherent neutrino floor. Experiments using different targets and technologies may yield minimums of their limits at different masses.

conducted in the underground lab and further shield by ultra-pure materials or active veto detectors. We will discuss the underground laboratories in Sec 2.1.

As detectors get bigger and bigger, we may expect several events in a year from coherent neutrino scattering off the nucleons. Since it is almost impossible to shield and veto neutrinos, they are considered as the ultimate background in the dark matter direct search experiments [65]. It is called the coherent neutrino floor as indicated in Fig 1.10. New ideas exist to mitigate the neutrino background like directional detection [66].

1.4 Xenon as a detector medium

Xenon is widely used as a detector medium in particle physics, astrophysics, and medical imaging experiments and applications [67]. The development of technologies kept exploiting the advantage properties of xenon as a detector medium. In this section, I will summarize the related properties of xenon as a detector medium of a dark matter direct search experiment below.

1. Xenon has a large atomic number[1].

The average atomic number of xenon is large, $A_{\mathrm{Xe}} = 131.3$, compared with other popular target elements as detector mediums, $A_{\mathrm{He}} = 4.0$, $A_{\mathrm{Ne}} = 20.2$, $A_{\mathrm{Ar}} = 39.9$, $A_{\mathrm{Na}} = 23.0$, $A_{\mathrm{Ge}} = 72.6$, $A_{\mathrm{I}} = 126.9$ [68]. This average atomic number of xenon corresponding to about 120 GeV average nuclear mass as shown in Tab 1.1 [68, 69]. Recall the discussion of Eq 1.4, the WIMP particle χ may have model-depending mass and a typical mass with $m_\chi \sim 100$ GeV. Xenon as the target nucleus can achieve more considerable recoil energy for m_χ in the order of a few hundred GeV. As

[1]Data was acquired from `http://hyperphysics.phy-astr.gsu.edu/hbase/pertab/xe.html`

Table 1.1: The atomic number (A), nuclear mass (m_A in GeV), natural abundance (c), Spin (J), decay mode and half-life time (τ) of xenon isotopes. ε, β-, and 2β- stands for electron capture, beta, and double beta decay modes, respectively.

Isotope	A	m_A	c	J	Decay Mode	τ
^{124}Xe	123.9	115.4	0.001	0	Stable	-
^{125}Xe	124.9	116.3	syn	1/2	ε	16.9 h
^{126}Xe	125.9	117.3	0.0009	0	Stable	-
^{127}Xe	126.9	118.2	syn	1/2	ε	36.35 d
^{128}Xe	127.9	119.1	0.0191	0	Stable	-
^{129}Xe	128.9	120.0	0.264	1/2	Stable	-
^{130}Xe	129.9	120.9	0.041	0	Stable	-
^{131}Xe	130.9	121.9	0.212	3/2	Stable	-
^{132}Xe	131.9	122.8	0.269	0	Stable	-
^{133}Xe	132.9	123.8.4	syn	3/2	β-	5.25 d
^{134}Xe	133.9	124.7	0.104	0	Stable	-
^{136}Xe	135.9	126.6	0.089	0	2β-	2.2×10^{21} yr

mentioned above in Eq 1.7, the differential event rate at a small momentum transfer scenario takes the form of A^2, and the form factor takes care of the decoherence in the higher recoil energy. Xenon has a promising event rate in the low recoil energy region as shown in Fig 1.11 [58].

2. Xenon is an excellent medium for both SI and SD search.

Tab 1.1 enumerates the spin of the xenon isotopes as well. About half of natural xenon atoms are with an odd number of neutrons and are good target nucleus for SD χ-neutron interactions [64, 70]. Fig 1.12 from [70] calculated the differential nuclear recoil spectra of ^{129}Xe and ^{131}Xe, assuming "neutron-only" couplings. Both elastic and inelastic recoil spectra are shown for comparison.

3. Xenon has high signal yields.

Among various mediums, xenon is a very efficient scintillator with less quench-

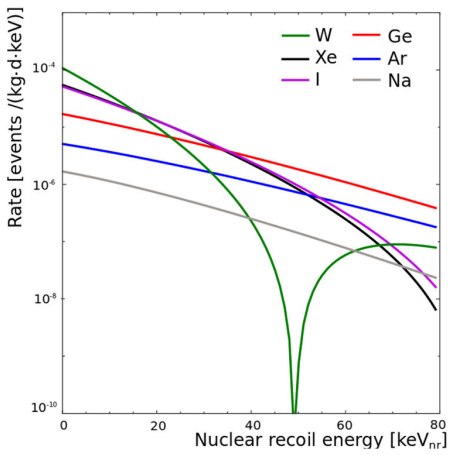

Figure 1.11: Differential event rate for the direct detection of a 100 GeV/c^2 WIMP with a cross-section of 10^{-45} cm^2 in experiments using tungsten (green), xenon (black), iodine (magenta), germanium (red), argon (blue) and sodium (grey) as target materials [58].

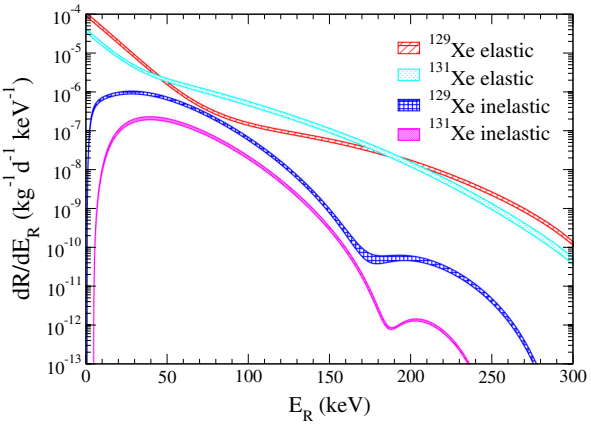

Figure 1.12: Differential nuclear recoil spectra $\mathrm{d}R/\mathrm{d}E_r$ as a function of recoil energy E_R for scattering off ^{129}Xe and ^{131}Xe, assuming "neutron-only" couplings of a 100 GeV WIMP with a WIMP-nucleon cross section $\sigma_{\mathrm{nucleon}} = 10^{-40}$ cm^2 [70].

ing effect than other noble gases and comparable scintillation efficiency to NaI (Tl) [71, 72] as shown in Fig 1.13 [73]. The scintillation yield often depends on the deposition type and deposition density of the incident particle and is characterized by Linear Energy Transfer (LET) and the W-value (work function of the medium).

On the other hand, the scintillation spectrum of xenon has the longest wave-

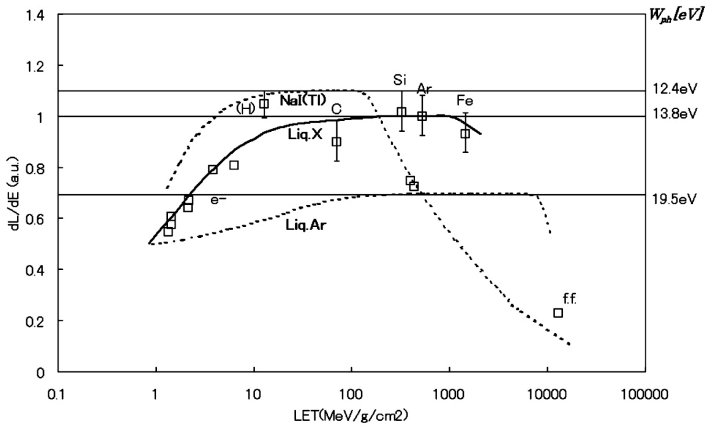

Figure 1.13: Three LET dependences of scintillation yield curves, the upper curve is that of NaI (Tl) crystal, the lower curve is liquid argon, and the middle curve is liquid xenon [73]. The abscissa on the right side shows the value of W_{ph}.

length centered at about 178 nm. Along with the development of low background PMT technologies, it allows photons from xenon to transmit through the PMT window and convert to photoelectrons. Fig 1.14 shows the scintillation spectrum of xenon (violet), krypton (blue), argon (azure) and helium (cyan) [74]. The quantum efficiency (red) combing the window transmission of Hamamatsu R11410 was overlaid in Fig 1.14 [75].

4. Xenon can be purified efficiently.

Noble gases are chemically stable which allows the development of chemical purification technology of noble gases. As shown in Fig 1.14, impurities like water (black dashed) and oxygen (gray dashed) have overlapped absorption spectra with the scintillation spectrum of xenon. The purification is needed to inhibit the attenuation of the scintillation signal. Besides, dual-phase TPC detectors measure the ionization signal with the scintillation signal at the same time. The electrons can attach to the electronegative impurities in xenon during the collection process. This

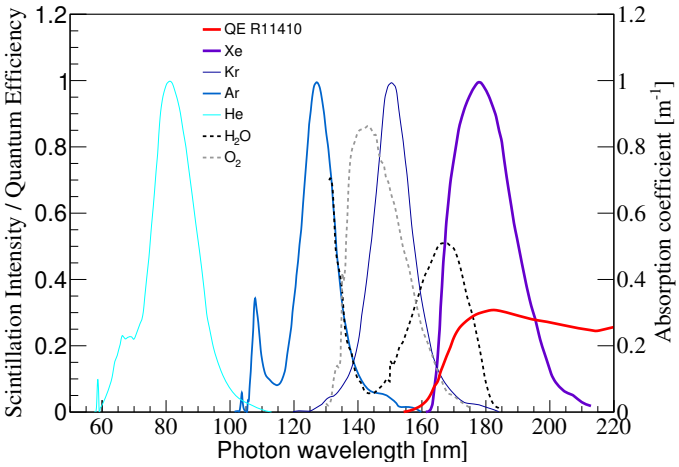

Figure 1.14: The scintillation spectrum of helium (cyan), argon (azure), krypton (blue), and xenon (violet) in 58 $\sim$ 200 nm wavelength region. Note that all curves have been normalized by making the maximum to 1. Therefore, the relative intensity only refers to each spectrum. Absorption coefficients for 1 part per million (ppm) water vapor (black dashed) and 1 ppm oxygen (gray dashed) are superimposed. The red curve is absolute QE measured at room temperature for Hamamatsu model R11410-10 PMT.

attenuation is often parametrized as the electron lifetime or attenuation length, or oxygen equivalent impurity concentration (Sec.II.C.7 in [67]). In PandaX-II, SAES hot zirconium getters (Model PS5-MGT50-R-909) are used to purify gaseous xenon [76] at about 50 Standard Liter Per Minute (SLPM). The electron lifetime was kept at about 1000 μs during the data taking period. By considering 1.7 mm/μs as the drifting velocity under the electric field of 320 V/cm in LXe, the attenuation length of the electron is about 1.7 m. The total impurity concentration (oxygen equivalent) is less than 1 parts per billion (ppb).

5. Xenon isotopes are stable.

Tab 1.1 summarizes the natural abundance (c), decay mode and half-life times of all xenon isotopes. Note that ^{125}Xe, ^{127}Xe, and ^{133}Xe are synthetic radioisotopes

with negligible abundance for rare production in natural process or short half-life time. ^{127}Xe has the longest half-life time among them and was present in the PandaX-II detector. It was produced by cosmogenic activation during the surface transportation of xenon via neutron capture of ^{126}Xe. Details about ^{127}Xe will be discussed later in analysis Sec 4.6.3. ^{136}Xe undergoes double beta decay to ^{136}Ba with a half-life time of $T_{1/2}^{2\nu\beta\beta} = 2.165 \pm 0.016\ (\text{stat}) \pm 0.059\ (\text{sys}) \times 10^{21}$ yr [77].

6. Liquid xenon is a good self-shielding material.

Radioactivities from instrumental materials produce backgrounds for WIMP detection. Various particles can create different types of energy deposition in liquid xenon such as α particle, electron, photon, and neutron. In most experiments, γ rays are the dominating instrumental background. There are three major types of interaction between photons (mainly γ) and matter as shown in Fig 1.15 [78]: photoelectric absorption (blue dashed line), Coherent and incoherent scattering (azure and green dashed lines) and Pair production (red and magenta dashed lines).

The mean free path of photon is a proper measurement for the self-shielding effect of the target medium to restrict the instrumental γ background from entering the centeral region of the detector. The energy dependence of the mean free path can be derived using the inverse mass attenuation coefficient divided by the density of the target medium. Fig 1.16 shows the photon mean free paths in three favorite target mediums for a WIMP search. The density of liquid argon and liquid xenon are pressure-dependent, and the calculation in Fig 1.16 takes the average operational density in WIMP search, i.e., 3.0 g/cm^3 for LXe and 1.4 g/cm^3 for LAr. Thus, xenon has an excellent self-shielding as a detector medium.

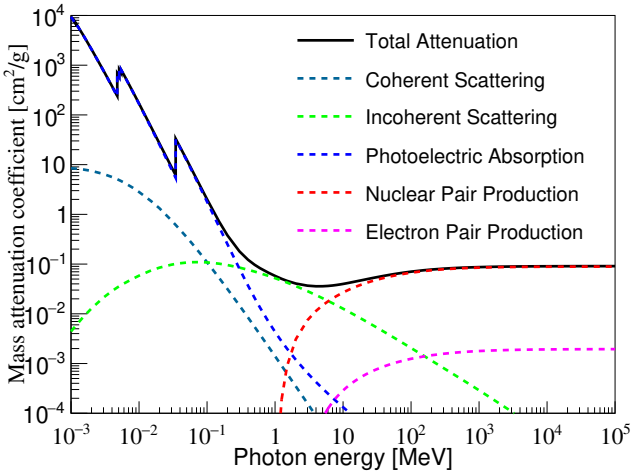

Figure 1.15: Mass attenuation coefficient of xenon (black curve). The contribution from coherent/incoherent scattering (azure/green dashed line), photoelectric absorption (blue dashed line), and nuclear/electron pair production (red/magenta dashed line) are overlaid.

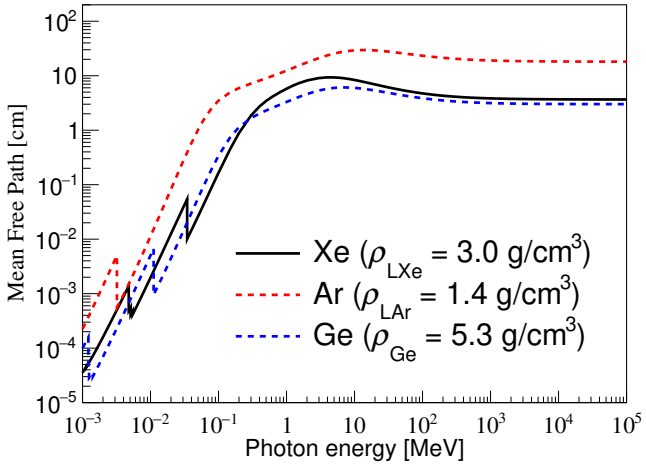

Figure 1.16: Mean free paths of photons in liquid xenon (black curve), liquid argon (red dashed line), and germanium (blue dashed line).

Overall, Properties 1−4 make xenon an effective medium to produce significant signals from WIMP detection. On the other hand, properties 5 and 6 provide a low intrinsic and instrumental background.

1.5 Dual-phase time projection chamber

Time projection chamber (TPC) is a type of particle detector that uses an electric field together with a sensitive volume of gas or liquid to perform a three-dimensional reconstruction of a particle trajectory or interaction position. The origin idea of TPC was proposed by David R. Nygren in 1974 [79]. As mentioned above, the incident particle will deposit its energy into three signal channels, thermal, ionization, and scintillation. Fig 1.17 from [80] is a general schematic diagram for the thermal, ionization, and scintillation processes occurring after energy deposition by any recoiling species in a noble element.

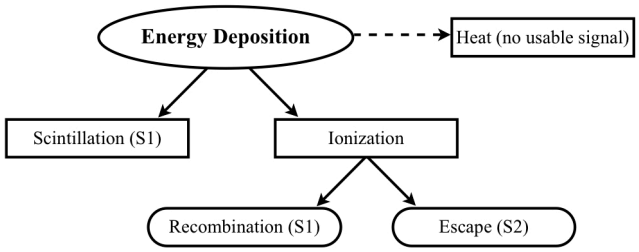

Figure 1.17: General schematic diagram for the ionization, scintillation, and loss processes occurring after energy deposition by any recoiling species in a noble element [80].

One part of the primary scintillation, $S1$ signal, is directly from electronic excitation. Ionization creates electron-ion pairs and electrons either recombine or escape driven by the drift electric field. The recombination generates excimers which yield scintillation lights and contribute to $S1$ as well. Escaped electrons can be collected on the anode wires with charge sensitive amplifiers like in Multi-Wire Proportional Chambers (MWPC). However, small signals are expected from WIMPs

and cause a low signal to noise ratio of charge sensitive amplifier. In a dual-phase detector, electroluminescence was used to amplify the electron signals by producing more scintillation in a high electric field gas phase, $S2$ signal. For the detailed ionization and scintillation process, I refer to the review article [67].

DM particle is expected to deposit its energy in a single site producing an $S1$ and an $S2$ signal inside the sensitive volume of a meter scale LXe detector since the weakness of the interaction. On the other hand, 1 MeV neutrons and 1 MeV γs have a mean free path in order of about 10 cm in liquid xenon. A multi-scattering event from neutrons or γs may produce a single $S1$ signal followed by multiple $S2$ signals. These backgrounds can be reduced significantly by selecting single scattering events with a single $S2$ signal.

Fig 1.18 from [81] shows the schematic view of the dual-phase TPC. The

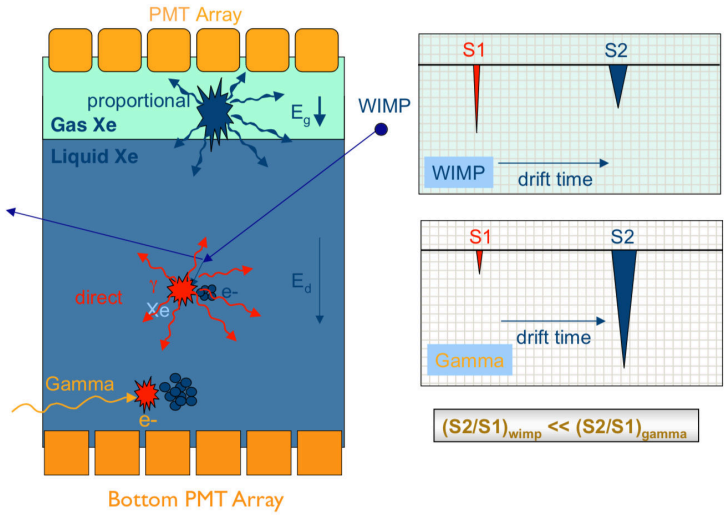

Figure 1.18: Schematic view of a xenon dual-phase TPC [81].

$S1$ and $S2$ signal from one event will be separated by a drift time which provides

information on the event's Z position in the detector knowing the drift velocity under the drift electric field E_d. In order to produce the $S2$ in the gas phase, a Frisch grid (also known as a gate electrode) was placed below the liquid-gas interface, and an anode was placed in the gaseous xenon. High voltage was applied on both electrodes to ensure an extraction field, E_g, within the proper strength above the threshold of electroluminescence and below the avalanche process. Thus, the $S2$ signal, originating from the cloud of ionization electrons, is very localized in the horizontal plane. The event X &Y position can be well reconstructed using the pattern of the array of photon sensors in the gas phase with high precision. The three-dimensional position sensitivity of the detector allows the fiducialization which suppresses the instrumental background with the excellent self-shielding property of xenon.

Moreover, by measuring both $S1$ and $S2$ signals simultaneously, one can infer the ratio of the initial scintillation and ionization which is a smoking gun of the recoil type [82]. As shown on the right of Fig 1.18, the WIMP and neutron produce NR events with smaller $S2/S1$ then the ER ones from γ or β^-. The ratio of the initial scintillation and ionization is much higher for the NR events. In addition to that, the recombination rate is higher for NR since denser electron-ion pairs along the track of energy deposition. The rejection power of ER events is about 99.5%, i.e., a leakage rate $0.53 \pm 0.22_{\text{stat.+sys.}}\%$ of ER events with a small $S2/S1$ ratio below the medium of the distribution of the NR band in $\log_{10}(S2/S1)$ vs. $S1$ in PandaX-II. More detail will be discussed in Sec 4.7.1 with the calibration of detector response to ER and NR.

Chapter 2: CJPL and PandaX experiment

WIMP direct search experiments are running in the underground laboratories to avoid the cosmic ray background. China Jinping Underground Laboratory (CJPL) is the deepest underground laboratory in the world with its overburden of more than 2400 m marble, and it has the lowest muon background at $2.0 \pm 0.4 \times 10^{-10}$ cm^{-2}s^{-1} which is equivalent to the shielding effect of about 6800 meters of water [83].

The PandaX project is a series of xenon-based ultra-low background experiments in CJPL. PandaX collaboration consists of about 50 scientists and engineers. The first and second stage experiments (PandaX-I and II) both utilize dual-phase xenon TPC to carry out a direct search for the dark matter particles. To further suppress the ambient background in the underground laboratory, a passive shielding system was built in PandaX-I to reduce the ambient neutron and γ background from surroundings in the laboratory. Boil-off gaseous nitrogen flowed through a purging tube to suppress the radon concentration in the gaps of the passive shielding system from about 100 to below 10 Bq/m^3. Throughout the periods of data taking, the PandaX-II detector was kept at about -96 °C steadily by a cooling bus, i.e., a custom-made modularized cryogenic system inherited from PandaX-I. Two

circulation loops were constructed to drive the xenon through purifiers. Zirconium getters were used to remove the electronegative impurities in xenon which attenuate the charge signal during the drifting of electrons. In PandaX-II, we circulated the xenon at a flow rate of 50 SLPM, and the study of the mono-energetic events indicated an electron attenuation length of more than 1.5 m was achieved.

In this chapter, a brief survey of underground laboratories and a short introduction to CJPL will be given in the beginning. I will then describe the design of the passive shielding, the performances of cryogenic and purification systems, respectively. In the end, I will summarize runs with different background levels and exposures in PandaX-II.

2.1 CJPL

Direct DM search experiments are conducted in the underground laboratories to suppress the ambient neutron background produced by cosmic ray muons. Tab 2.1 summarizes the characteristics of some deep underground laboratories around the world [84]. The reduced muons flux is the most fundamental characteristic of deep underground laboratories. The overall low background environment (from muons and other ionizing particles) allows searching for rare events. Fig 2.1 [84] shows the depths in meters of water equivalent and their remaining cosmic ray muon intensities.

CJPL is located at Sichuan Province of China as shown in Fig 2.2 [85], under Jinping mountain with a rock shielding of about 2400 m (Fig 2.3 [86]) equivalent to

Table 2.1: Summary of characteristics of some deep underground laboratories. For Access of the laboratories, H = horizontal, V = vertical, and D = drive-in.

Name	Country	since	Space (m^3)	Depth (m)	Access
SNOLab	Canada	2003	30,000	2070	V
LNGS	Italy	1987	180,000	1400	H
LSC	Spain	2010	10,000	850	H
BUL	UK	1989	7,200	1100	V
LSM	France	1982	3,500	1700	H
CallioLab	Finland	1995	1,000	1440	V+D
Baksan	Russia	1967	23,000	1700	H
SURF	USA	2007	7,160	1500	V
Kamioka	Japan	1983	150,000	1000	H
Y2L	Korea	2003	5,000	700	D
CJPL-1	China	2009	9,000	2400	H
CJPL-2	China	2014	300,000	2400	H

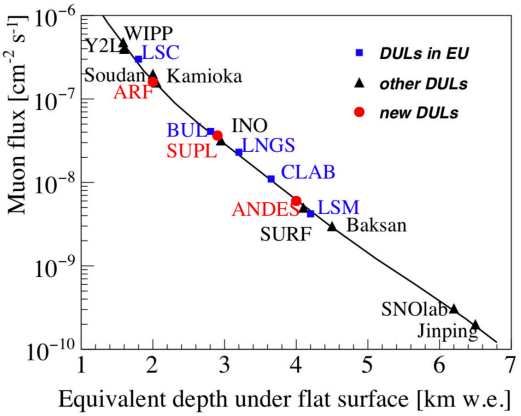

Figure 2.1: Cosmic ray muons flux in different underground laboratories [84].

6,800 m of water. It is the deepest underground laboratory in the world with the lowest muon flux at $2.0 \pm 0.4 \times 10^{-10}$ cm^{-2}s^{-1} [83]. CJPL is a 3-hour drive away from Xichang and the airport (70 km mountain road and 30 km freeway) where logistics and limited mechanical support can be found.

Daily lodging and meals are available outside the east end of the Jinping

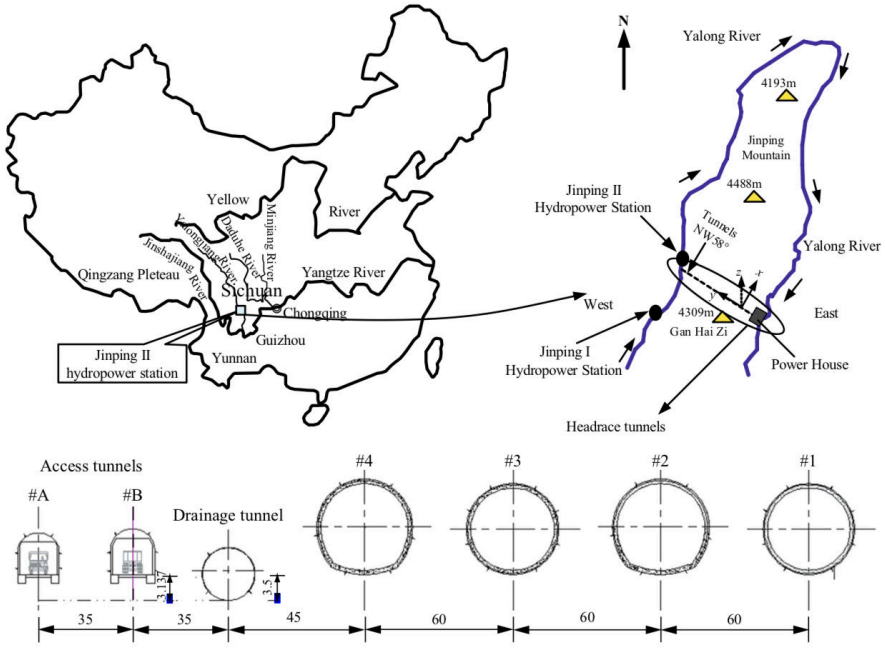

Figure 2.2: Location and layout of 7 tunnels in the Jinping mountain [85].

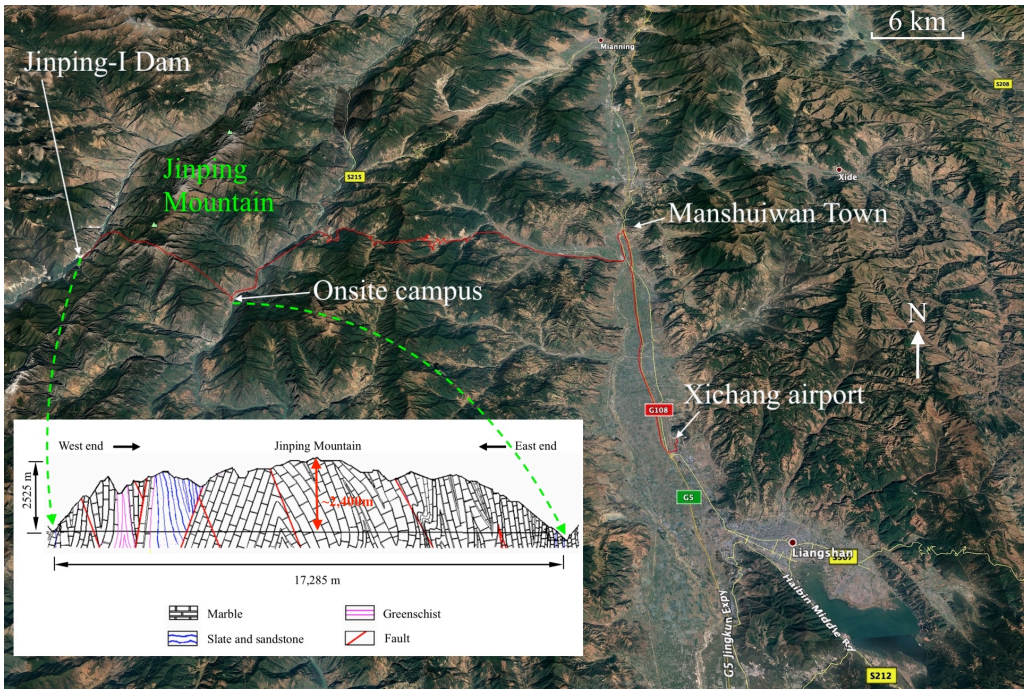

Figure 2.3: The route from Xichang airport to the onsite campus and the Jinping dam through the Jinping mountain (solid red curve). Geological profile along head-race tunnels in Jinping mountain is embedded.

tunnel, i.e., ∼9 km away from the lab. The surface camp is shown in Fig 2.4(a). Two 5 m^3 liquid nitrogen storage tanks were erected beside the parking lot in 2011 and 2013 for CDEX and PandaX, respectively. CJPL-I is a branch tunnel in the

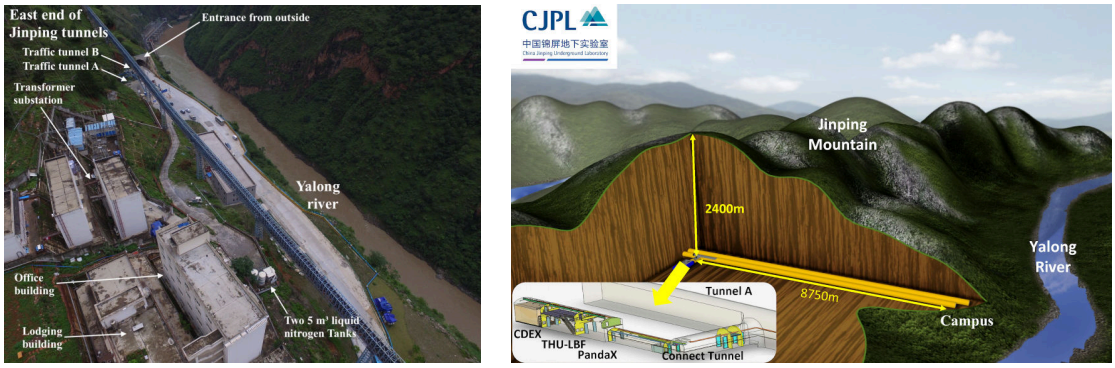

(a) CJPL-I (b) Campus

Figure 2.4: The campus for the PandaX onsite personnel (a) and the schematic diagram of CJPL-I inside Jinping tunnel (b).

middle of Jinping tunnels attached to access tunnel A (or traffic tunnel A) which has 2000 m^3 space in Hall A and ∼ 4000 m^3 space in total including the auxiliary space. Currently, two dark matter experiments, CDEX [87] and PandaX [88] and a neutrino experiment [89] are ongoing at CJPL-I (Fig 2.4(b)).

As shown in the schematic drawing embedded in Fig 2.4(b), the Hall A of CJPL-I is 6.5 m (H)×6.5 m (W)×40 m (L). PandaX experiment uses the outer space of Hall A. There is a requirement for a minimum width of 3 m open space for fire exit and extensive apparatus access. Therefore, PandaX occupies an area with a footprint of 3.5 m×12 m in Hall A as shown in Fig 2.5(a), as well as some space of the auxiliary space outside Hall A.

The second phase upgrade of CJPL, CJPL-II [90] providing an experimental

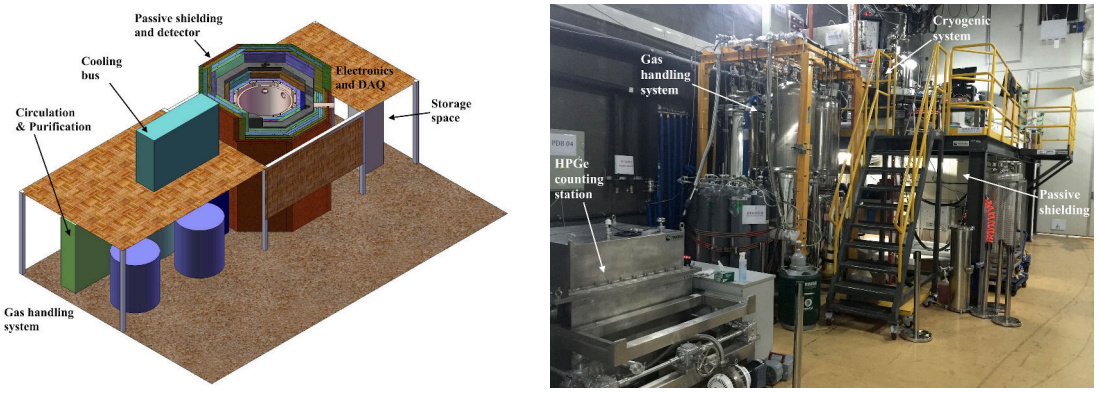

(a) The design layout

(b) A photo of PandaX onsite equipments

Figure 2.5: The design layout (a) and a photo (b) of PandaX facilities in CJPL-I.

space of 100,000 m^3 along with another 200,000 m^3 service and logistics area, is currently under construction. It will have 8 experiment halls, each 12 m in width and 60 m in length, shielded by 2.4 km of rock like CJPL-I. The schematic diagram of the CJPL-II is shown in Fig 2.6 [91]. The succeeding stage of the PandaX project will locate at Hall B2.

2.2 Passive shielding system

Though the overburden 2400 m marble effectively shields the background from cosmic ray, the background from surrounding marble, cement, infrastructure and air inside the laboratory needs to be further reduced.

Ambient neutron flux and γ background

The marble rocks around Hall A in CJPL-I are low radioactive with activities of ^{238}U, ^{232}Th and ^{40}K to be 3.69 $\sim$ 4.21, 0.52 $\sim$ 0.64 and 4.28 Bq/kg respectively [92]. The cement used contains about 60, 25, and 130 Bq/kg of ^{238}U, ^{232}Th and ^{40}K

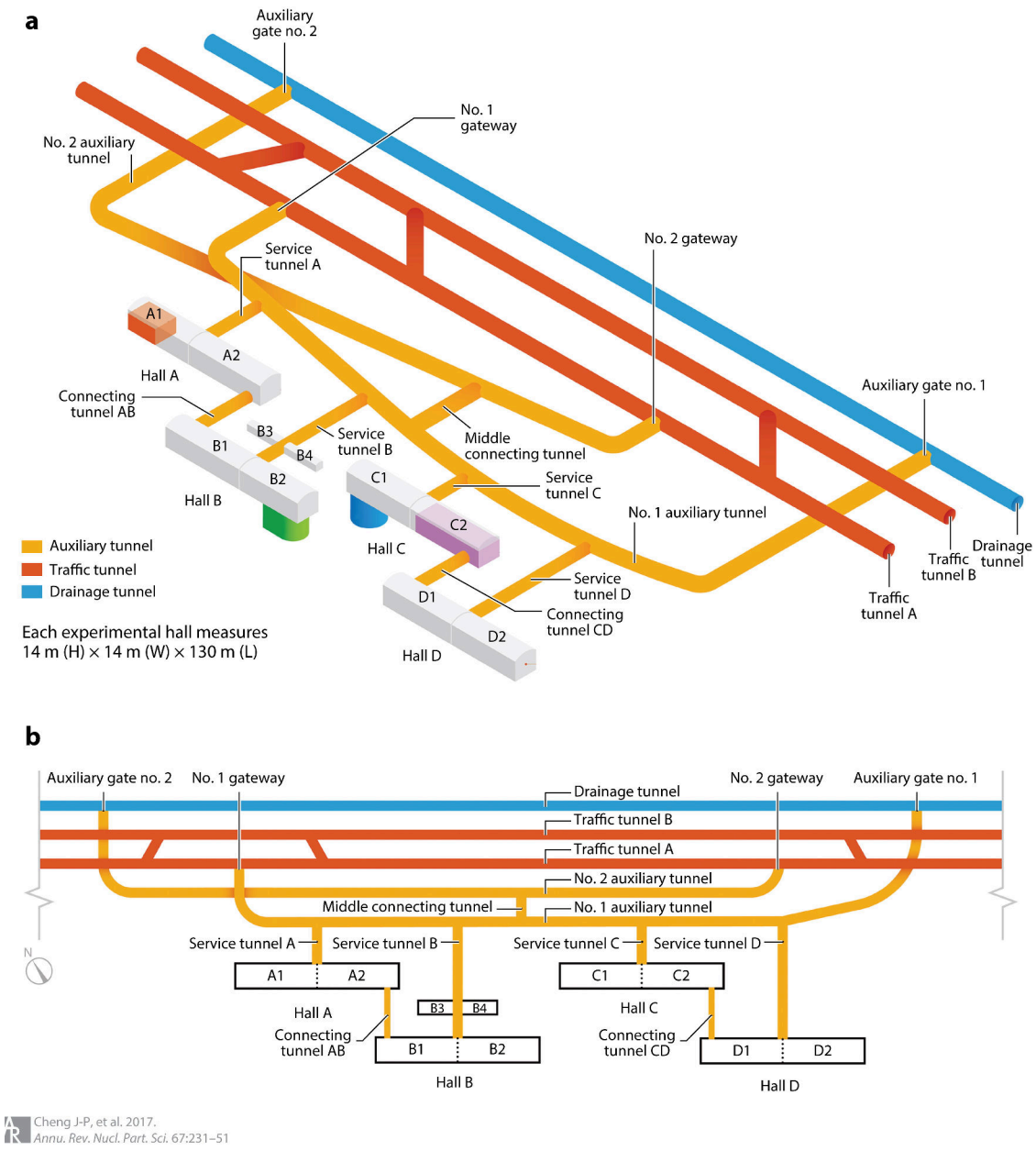

Figure 2.6: Schematic layout of CJPL-II, showing the four experimental halls as well as the connecting and service tunnels [91]. The green pit in Hall B2 will host the next generation of PandaX experiments.

respectively. The ambient radioactivity will produce neutron and γ backgrounds.

Neutron is a critical background in the PandaX experiment designed for searching nuclear recoil signals from WIMPs. The neutron flux was measured at CJPL-I

Hall A to be $4.00 \pm 0.08 \times 10^{-6}$ cm^{-2}s^{-1} for thermal neutron [93] and $3.63 \pm 2.77 \times 10^{-6}$ cm^{-2}s^{-1} for fast neutron in 1-20 MeV [94] and $1.51 \pm 0.03_{\text{stat.}} \pm 0.10_{\text{sys.}} \times 10^{-7}$ cm^{-2}s^{-1} in $1 - 10$ MeV [95].

The γ background is reported in [92]. The γ peak counting rates of primordial radionuclides are: 0.845 and 0.698 count per second (cps) respectively for 352 and 609 keV from ^{238}U progenies ^{214}Pb and ^{214}Bi, 0.105 and 0.092 cps respectively for 911 and 2615 keV from ^{232}Th progenies ^{228}Ac and ^{208}Tl, and 0.165 cps for 1461 keV from ^{40}K.

Passive shielding structure

A passive shielding system was built to block ambient neutrons and γs. The lead (Pb) is a common-used shielding material for photons like X-rays and γs. Copper is similar to lead but more radio-pure. Polyethylene is an excellent moderator for neutrons. As shown in Fig 2.7(a) layer by layer from outside-in, the passive shielding structure consists of 40 cm thick Polyethylene, 20 cm thick Pb, 20 cm thick Polyethylene, 5 cm thick Cu slabs and another 5 cm thick Cu. Polyethylene layers are made of 10 cm thick slabs with herringbone brickwork. Pb layer is made of Pb bricks with herringbone brickwork as well.

The most inner 5 cm Cu is made as a vessel with an inner diameter of 1240 mm and an inner height of 1750 mm which also serves as the outer vessel for vacuum jacket of the cryostat. It has four ports on the top allowing the connection between the detector and peripheral systems. Three horizontal ports are for motion feedthroughs and optical fibers, cables of PMTs and sensors, and HV feedthrough and the calibration tubes, respectively. Another port is tilted by 5 degrees allowing

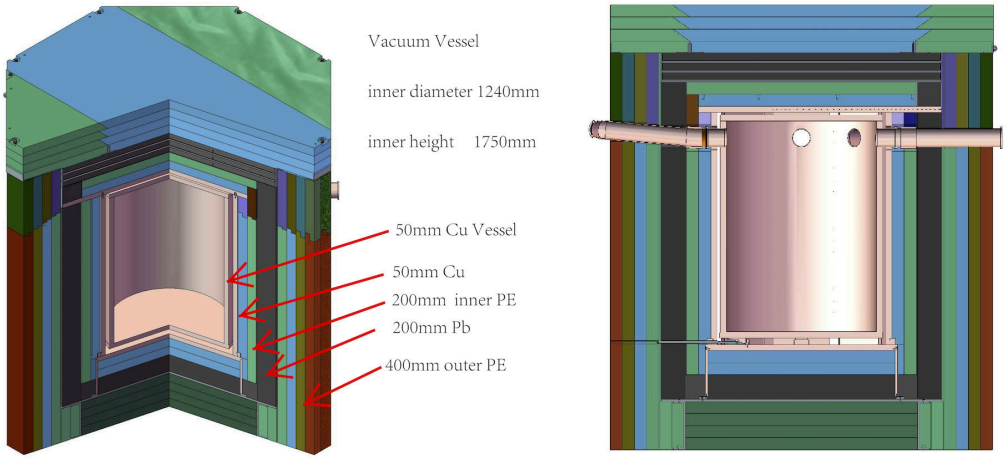

(a) The passive shielding (b) Ports in the passive shielding

Figure 2.7: The passive shielding system of PandaX-I and PandaX-II experiments.

the flow of liquified xenon driven by the gravitational force from the cryogenic system to the detector as shown in Fig 2.7(b). The leveling system is separated into two parts. One is to adjust the levelness, and the other is to adjust the height of the interface between liquid and gaseous xenon.

The whole passive shielding structure has 3.16 m in diameter and 3.68 m in height as shown in Fig 2.8. The total weight is 95 t with 5 t of Cu vessel, 7 t of Cu slabs, 20 t of Poly-Ethylene slabs, 60 t of lead bricks and 4 t of the steel support frame.

Rn level in the shielding structure

Another background is from radon in the air and its progenies attached to the surfaces closed to the detector. Those radioactive isotopes may produce an electron recoil background by releasing γs and a nuclear recoil background by emitting αs to material following by (α, n) reaction. PandaX collaborator monitored the ambient

(a) The passive shielding with platform (b) The construction of passive shielding

Figure 2.8: Photos of the passive shielding in construction.

Rn level intermittently. With functional fresh air ventilating, the ambient Rn level is about 100 Bq/m^3. The ambient Rn level at CJPL-I and CJPL-II were measured using a commercial radon detector (RAD7 from Durridge) in early January 2017. At CJPL-I, the Rn levels at seven positions was measured as indicated in Fig 2.9. Tab 2.2 shows the result of the measurements. One can notice a slight increase in

Table 2.2: The measured Rn levels at seven positions in CJPL-I.

Position	descriotion	Rn level (Bq/m^3)
1	passive shielding	99.57 ± 9.72
2	Kr Station	89.59 ± 9.29
3	Counting station	93.74 ± 9.50
4	Tools	100.02 ± 9.71
5	Storage	89.13 ± 9.24
6	Sink	100.94 ± 9.75
7	Entrance	125.45 ± 10.62

the Rn level from inside out following the flow of fresh air.

The Rn level can increase to about 200 Bq/m^3 in the absence of the fresh air which is consistent with the measurement at CJPL-II without any ventilation

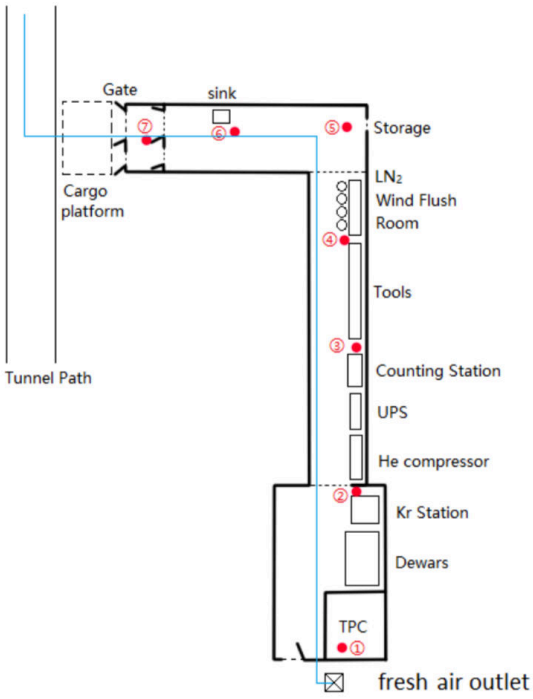

Figure 2.9: Schematic diagram of the positions of Rn measurements at CJPL-I (provided by Linhui Gu). The blue line indicates the flow of the fresh air.

system (211.47 Bq/m^3 on January 2017). The passive shielding system has not been sealed, and Rn can diffuse into the gaps between slabs and bricks and emit γs closer to the detector. Though the gaps are tiny, we purge the passive shielding structure inside-out regularly using boil-off GN_2. A conduit was installed between the Cu vessel and Cu slabs with vent holes as shown in Fig 2.10 [96]. Another gas pipe was placed in that region connecting to RAD7 for Rn level monitoring. Fig 2.11 shows the Rn level in the passive shielding during June 2016 as an example. The average Rn level in that month was 36.1 Bq/m^3. As expected, the Rn level dependents on the flow rate of the boil-off GN_2. The high Rn peaks correspond to the periods without fresh air or sufficient nitrogen supply in the laboratory.

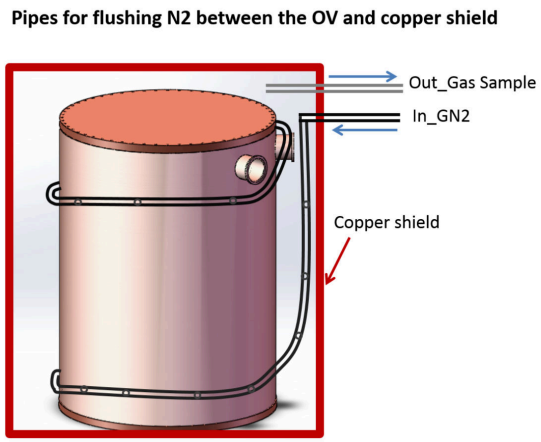

Figure 2.10: The schematic diagram of the purge and monitoring of the Rn level in the passive shielding.

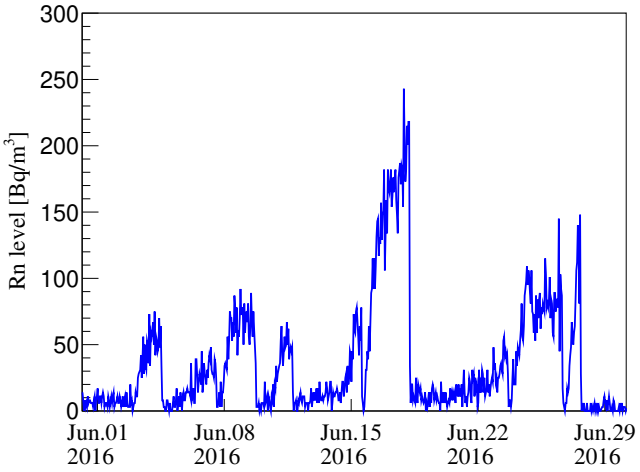

Figure 2.11: The evolution of Rn level in the passive shielding monitored by RAD7.

2.3 Cryogenic system

The cryogenic system of PandaX was described in [97, 98]. The cooling bus is a modularized structure as shown in the upper part of Fig 2.12. It has five modules including pumping, heat exchanger, Pulse Tube Refrigerator (PTR), emergency

cooling and sensor module from left to right.

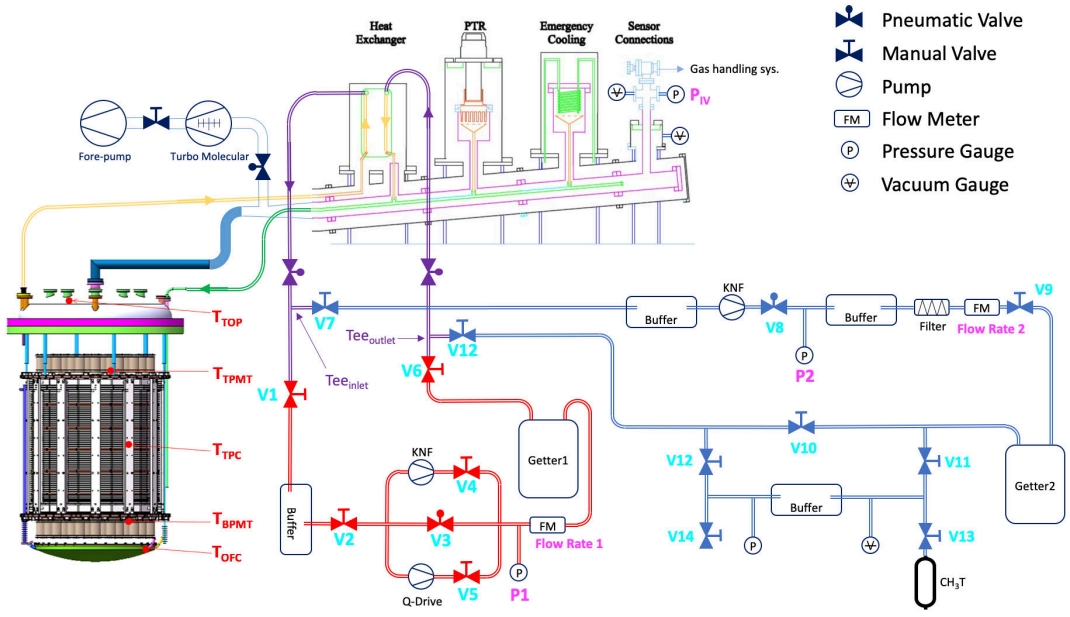

Figure 2.12: The schematic diagram of the cryogenic, purification systems, and the detector in PandaX-II.

Five modules have been designed as double-wall cryostat like the detector, and the cooling bus is connected to the detector through the tilted port embedded in the shielding structure. There is an inner pipe (tilted green pipe in the cooling bus in Fig 2.12), and funnels collect the liquified xenon droplet and guide the flow toward the TPC. A control panel and a crate for readout devices were installed beside the cooling bus (Fig 2.13).

The pumping module is equipped with two sets of turbo and fore pumps for inner and outer volume respectively (TV301, TriScroll600, and IDP-15 from Agilent and F200/1200 from KYKY, Beijing). The barrel of the inner vessel, outer vessel (Cu vessel) and part of the pumping module are not shown in Fig 2.12. The heat exchange module is the interface with circulation and purification loops which

(a) (b)

Figure 2.13: The control panel and readout devices of the cooling system (a) and a photo of the cooling bus (b).

has 95% efficiency and saves a considerable amount of cooling effort for thermochemical purification via hot zirconium getter. The PTR module (PC150 from Iwatani Industrial Gases Corp.) provides the regular cooling power up to about 180 W at −94.4 °C. To minimize the heat loss, all inner vessel of the detector and cooling bus were wrapped with thermal insulation layer as in Fig 2.14 which lead a net heat loss of about 80 W at a typical outer vacuum at 2×10^{-3}Pa. The circulation introduces a heat load at about 1.125 W/SLPM.

The emergency cooling module is equipped with a coil and connects to a LN_2 tank through a solenoid valve controlled by the internal pressure gauge. In case of insufficient cooling power from PTR, the LN_2 will flow through the coil and freeze the xenon gas for safety. The pressure gauge (digital and mechanical) and vacuum gauges are mounted to the sensor module at the end of the cooling bus. There is a rupture disk rated for 2.5 bar differential pressure mounted on the sensor module for

(a) (b)

Figure 2.14: The PandaX-II detector wrapped with thermal insulation layers.

safety. The sensor module also connects the cooling system with the gas handling system.

Fig 2.15 shows the stability of the internal pressure and two temperature readouts in the PandaX-II detector during Run9 (from Mar. 9 to Jul. 2) and Run10 (from Apr. 22 to Jul. 17 in 2017). There are five temperature sensors (Pt100) mounted in the detector in PandaX-II. Two shown in Fig 2.15 are one in the top of the inner vessel on the feedthrough and one in the middle of the TPC on the PTFE supporting bar. During Run9, the mean internal pressure was 0.82 ± 0.02 barG. The top and TPC temperatures were -90.25 ± 0.99 and -96.4 ± 0.32 °C. In Run10, the internal pressure was 0.861 ± 0.003 barG. The top and TPC temperatures were -90.28 ± 0.05 and -96.38 ± 0.04 °C. In general, the running condition is more stable in Run10 than in Run9.

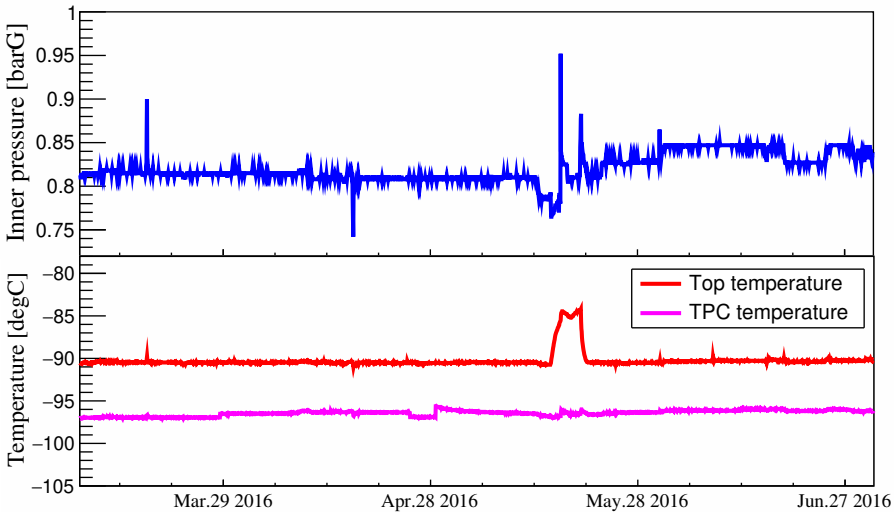

(a) Run9

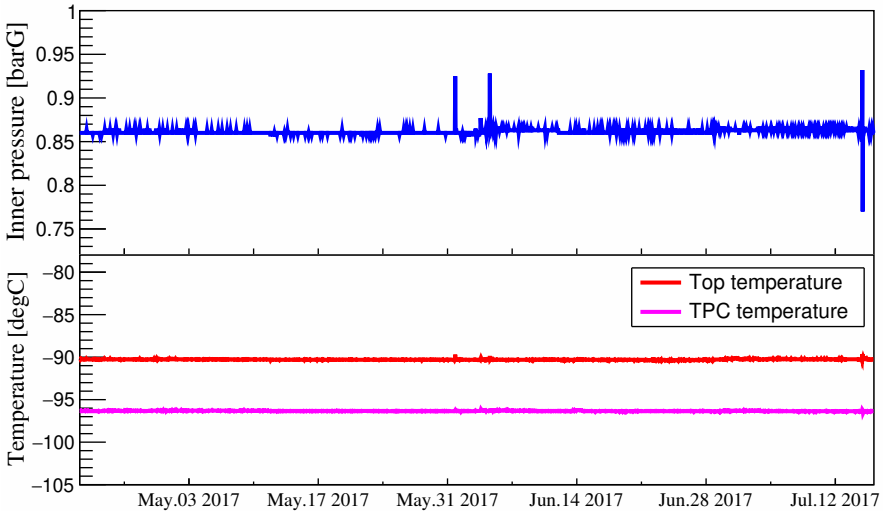

(b) Run10

Figure 2.15: The stability of the PandaX-II detector in Run9 and Run10.

2.4 Purification system

The schematic diagram of the purification system is shown in Fig 2.12 as well. There are two loops of circulation in the PandaX-II experiment. The red one (loop1)

is inherited from the PandaX-I experiment with two pumps (a KNF and a Q-Drive) connected in parallel as the backup to each other. The blue one (loop2) was added on May 2015 for better circulation and internal calibration source injection (more details in Sec 3.3). Both loops are equipped with a hot zirconium getter (Mod. PS5-MGT50-R-909 from SAES). The maximum flow rate is about 65 SLPM for loop1 but only 30 SLPM for loop2 due to longer plumbing and smaller flow conductance. Running both loops in parallel will provide about 70 SLPM in total (loop1 reduces to 50 SLPM). Therefore, we usually circulate xenon using loop1 only and use loop2 as a backup and for injections of internal calibration sources.

Fig 2.16 shows the electron attenuation length (solid red circles) and flow rate (blue dots) of the PandaX-II detector during DM data taking in Run9 and Run10. The leakage accident on loop1 around May 18, 2016, caused a significant decrease in

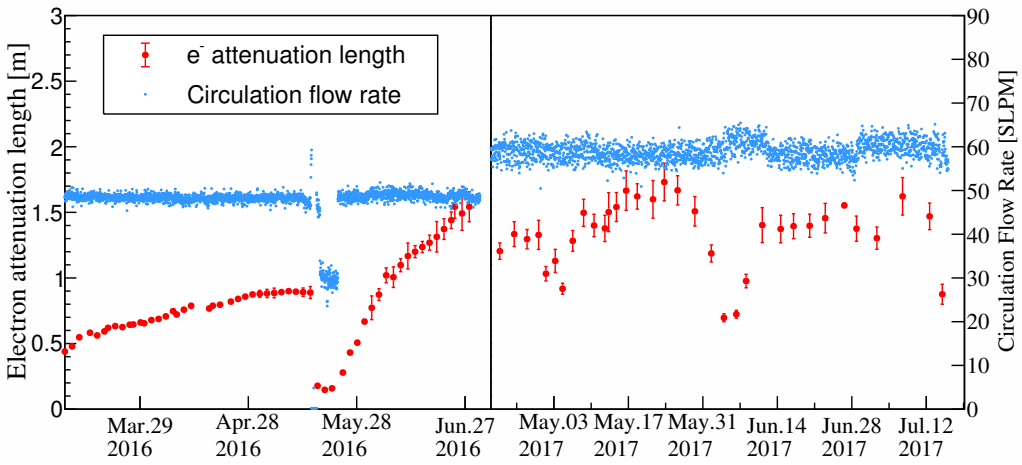

Figure 2.16: The electron attenuation length (red solid circle) and flow rate (blue dot) of the PandaX-II detector during DM data taking in Run9 and Run10.

the electron attenuation length. We show the electron attenuation length instead of

the electron lifetime due to the change of the drift field from Run9 to Run10. Data with an electron lifetime greater than 200 μs, i.e., 0.34(0.33) m in Run9(10) (TPC length is 0.6 m), are used in the physics analysis.

2.5 Run history in PandaX-II

The PandaX project has gone through the first two stages, i.e., PandaX-I and PandaX-II experiments. The PandaX-II experiments inherited most peripheral systems from the PandaX-I experiments with upgrades and improvements. The TPC and the calibration system were completely rebuilt.

The data-taking periods are enumerated as Run1$-$5 in PandaX-I. The PandaX-II experiment started in 2014. Run6 and Run7 are two mechanical commissioning runs in PandaX-II. Run8 is the physics commissioning run demonstrated a well-functioning detector. In Run8, we collected data of 6-ton-day exposure with krypton contamination at a level of 507 ppt in 2015 (See details in Sec 4.6.1).

A data set of 27-ton-day exposure was taken as Run9 in 2016 with 10 times lower Krypton level after a surface distillation campaign in early 2016. In early 2017, we carried out an underground distillation campaign which further reduced the Krypton level to 6.6 ppt. Another data set of 27-ton-day exposure as Run10 was collected with 0.8 mDRU (1 mDRU= 10^{-3} events/day/kg/keVee) which is the lowest background rate at that time among the experiments with similar detection technology.

Chapter 3: PandaX-II TPC and calibration system

PandaX-II reuses most of the infrastructures of PandaX-I. The most significant upgrades are the new inner vessel constructed from stainless steel with much lower radioactivity, reducing the ^{60}Co activity by more than an order of magnitude [99], and a larger xenon time projection chamber (TPC). The cylindrical TPC contains 580 kg LXe in the sensitive volume enclosed by polytetrafluoroethylene (PTFE) reflective panels with an inner diameter of 646 mm and a maximum drift length of 600 mm. The liquid level can be adjusted remotely via an overflow mechanism. A skin (surface layer) LXe volume with a thickness of about 40 mm is confined between the inner PTFE and a layer of outer PTFE panels. Two identical arrays of photomultiplier tubes (PMTs) were placed above and below the TPC, respectively, each consisting of 55 Hamamatsu-R11410 3″ PMTs, to detect scintillation photons in the sensitive volume. Two additional PMT arrays are located at the same heights as the 3″ arrays, each with 24 Hamamatsu-R8520-406 1″ PMTs, to produce veto signals in the skin volume to suppress background events due to ambient gamma rays.

Radioactive sources calibrate the electron and nuclear recoil (ER and NR) responses. Two PTFE tubes were installed on the interior surface of the outer Cu

vessel for the deployment of external sources like AmBe and ^{252}Cf neutron sources, and ^{60}Co, ^{137}Cs and Thorium γ sources. The self-shielding property of liquid xenon obstructs an efficient calibration of low energy ER response from any external γ source. Therefore, an injection system was designed and embedded in one of the circulation loops. It allowed us to uniformly mix gaseous electron emitters into the xenon such as tritiated methane, ^{83m}Kr, and ^{220}Rn.

In this chapter, I will describe the optimization of the design of Cu plates and various PTFE parts using finite element analysis at first. The R&D of feedthroughs on the cryostat connecting TPC with other systems including circulation, leveling, electronics, optical fibers, sensor readout, and high voltage system will be presented afterward. A custom-made HV feedthrough was designed for applying high voltage on the cathode. A drift field at about 400 V/cm was achieved by applying -29.3 kV on the cathode. This drift field is the highest one among the WIMP dual-phase xenon TPC detectors. The design of the calibration tubes for external sources and the injection setup will be described in the end.

3.1 Time projection chamber

TPC is made of the top and bottom Cu plats and the field cage as shown in Fig 3.1(a). PTFE reflective panels enclose the field cage with an inner diameter of 646 mm and a maximum drift length of 600 mm. The drift field is defined by a cathode mesh (200 μm wire diameter with 5 mm pitch) placed at the bottom of the TPC and gate grid (100 μm wire diameter with 5 mm pitch) 5.5 mm below the

liquid level. The extraction field, which extracts electrons in liquid xenon into the

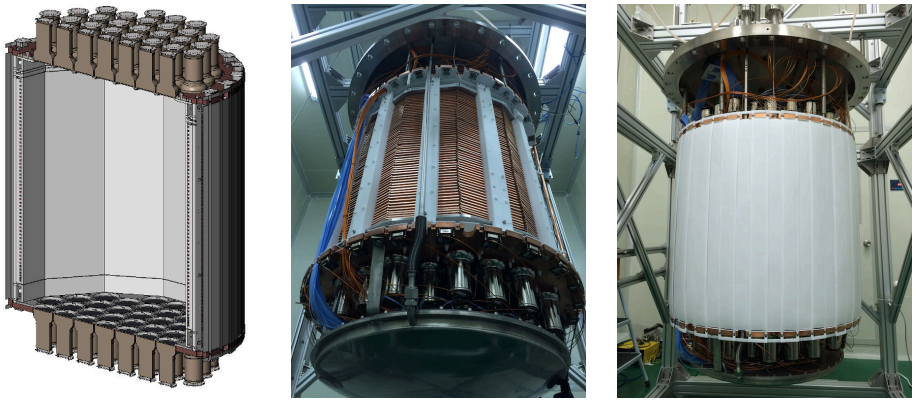

(a) (b) (c)

Figure 3.1: The cross section of the TPC design (a), a photo of the TPC assembly without the outer PTFE reflector (b), and a photo of the final TPC assembly (c).

gas region at the liquid-gas interface, is produced between the gate grid and the anode mesh located 5.5 mm above the liquid level with the same construction as the cathode. Outside the PTFE panels, 58 Cu shaping rings are mounted to guarantee the uniformity of the drift field (Fig 3.1(b)). The top PMT array is placed 46 mm above the anode, and the bottom array is located 66 mm below the cathode. A screen grid (200 μm wire diameter with 5 mm pitch), set at the ground, is placed 6 mm above the bottom PMT array to shield the cathode high voltage. A skin LXe volume with a thickness of about 40 mm is confined between the inner PTFE and a layer of outer PTFE panels (Fig 3.1(c)).

In this section, I will describe the optimization on the design of components of TPC and the change to the field cage after a series of commissioning runs.

3.1.1 Finite element analysis

During the design phase, I optimized the design related to the top and bottom Cu plates including the gap between PMTs, hanging structure of the entire TPC and spring structure for holding PMTs. I used both ANSYS and SOLIDWORKS to carry out the Finite Element Analysis (FEA) on the components as shown in Fig 3.2. The deformation and stress of both top and bottom plates are simulated under certain boundary conditions.

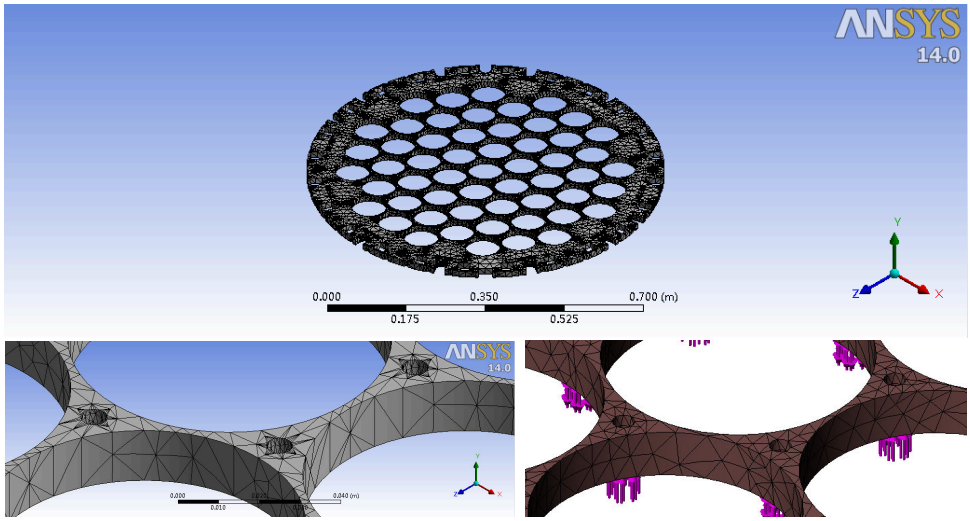

Figure 3.2: Elements generated for bottom Cu plate simulation in ANSYS (top and bottom left) and SOLIDWORKS (bottom right). Elements were refined around M6 screw holes (bottom left). Magenta arrows in the bottom-right figure were the demonstration of the load on the Cu plate.

According to the simulation, we decided to use the design with 2.0 mm as the minimum distance between PMT holes instead of 1.5 mm to avoid deformation and yield of the bottom Cu plate under the buoyancy of bottom PMTs as shown in Fig 3.3.

I used maximum deformation and stress to indicate the stiffness. The factor

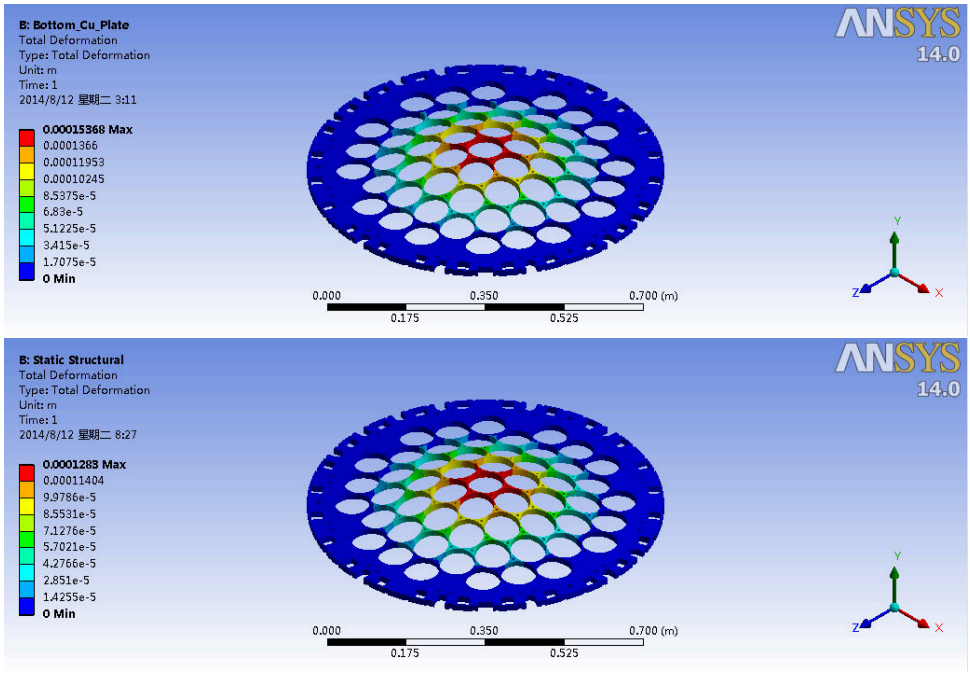

Figure 3.3: The deformation of bottom Cu plates with 1.5 (top) and 2.0 mm (bottom) gaps respectively.

of safety (FoS) is defined as the ratio of the material strength over the load. The results of simulations are listed in Tab. 3.1 where **A** stand for ANSYS and **S** for SOLIDWORKS. In ANSYS, when FoS $>$ 15, the software will show minimum FoS $>$ 10.

Table 3.1: Summary of the results from FEA simulations of the bottom Cu plate.

Quantity	1.5mm **A**	1.5mm **S**	2mm **A**	2mm **S**
Max Deformation (mm)	0.154	0.151	0.128	0.121
Max Stress (MPa)	13.98	32.08	10.86	23.58
Min FoS	>10	8.06	>10	10.97

The number of hanging rods for hoisting the entire TPC on the dome of the inner vessel was altered to be 6 instead of 3 to reduce the deformation of the top Cu plate under the load as shown in Fig 3.4. Maximum deformation, maximum stress

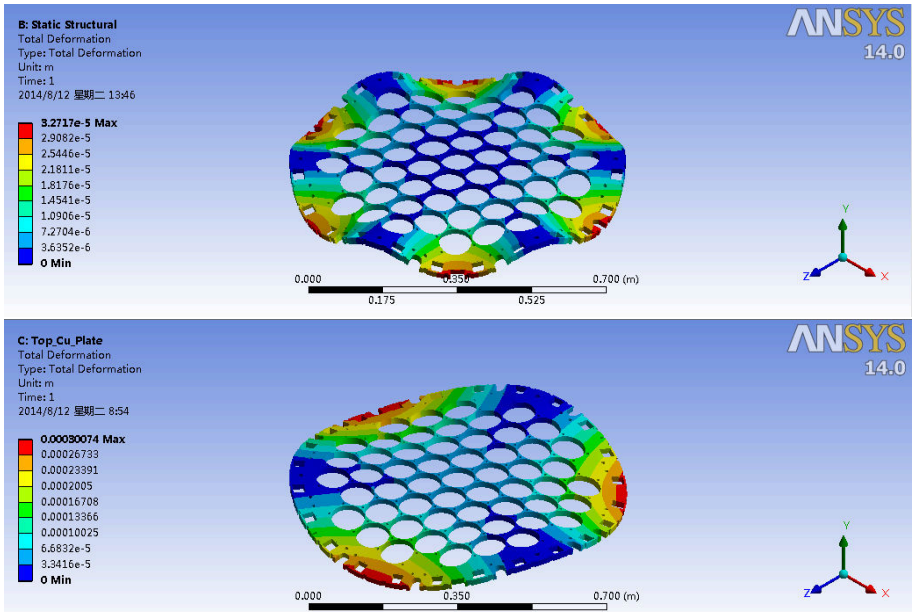

Figure 3.4: The deformations of cases for the top Cu plate hanging on the inner vessel with 6 (top) or 3 (bottom) rods.

and FoS from ANSYS are listed in Tab. 3.2.

Table 3.2: Summary of the results from FEA simulations of the top Cu plate hanging plans.

Quantity	3 hanging rods	6 hanging rods
Max Deformation (μm)	300.74	32.72
Max Stress (MPa)	46.53	9.53
Min FoS	4.56	>10

Both FEA results suggested the original PTFE hanging rods of peripheral PMTs would have small elongation but suffer severe deformation and bending as shown in Fig 3.5.

And we modified the design accordingly to have the shorter rods and longer springs as shown in Fig 3.6.

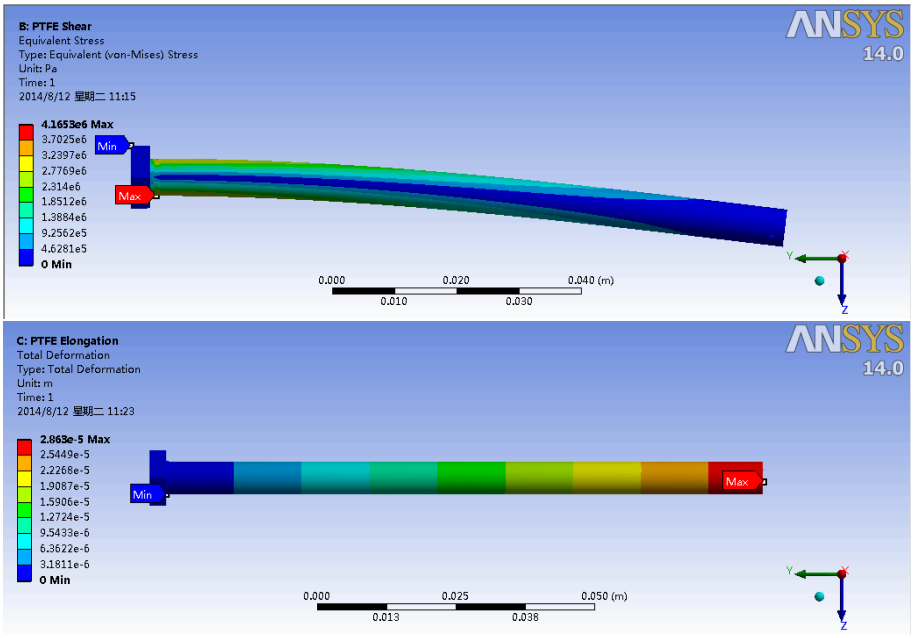

Figure 3.5: The shear stress and elongation of the PTFE hanging rods.

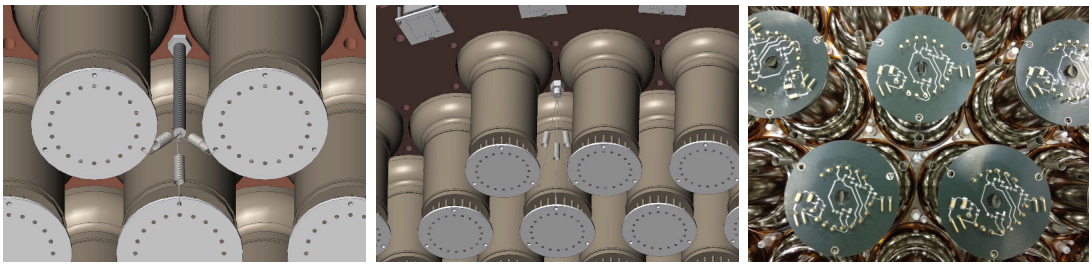

Figure 3.6: The original (left) and modified (middle) design of PTFE hanging rods for PMTs. A photo of the hanging rods along with springs and PMTs is on the right.

3.1.2 Electrodes

After Run7, a series of commissioning runs were carried out. To avoid the suspicious sparking events from the electrodes, we changed from the original design of 3 electrodes on the top to 2 electrodes. The top screening grid was omitted, and the distance between the anode and the gate was changed from 5.5 to 11 mm as shown in Fig 3.7.

(a) (b)

Figure 3.7: The original 3 electrodes (a) and the final 2 electrodes (b) on the top of PandaX-II TPC.

During Run8 and Run9, a voltage of -29.3 and -4.95 kV was applied to the cathode and gate, respectively, and the anode was kept at ground, resulting in a drift field of 393.5 V/cm (with spatial variation of about 0.77% in the fiducial volume) in LXe as in Fig 3.8, and an extraction field of 4.4 kV/cm in the gaseous xenon right above the liquid surface. The uniformity of the extraction field is reflected in the

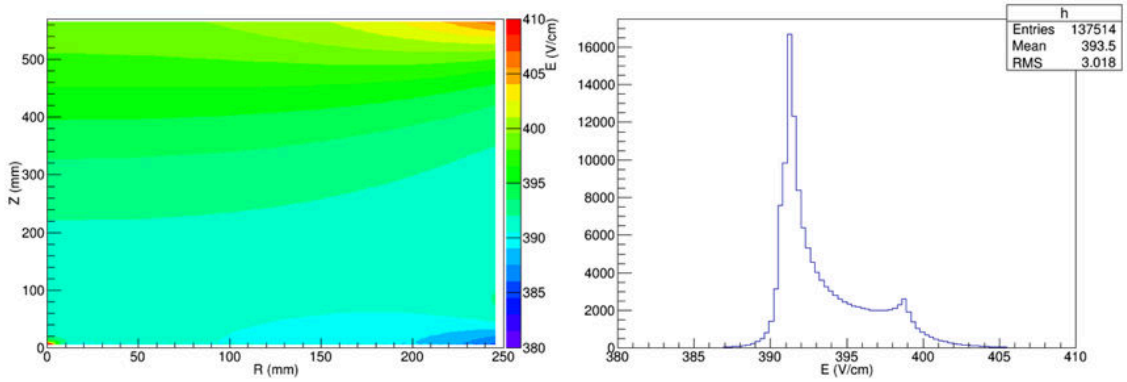

Figure 3.8: The field uniformity distribution based on the COMSOL simulation. The field map in (r, z) and the distribution in the fiducial volume (left). The mean and variance of the field strength in the fiducial volume is 393.5V/cm and 0.77%, respectively.

position dependence of the $S2$s from single electron and partly reflected in the $S2$s of mono-energetic events. More detail will be discussed in Sec 4.4.

In Run10, the voltage on cathode was changed to -24.0 kV to avoid spurious discharge resulting in a drift field of about 320 V/cm. The voltage on the gate remained unchanged, and so did the extraction field.

3.2 Feedthroughs and sensors

There are four ports on the outer vessel as shown in Fig 2.7(b) before and Fig 3.9 below. The left port connects a thick tube for gas pressure balance and two thin pipes for liquid xenon in and out. The top port is used for cathode HV feedthrough and the calibration tubes for external sources. The top left port is for the cables of PMT and sensors. The right port is designed for motion, gate HV feedthrough and optical fibers.

Figure 3.9: A top-view photo of feedthroughs passing through 4 ports on the Cu outer vessels.

All feedthroughs on the Inner Vessel (IV) are on the top dome. In this section, I will describe the design of custom-made feedthroughs as well as sensors and other subsystems connected to them. There are one CF50, fourteen CF35 and one CF16

flange in total on the IV. The CF50 one is in the center connecting the cooling bus with IV for balancing the pressure of gaseous xenon. One CF35 and one CF16 flange for liquid xenon circulation. An array of 10 CF35 flanges are aimed for PMTs, sensors and optical fibers. Two CF35 flanges for the cathode and gate HV feedthrough. The other CF35 flanges for the motion feedthrough.

3.2.1 Motion feedthrough and liquid circulation tubes

The liquid level can be adjusted remotely via an overflow mechanism. The overflow chamber, as shown in Fig 3.10, has a capacity of about 18 L and sealed using indium wire. It is mounted on the bottom Cu plate as shown in Fig 3.1(b) with the overflow-in tube. An internal wall is welded to prevent it from crush under liquid pressure. A level meter is installed in the center to measure the liquid level inside it. Three 5/8″ tubes are connecting the overflow chamber for pressure-equalizing, liquid out and overflow in, respectively. The cable of the level meter goes through the pressure-equalizing tube.

The pump in the circulation system will drive the liquid xenon out of the bottom of the overflow chamber through the heat exchanger. And the purified xenon droplet will be collected by the central tube in the cooling bus and delivered to the inlet port in the bottom of the TPC. Once the liquid level reaches the overflow point, xenon starts to drop into the overflow chamber through the overflow-in tube. The overflow-in tube can be adjusted through a custom-made motion feedthrough on the IV driven by an MDC rotary motion feedthrough (Part No. 670000) on the

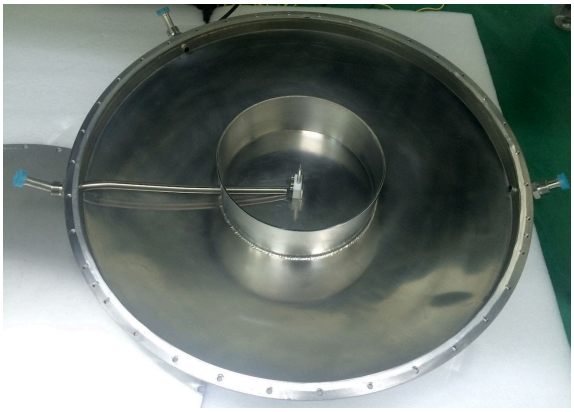

Figure 3.10: The internal structure of the overflow chamber. A level meter in the middle of the chamber. The tube on the left is for liquid xenon out. The other two are for pressure equalizing and overflow-in.

outer port as in Fig 3.11.

The custom-made motion feedthrough and the overflow-in tube is connected by a motion transfer bar. The level, i.e., the overflow point, is initially set in between the gate and anode electrodes as shown in Fig 3.12.

A PTFE Tee guides the purified xenon to the bottom of the TPC. The Tee is fixed on the bottom Cu plate. A horizontal tube delivers the most purified xenon to the area below the cathode and above the bottom screening grid. The design goal is to have high efficiency for the purification in the sensitive volume. However, during the early stage of xenon filling, the thermal stress from the sudden cooling of PMTs by cold liquid xenon can create cracks in the quartz windows of PMTs. The end cap with three holes and a float valve with a nylon ball is designed to allow liquid xenon flow to the bottom of the IV in the early filling period as shown in Fig 3.13.

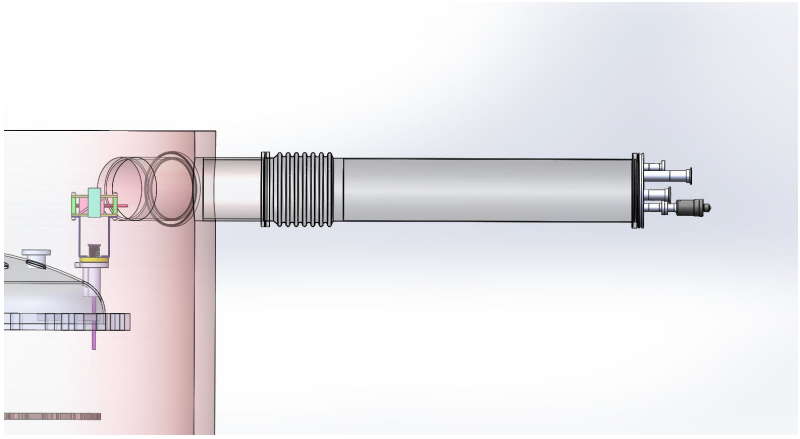

(a)

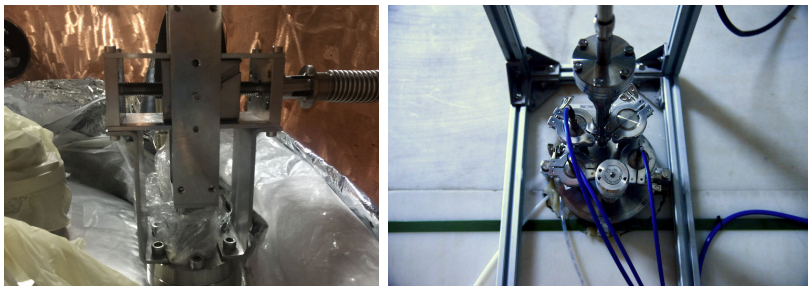

(b)

Figure 3.11: The design of the motion feedthrough (a) and the custom-made motion feedthrough on the IV and the MDC rotary motion feedthrough (b).

3.2.2 Feedthroughs for PMTs, sensors and optical fibers

There are ten CF35 flanges for PMTs, sensors and optical fibers. We split the HV on the 3″ PMTs. Therefore, each 3″ PMT was connected to two cables with four pins and the outer surface of the PMT was at about −650 V during the normal running condition as shown in Fig 3.14(a). The negative HV was grouped into ten sets using ribbon cables as in Fig 3.14(b). A single Kapton cable supplies the HV on 1″ PMTs in the skin region. Eight Kyocera 48-pin feedthroughs (Mod.

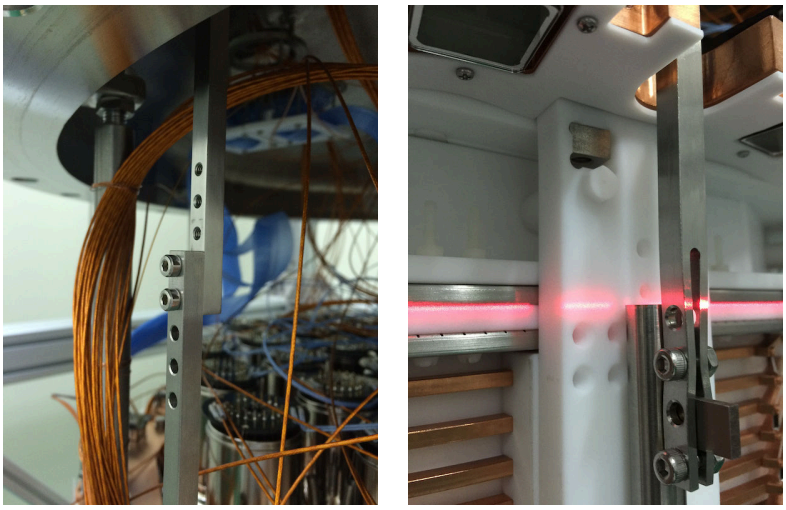

(a) (b)

Figure 3.12: The connection between the custom-made motion feedthrough and the motion transfer bar (a) and the connection between the bar and the overflow-in tube (b).

GMM-B3209) are used for PMTs.

One Kyocera feedthrough is used for five temperature sensors and five level meters. The positions of the five Pt-100 temperature sensors are indicated in Fig 2.12. They are mounted on the detector using thin Cu wire as shown in Fig 3.15.

A 760 mm long level meter is installed for control of the filling process. It covers the range from the bottom to the top Cu plate. A short one is installed in the overflow chamber to indicate the occupancy. Another three short ones with an effective range of 6 mm were installed at the height of the expected level as shown in Fig 3.16. Both the long and overflow chamber ones are equipped with PTFE fillers as the self-calibration parts which maintain constant capacities while liquid level immersing those fillers.

Level meters provided useful information during the filling and commissioning

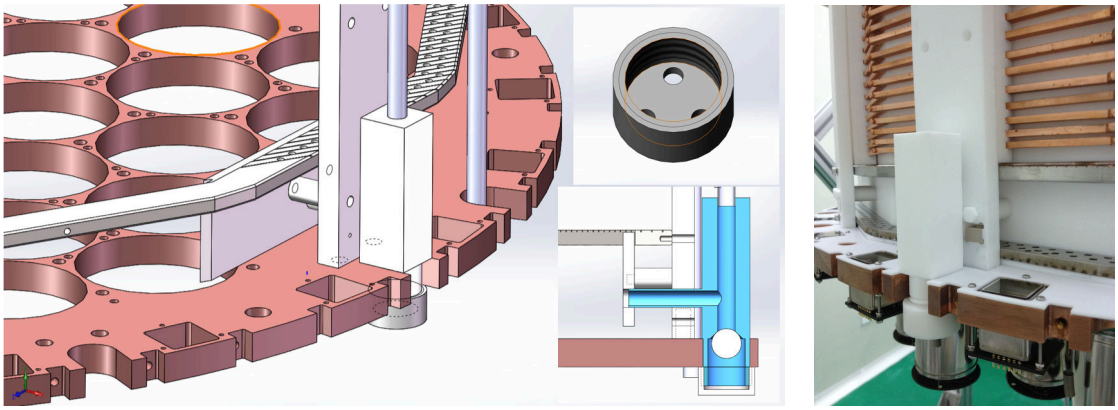

(a) (b)

Figure 3.13: The design of the purified xenon inlet with a cross section view and the detail of the end cap (a), a photo of the PTFE Tee (b).

stage of the PandaX-II. Fig 3.17 shows the capacities of level meters during the filling stage in Run7. The mass of xenon filled in can be read out from the integral of the flow meter. The liquid level can be inferred from temperature sensors and level meters. When the level reached the temperature sensor mounted on the overflow chamber, the temperature readout of that sensor stabilized at liquid temperature, i.e., −96 °C. As shown in Fig 3.17, when the level reached the bottom of the long level meter, its capacity increased due to the difference dielectric constant of liquid and gaseous xenon. When the liquid level reached the bottom of three short ones, it was about 3 mm below the overflow point. The capacities of the long and three short ones increased until the overflow started. The circulation flow rate would decrease due to the increasing flow resistance of liquid instead of gaseous xenon. The capacity of the overflow level meter started to increase. All capacities stayed constant if filling stopped and the detector reached a dynamic equilibrium with

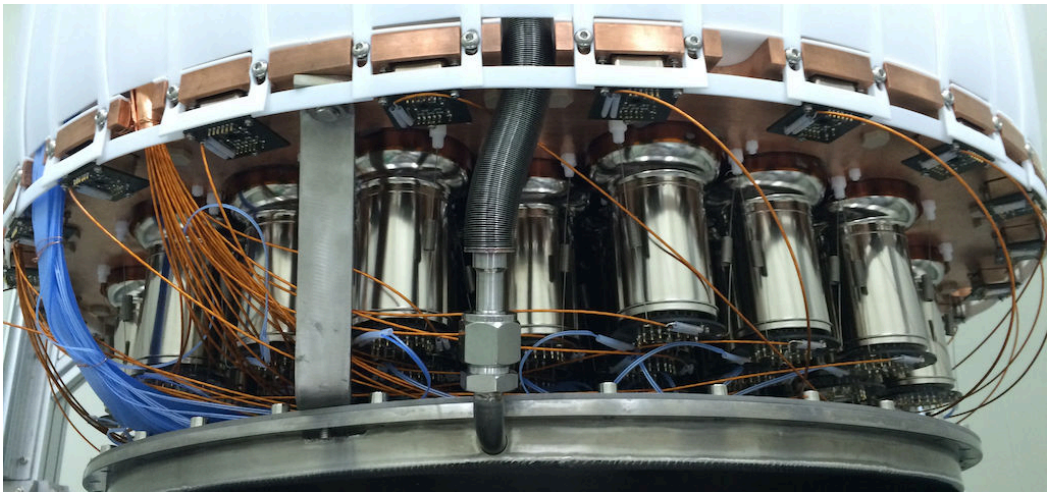

(a)

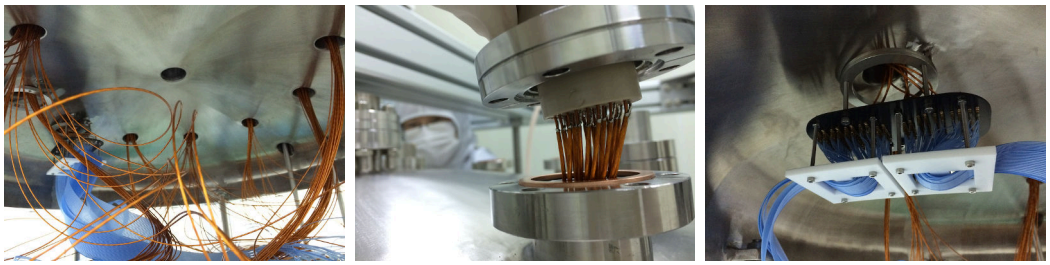

(b)

Figure 3.14: The HV cables of 1″ and 3″ PMTs (a), cable bundles into the feedthroughs, a custom-made PEEK adapter connects a bundle of cables to the Kyocera feedthrough, and ribbon cables grouped into 10 cables on a board (b).

Figure 3.15: Five temperature sensors in PandaX-II detector top down.

regular circulation flow rate. In PandaX-II, we can adjust the level by rotating the motion feedthrough outside the shielding structure at 0.85 mm/round with negligible

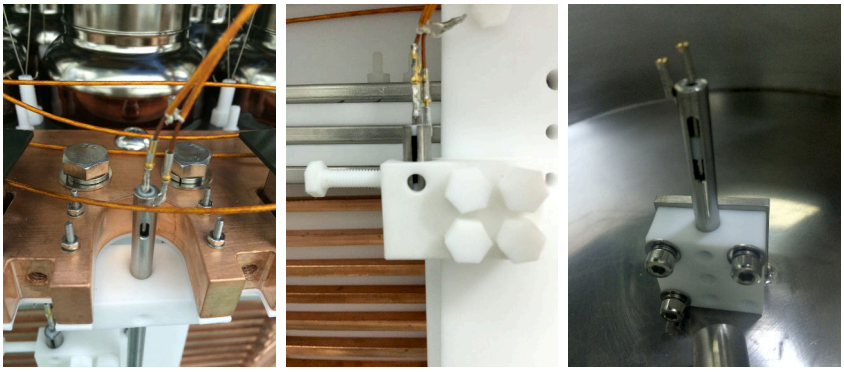

Figure 3.16: The long level meter (left), one of the three short ones (middle), and the overflow chamber one (right) in the PandaX-II detector. A PTFE filler can be seen in the middle of the one in the overflow chamber.

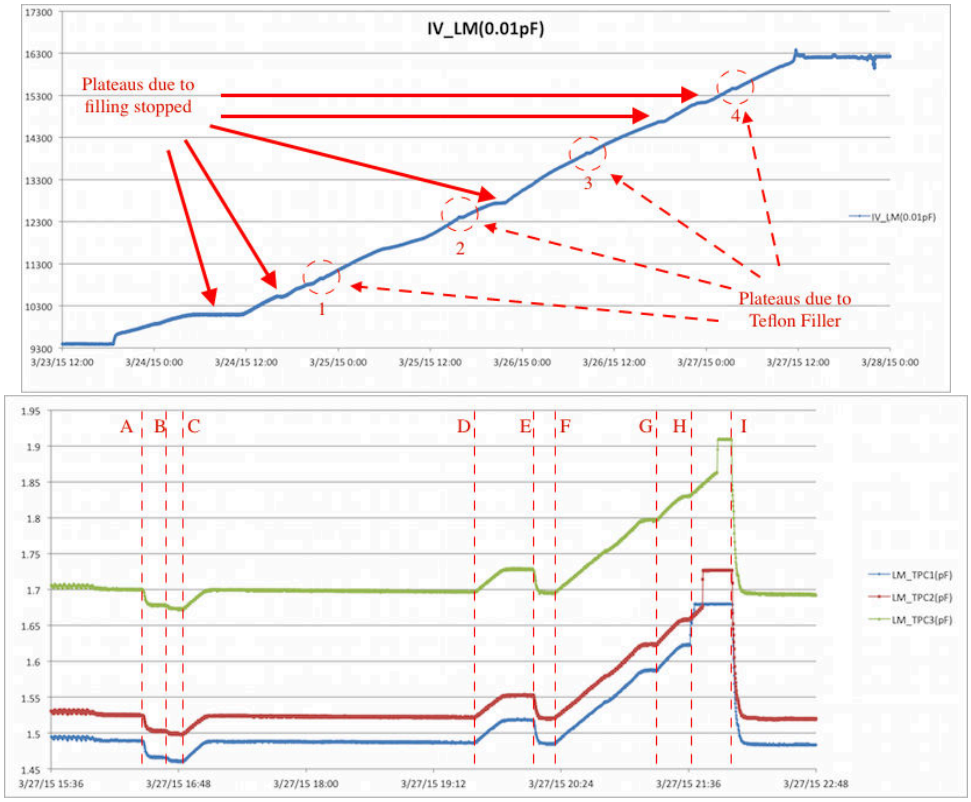

Figure 3.17: The capacity of the long level meter during the filling of Run7 (top). The capacities of three short level meters during the adjustment of the height of the liquid level (bottom).

hysteresis effect.

After Run6, we had surgery to the inner vessel to release the residual thermal

stress in the big flanges. Dry ice and LN_2 are used for cooling, and warming-up cycles and the dry ice may create tiny cracks in the ceramic of some Kyocera feedthroughs. Two Kyocera feedthroughs were found leaking using Pfeiffer sniffer while 2 bar gaseous xenon filled in the inner vessel after warming up to the room temperature. We potted Kyocera feedthroughs with Epoxy as shown in Fig 3.18.

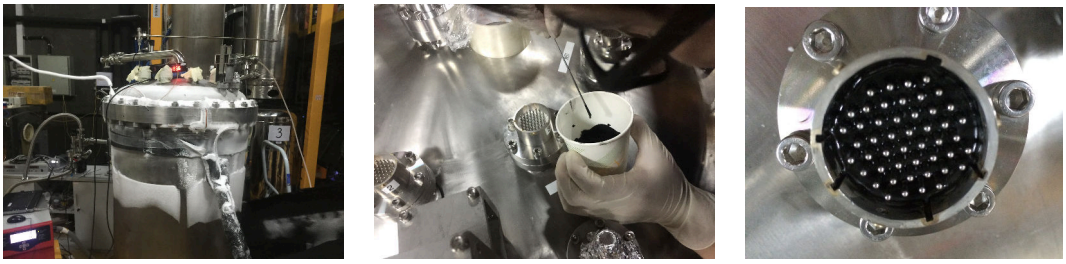

(a) (b) (c)

Figure 3.18: The big flanges of inner vessel cooled to about -83 °C using LN_2 flowing through a Cu coil and dry ices (a), the process of potting Kyocera feedthroughs using Epoxy (b), and a potted Kyocera feedthrough (c).

One Accu-Glass feedthrough (part No. 112606) with four male SMA 905 connectors mounted on a 2.75″ CF flange is used to connect three optical fibers guiding photons from a blue LED for PMT calibration. Three fibers are fixed at PTFE diffusers, and photons diffuse into TPC through the gaps between PTFE parts near the anode and gate grids as shown in Fig 3.19.

3.2.3 HV feedthroughs for cathode and gate electrodes

The anode mesh and bottom screening grid are grounded outside the shielding structure through the same Kyocera feedthrough with temperature sensors and level meters. This allows us to manipulate the voltage on these two electrodes if necessary.

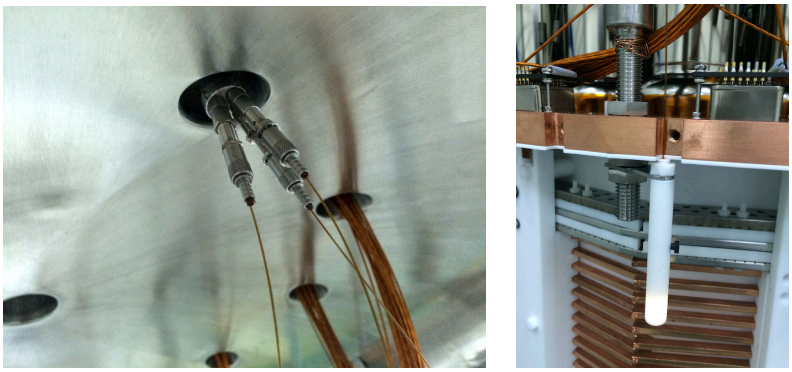

(a) (b)

Figure 3.19: Photos of the inner side of fiber optics feedthrough (a) and a PTFE diffuser (b).

The gate is connected to a CAEN HVPS (Mod. N1470AR) through an MPF SHV-20 coaxial feedthrough on the IV and another one on the port near the motion feedthrough as shown in Fig 3.11(b) and Fig 3.20.

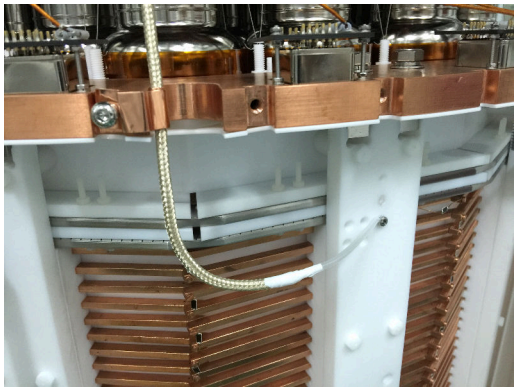

Figure 3.20: The connection between the gate grid and the wire.

The cathode is connected to a MATSUSADA HVPS (Mod. AU100-N3) through a custom-made feedthrough directly from gaseous xenon to the air as shown in Fig 3.21. The cable is guided in a 2.75″ tube using the same port in the shielding structure with the calibration tubes.

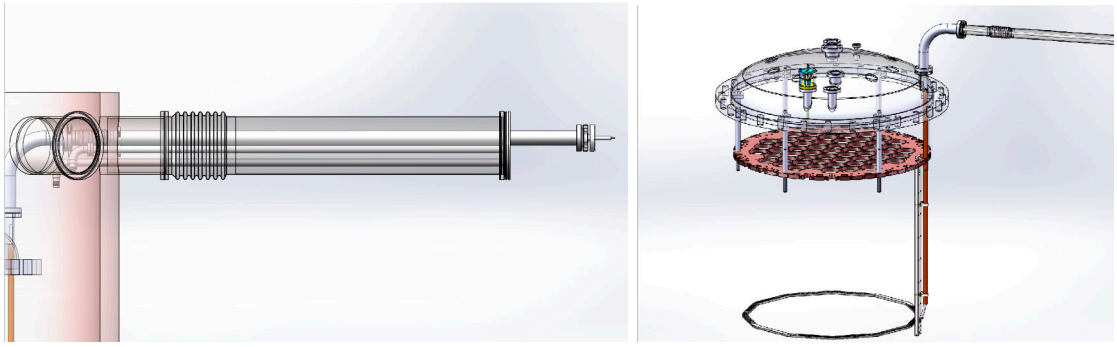

(a)

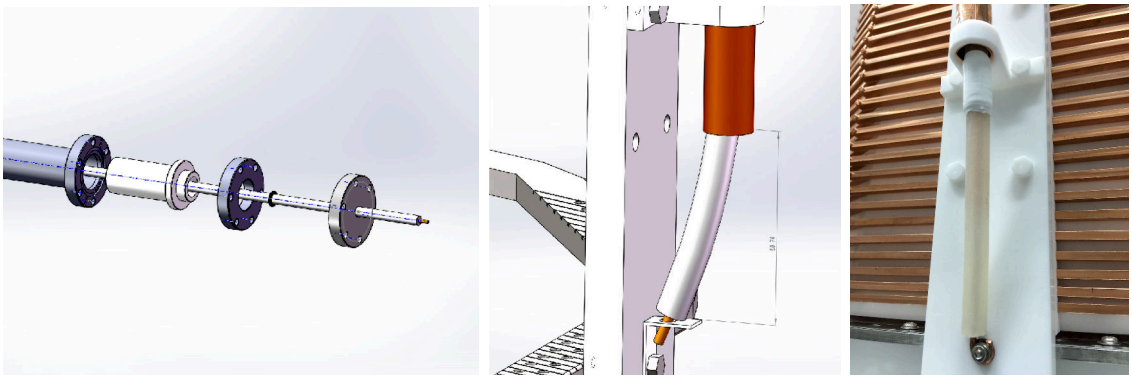

(b)

Figure 3.21: The design of the cathode connection tube (a), the cathode feedthrough and the connection between the cable and the electrode (b).

3.3 Calibration system

In PandaX-II, we installed two PTFE tubes with a 25 mm inner diameter on the interior surface of the outer Cu vessel at two different heights (15 and 45 cm above the height of the cathode electrode) for the external calibration sources (Fig 3.22(a)). The foot-pieces are fixed on the surface of Cu vessel using Epoxy as in Fig 3.22(b). Two PTFE tubes are sealed with four stainless steel tubes as in Fig 3.22(c). The four stainless steel tubes share the same port with the cathode

tube in the shielding structure as shown in the left plot in Fig 3.21(a).

(a) (b) (c)

Figure 3.22: Two PTFE tubes mounted on the interior surface of the Cu vessel (a), the foot-pieces fixed on the Cu vessel (b) and the connection between PTFE tubes and stainless-steel tubes (c).

Two stainless-steel wires in two loops guide the source within the size of 8 × 10 mm (d×length) capsule. We made eight marks on both up and down loops to indicate the azimuthal positions of sources.

Besides the tubes for external calibration sources such as AmBe neutron source, ^{137}Cs, ^{60}Co, and ^{232}Th sources, we also designed an internal injection setup embedded with the circulation loop2. It allows us to inject radioactive noble gas isotopes before getter and tritiated methane after the purifier as shown in Fig 3.23.

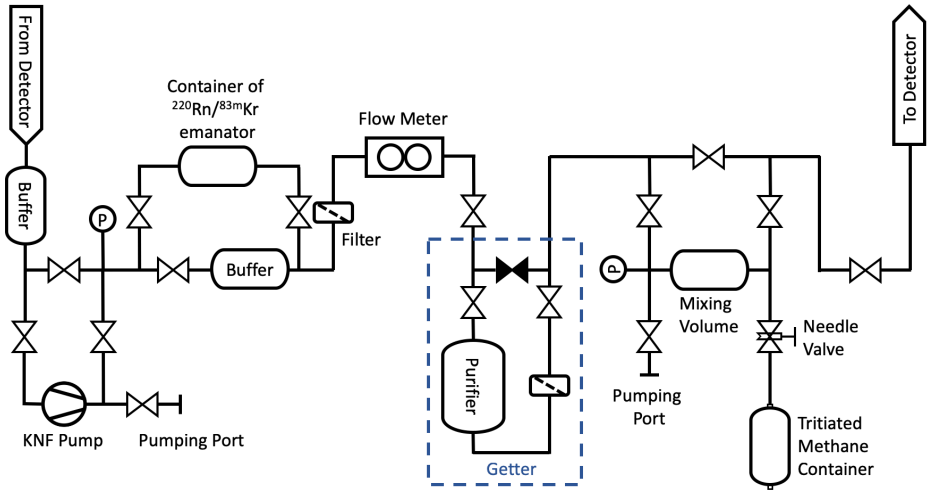

Figure 3.23: The schematic diagram of the injection setup embedded in the circulation loop 2 of the PandaX-II detector.

Chapter 4: Data analysis and WIMP search result

The data acquisition system in PandaX-II records waveforms of all PMTs with triggers. For the 60 cm depth of the TPC, the maximum time separation between $S1$ and $S2$ is estimated to be 350μs. The length of each readout window is set to 1 ms, with 500 μs before and after the trigger. The trigger is generated primarily on $S2$s for low-energy events $<$ 10keVee (electron equivalent energy) with a trigger threshold of 79 photoelectrons (PEs), and higher-energy events are mostly triggered by $S1$s.

The data processing and signal selection framework is firstly converting information from the raw waveforms of individual PMTs into photoelectrons and timing for $S1$s and $S2$s, etc. The horizontal vertex position is reconstructed based on the charge pattern of $S2$ on the top PMT array. The single photoelectron gain (PMT gain) is obtained by integrating the area of the waveform below the baseline for the single photoelectron signals. PMT gains are calibrated by guiding blue photons from the light-emitting diodes through optical fibers to the detector periodically. After the gain correction, a threshold of 0.25 PE/sample in amplitude, roughly corresponding to a single channel threshold of 0.5 PE, is used for finding PMT hits from each waveform. Clusters of time-correlated hits are grouped into individual

signals, which are tagged into either the $S1$ signal, $S2$ signal, or noise based on the shape of the summed waveform over all channels. The discrimination between $S1$ and $S2$ signals relies on the full-width-10%-maximum of the waveform. At least three PMT hits are required for a valid $S1$ signal to suppress random coincidence among PMTs. Veto PMTs hits are not used in the clustering. However, any hit in the veto array that occurs during the entire width of an $S1$ signal will veto an event. The threshold to generate a veto was estimated to be $\sim$150 keVee in the skin region from a comparison between the data and Monte Carlo (MC) simulation.

Mono-energetic γ peaks were used to calibrate the detector response. The 164 and 236 keV γ events were uniformly distributed in the detector and were used to produce a uniformity correction for the $S1$ and $S2$ signals in Run9 and Run10. A three-dimensional correction map was created for $S1$. For the $S2$ signals, the vertical uniformity correction was obtained by fitting $S2$ dependence on the drift time using the electron lifetime as an exponential decay constant τ. The $S2$ distribution in the horizontal plane was used to produce a two-dimensional correction map in the X-Y plane.

For each event, the electron equivalent energy can be reconstructed using the combined energy formula. The photon detection efficiency (PDE), the electron extraction efficiency (EEE), and the single-electron gain (SEG) in PE/e are the three key detector parameters in the formula derived from a χ^2-fitting to multiple γ peaks.

An AmBe neutron source was deployed through two PTFE tubes, and tritiated methane was injected to calibrate the detector response to NR and ER events.

The NEST-based modeling of background and signal was built using the ER and NR calibration data. The investigation of backgrounds provided the estimated composition of the final candidate events as inputs to the final statistical analysis. We constructed an un-binned likelihood function and used the CL_s technique to set the exclusion limit on the WIMP-nucleon cross section.

In this chapter, I will present details on several steps in the data process chain that I deeply involved and discuss dark matter search results.

I will start with the calibration and the stability of the gains during Run9 and Run10. Some PMTs ran in relative low gains in Run10 which caused an inefficiency from a data suppression firmware in the data acquisition system, named zero length encoding (ZLE). We use the LED signals with or without ZLE suppression to calibrate this efficiency on $S1$s. And for $S2$s, the charge of high gain PMTs is used as the estimator, and the result indicated a negligible effect. I developed a data-driven algorithm for the X-Y position reconstruction named photon acceptance function (PAF). PAF algorithm allows the events to be reconstructed in the entire physical boundary of the sensitive volume of the detector and extends the fiducial volume by 20%. The algorithms for uniformity correction and the derivation of two parameters for energy reconstruction (PDE and EEE) will be described. Finally, the low background is crucial for rare event search experiments like PandaX, the study on intrinsic ER backgrounds from Kr, Rn, and ^{127}Xe will be presented.

4.1 PMT gain calibration

The first step of the data processing chain is to convert information from the raw waveforms of individual PMTs into photoelectrons (PEs) and timing for $S1$s and $S2$s, etc. In this section, I will describe the calibration of PMT gains and present the stability of the gains during Run9 and Run10.

The PMT gains are calibrated by photons from a light-emitting diode (LED) fed through optical fibers to the detector periodically. The LED is driven by a 200 Hz TTL pulse generator which emits blue photons (about 430 nm) with lower energies than xenon scintillation photons centered at 178 nm [100]. The photons from LED propagate along the three optical fibers to the PTFE diffusers in the skin region outside the TPC and diffuse into the TPC through the gap on the top of the field cage around the anode grid as shown in Fig 3.19(b). A forced trigger is aligned to the pulses recording the waveforms of all PMTs. To optimize the occupancy of PMTs with different distances to the diffusers, we varied the voltage on the LED driver to change the luminosity of the LED. For each luminosity, 50,000 waveforms are taken for each PMT, and the process takes about 4 min. The 3″ PMTs receive photons from PTFE diffusers more uniformly than 1″ PMTs in the skin region mainly due to the geometry of the configuration. A mini-calibration means that we only calibrate 3″ PMTs at three sets of different LED luminosities. A full calibration stands for ten sets of different luminosities. In Run9, we made full calibrations every three days. In Run10, we made daily mini-calibration and a full calibration each week.

Fig 4.1 shows typical spectrums of a 3″ and a 1″ PMTs. The black histograms are raw spectrums. The red curves are fitting curves with three Gaussians for the pedestal, single photoelectron (SPE), and double photoelectron (PE) peaks. The charge in the unit of ADC bit can be converted to the number of electron per photon electron (e^-/PE) by taking into account 50 Ω as the resistance on the PMT base and DAQ sample width of 10 ns. The gains and their errors were filled into the database

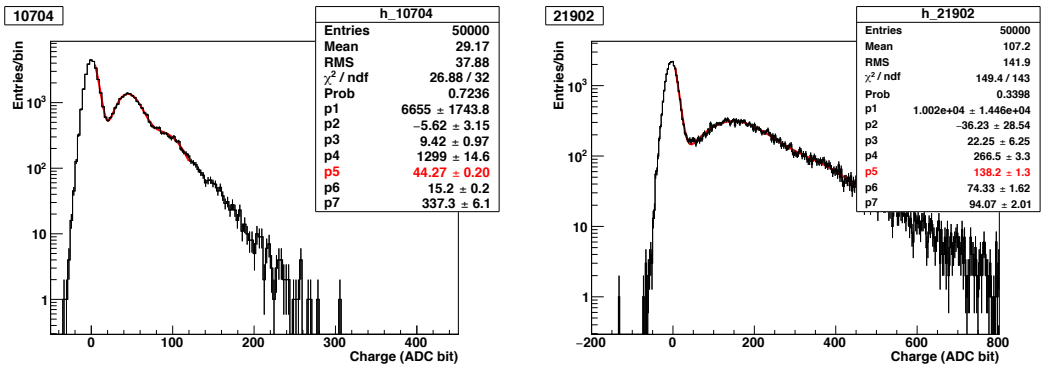

(a) (b)

Figure 4.1: Typical spectrums of a 3″ (a) and a 1″ (b) PMTs (black histograms). The red curves are multi-Gaussian fitting. In legend, "p5" in red is the mean value of the SPE Gaussian in ADC·bit/PE.

for PMT hit finding and signal calculation in the upper level of data analysis. After the replacement of amplifiers in early 2017, some PMTs still had to be run at a lower HV in Run10 to avoid the spurious discharge signals, possibly due to the damage on the insulation on the feedthrough. The gain evolution of two typical PMTs is shown in Fig 4.2.

The means and the standard deviations of these two PMTs are given in Tab 4.1 along with the overall gain stability of all PMTs in Run9 and Run10. The standard

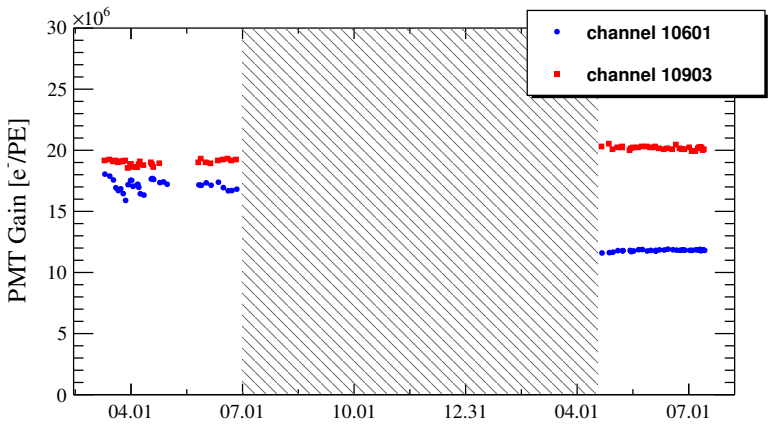

Figure 4.2: The gain evolution of two typical PMTs during Run9 and Run10.

Table 4.1: Gain Stability in Run9 and Run10 in the unit of $\times 10^6$ e^-/PE.

Channel	Run9		Run10	
	Mean	STDEV	Mean	STDEV
10601	17.29	1.05	11.80	0.07
10903	18.53	1.96	20.16	0.12
All PMTs	13.36	3.50	9.00	5.31

deviations of all PMTs in Run9 and Run10 are not the average time variation of all PMTs but the dispersion of the gain among all active PMTs in Run9 and Run10. The average time variations overall active PMTs are 12.1% and 7.3% in Run9 and Run10, respectively.

4.2 ZLE efficiency

Due to lower HV on the PMTs during Run10, the ZLE firmware introduces a charge suppression, a systematic effect that has to be taken into account in the signal modeling. In this section, I will present how we determine the ZLE efficiencies on $S1$s and $S2$s.

The ZLE causes inefficiency in small signals, especially on $S1$s. For $S1$s, we used the LED signals obtained with or without ZLE to calibrate this efficiency. And for $S2$s, the charge of high gain PMTs is used as the estimator, and the result indicates a negligible effect. The ZLE efficiencies on both $S1$s and $S2$s are implemented in the Monte Carlo (MC) to generate the probability density function (PDF) for signal and background to fit the DM search data.

4.2.1 Inefficiency from zero-length encoding

During the regular data taking, a value of 20 ADC counts relative to the baseline has been set as the threshold below which the ZLE firmware of the CAEN V1724 digitizers suppressed the data recording [101].

The sample rate of DAQ in the PandaX-II is 100MHz. The maximum delay time between $S1$ and $S2$ is about 360 μs, which varies according to the drift electric field in the liquid. In PandaX-II, the length of the data recording window is 1 ms. Fig 4.3 shows two segments of the waveform of one PMT. The baseline of that

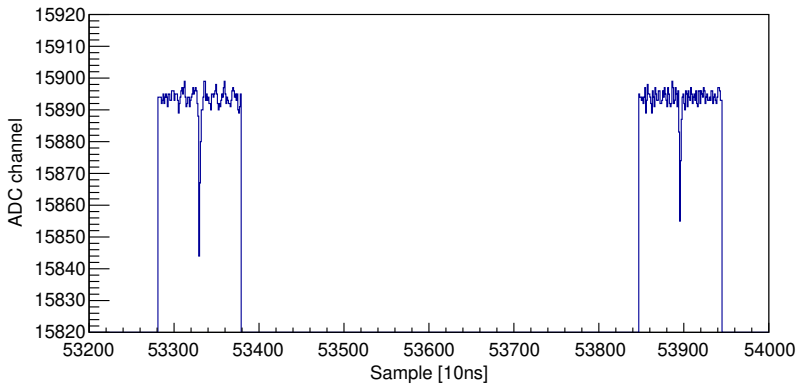

Figure 4.3: The waveform of two consecutive signals with ZLE on one PMT. The ZLE suppresses the waveform in the interval where no sample above the ZLE threshold (20 ADC). And two segments of the waveform around the signal are recorded.

PMT in the DAQ configuration is at 15895 ADC. Thus, the ZLE threshold is at 15875 ADC. The waveform within 48 samples before and after the sample over the ZLE threshold is suppressed. As summarized in Tab 4.1, the average gain of the 3″ PMTs is 13.36×10^6 e^-/PE and 9.00×10^6 e^-/PE in Run9 and Run10, respectively, after the $\times10$ amplifier. The average ZLE threshold corresponds to 0.4 SPE in Run9, and 0.6 SPE due to lower gain in Run10. The ZLE efficiency is defined as the ratio of the number of detected signals to the total number of true signals. For $S1$-like signals, the ZLE efficiency has been studied channel-by-channel using the difference between LED calibration runs with and without ZLE. For $S2$-like signals, a data-driven model based on the charge on high gain PMTs as an estimator has been developed to characterize the ZLE efficiency.

4.2.2 ZLE efficiency on $S1$

The $S1$ pulses are narrow pulses with $\sim$100 ns in width. They can be simulated by fast LED pulses with similar time profile. The ZLE efficiency on the $S1$-like signal was derived by taking the ratio between charge distribution of $S1$ signal with and without ZLE from very low intensity to high intensity LED runs.

LED with or without ZLE

Fifteen sets of LED runs under different luminosities were taken. The same forced trigger which synchronized with the LED driving pulses was used as in the gain calibration runs. The data recording window was set to be 5 μs, and the LED driving frequency was 200 Hz. The photon signals from LED diffusers were roughly

in the center of the data recording window. In the no ZLE case, the entire waveform of the record window with 500 samples was recorded. In the ZLE case, the segment contains the photon signal from LED along with 48 samples before and after the samples above the ZLE threshold. The average ADC of the first and last 10 samples on the segment was calculated to be the pedestal value. The area was calculated as the integral of samples (pedestal subtracted) in the signal interval on the waveform. For each PMT, one data set under certain LED luminosity was selected where there is sufficient statistics in the spectrum around the turn-on edge of the efficiency.

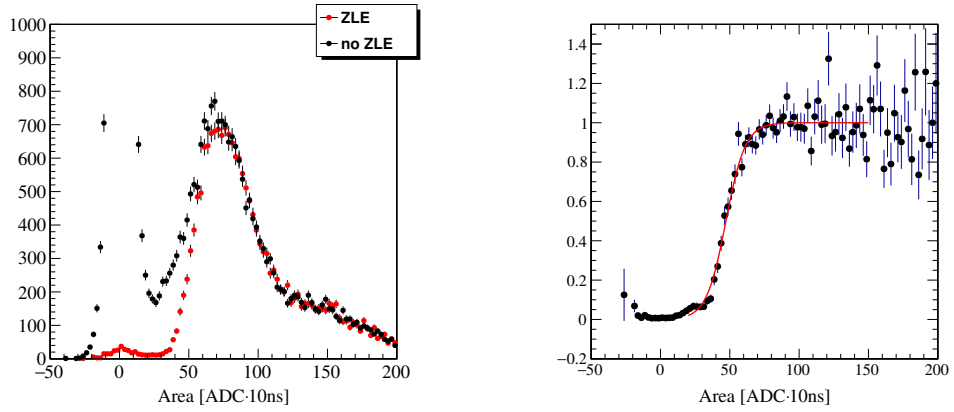

(a) The spectrum with or without ZLE. (b) ZLE efficiency fitting

Figure 4.4: The pulse area spectrums with and without ZLE for one typical channel (a) and the ratio histogram (b). The black histogram is the spectrum without ZLE, and the red one is with the ZLE. The red curve indicates the Fermi-Dirac fitting of the ratio histogram.

Fig 4.4 shows the measured ZLE efficiency of one channel. The pedestal peak around zero for no ZLE was out of the range of the Y-axis for visual clarity, and it was almost entirely suppressed in the ZLE case as expected. The channel-by-channel ZLE effect on $S1$-like signals was characterized using the so-called Fermi-Dirac (F-D)

function as

$$\epsilon^i(S1) = \frac{1}{1 + \mathrm{e}^{-\frac{S1 - p_0^i}{p_1^i}}}, \tag{4.1}$$

where $\epsilon^i(S1)$ is the ZLE efficiency on $S1$ for the i^{th} PMT and $p^i_{0,1}$ are the parameters of the F-D for the i^{th} PMT.

For some channels with the high noise level, the pedestal peaks are not entirely suppressed by ZLE. Thus, the modified F-D function was used to fit the ratio histogram as

$$\epsilon^i(S1) = \frac{1 - p_2^i}{1 + \mathrm{e}^{-\frac{S1 - p_0^i}{p_1^i}}} + p_2^i, \tag{4.2}$$

where p_2^i is the offset at negative infinity of the F-D function for the i^{th} PMT.

The overall ZLE efficiency on $S1$ in data and MC

In the LED runs, the overall ZLE efficiency was calculated using the ratio of the charge of $S1$ with and without the ZLE. For each calibration data set under certain LED luminosity, the average total charge without (with) the ZLE was denoted as $S1_{\text{true}}$ ($S1_{\text{eff}}$). The pedestal peaks of some PMTs were not centered precisely at zero, thus did not vanish after the integral. The pedestal peak contributions to the $S1_{\text{true}}$ and $S1_{\text{eff}}$ were subtracted by a Gaussian fitting and taken as the systematic error. The errors of the overall ZLE efficiency were propagated from the errors of the $S1_{\text{true}}$ and $S1_{\text{eff}}$ which dominated by systematics.

The channel-by-channel efficiency was combined in a toy simulation to check if we can reproduce the measured efficiency above. The photons were distributed according to the LED hit pattern as in Fig 4.5.

The hit pattern was stable to the luminosity of LED, and on average, the top

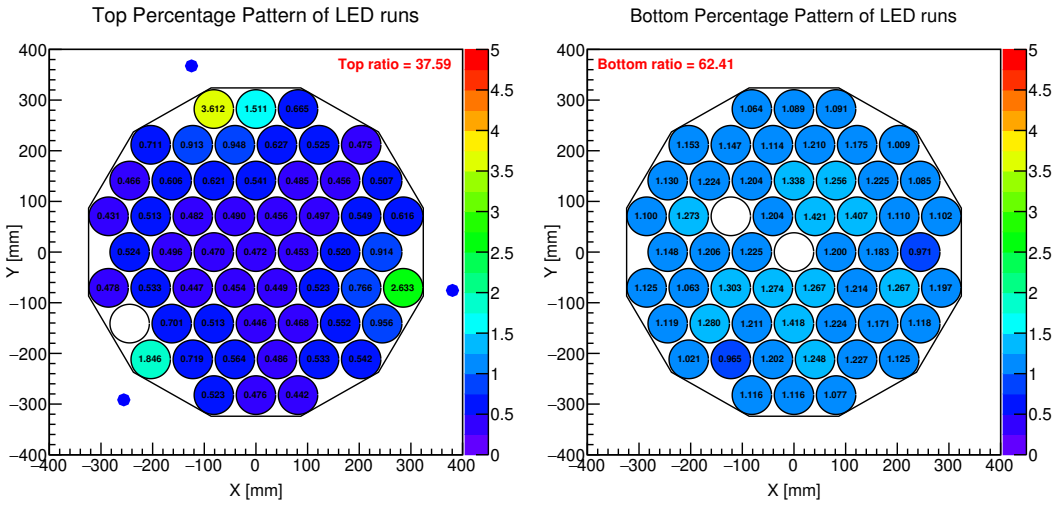

Figure 4.5: The hit pattern of the top (left) and bottom (right) PMT arrays in the LED runs. The three blue circles outside the dodecagon boundary of TPC indicate the position of three LED diffusers. The value and color in each PMT represent the percentage of photons received by the PMT in LED runs. The Z-axis ranges were fixed from 0 to 5.

array collected 37.6% of the total detected photons. Three PMTs with no value and color were inhibited during Run10. The one on the top array was inhibited due to the broken base. The one in the center of the bottom array was inhibited due to the multi-pulsing problem, and the last one in the bottom array was inhibited due to the broken base. Charge on each PMT was calculated by smearing the number of hit photons by the measured single-photon resolution (0.33 PE). The direct sum of the smeared charge on each PMT was denoted as $s_{1\text{true}}$. On the other hand, the modified F-D (Eq 4.2) of each PMT was applied to the smeared charge. The sum of the suppressed charge was denoted as $s_{1\text{eff}}$. The original F-D as in Eq 4.1 was used to calculate the systematic error of $s_{1\text{eff}}$.

In Monte Carlo (MC), we calculate the overall ZLE efficiency in each $S1$ bin by taking the ratio of the average $S1_{\text{eff}}$ over $S1$. The error of the overall ZLE efficiency

in each bin was dominated by the systematics propagated from the systematic error of $s_{1\text{eff}}$. The black shaded area is the 1-σ band of the overall ZLE efficiency. As shown in Fig 4.6, the simulation yields a reasonable agreement to the LED measurement.

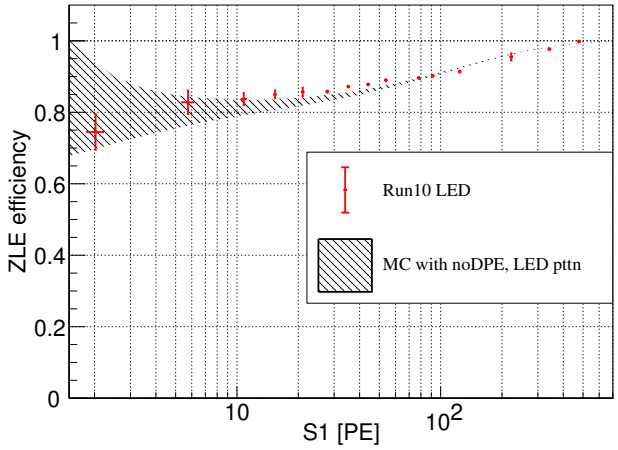

Figure 4.6: The ZLE efficiency, defined as the ratio of the average $S1$ with and without ZLE, vs. $S1$ (without ZLE), measured from the LED data in Run 10 (red). The black shaded area is the 1-σ band of the overall ZLE efficiency in the MC.

For the modeling of real $S1$-like signals in the DM search, we distributed photons according to the average pattern of the 164 keV $^{131\text{m}}$Xe events (uniformly distributed and barely affected by ZLE). The double photoelectron emission (DPE) fraction was taking into account before the resolution smearing. Since DPE should suppress the ZLE effects, the ZLE efficiency for real $S1$s from xenon was higher than that in the LED case.

Double PE emission

R11410-20 PMT from Hamamatsu was reported to have the DPE phenomenon for vacuum ultra-violet scintillation photons from xenon in [102]. In PandaX-II, we studied this effect using $S1\text{s} \geq 3$ PMT hits to avoid dark hits faking DM search data. The smallest signals were selected with only one PMT hit on the top(bottom)

array. Only PMTs with high gains were analyzed to prevent the ZLE effect on the fraction calculation. An example histogram is shown in Fig 4.7.

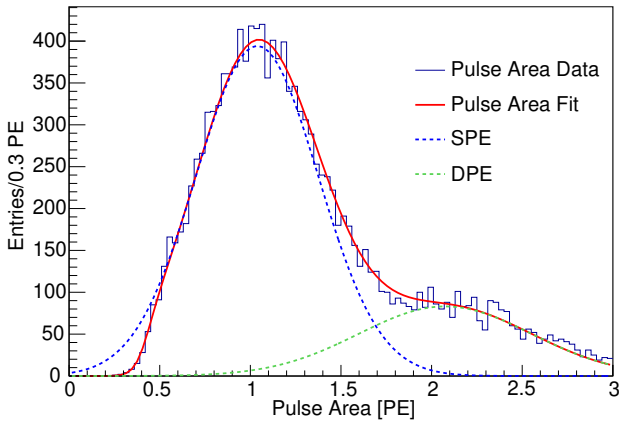

Figure 4.7: Charge spectrum of 7 PMTs with SPE efficiencies higher than 90% with 20.503 day live-time. The fitting function was constructed with two Gaussian functions and an F-D function. The dashed blue line indicates the SPE component and the dashed green line stands for the double PE component.

The DPE fraction was calculated using the double PE area divided by the SPE area. The systematic error was derived by taking the difference among DPE fraction varying the PMTs and runs. The final DPF is $21.7 \pm 2.2_{\text{sys.}} \pm 0.4_{\text{stat.}}$ %.

In contrast, the DPE fraction in LED runs was found to be negligible and consistent with the random coincidence estimation.

4.2.3 ZLE efficiency on $S2$

The electroluminescence of extracted electrons generated $S2$s. A cloud of electrons suffers from field non-uniformity, diffusion, track orientation, and recombination during the process from the production of electron-ion pairs and drifting under the electric field. Therefore, the $S2$s with a similar charge can have widely

different time profiles, especially for low energy events. The single electron gain in Run10 is 23.9 ± 0.5 PE/e$^-$. Thus, the $S2$ signal is usually much larger and broader than the $S1$ signal of the same event.

Fig 4.8(a) shows a typical waveform of an $S2$ signal on the top PMT array. Fig 4.8(b) shows the waveform of one top PMT of the same $S2$ signal. Note that for a small $S2$ signal, the waveform exhibits a comb-like shape with multiple peaks. In the example in Fig 4.8(b), a small peak was recorded right before the end of the segment though it is below the ZLE threshold since there was another larger enough pulse before it which enables the recording of 48 samples after the threshold crossing. Such complexity is difficult to be simulated by LED photons.

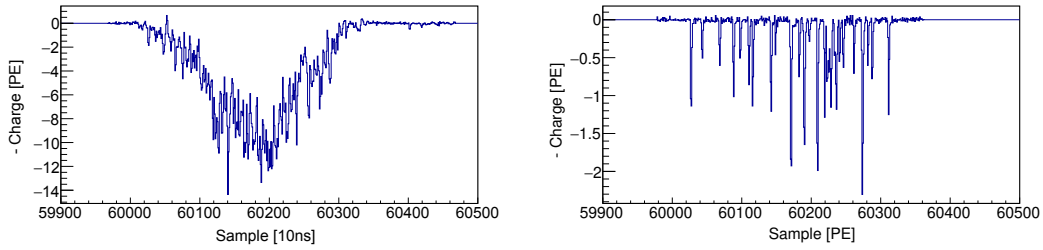

(a) The sum waveform of top PMT array (b) The waveform of one top PMT

Figure 4.8: The sum waveform of an $S2$ signal in the top PMT array (a) and a segment in the raw waveform of a single top PMT of the same $S2$ signal (b). The Y-axis has been converted to PE using the gain of individual PMT.

A data-driven approach was developed to derive the overall ZLE efficiency on $S2$. Calibration runs of tritiated methane were used, since the high statistics of low energy events and their uniform distribution. PMTs with gains above 13.7×10^6 e$^-$/PE were tagged as good PMTs which have negligible inefficiencies from ZLE. The sum charge on those PMTs, scaled to the total number of active PMTs,

is denoted as $S2$. On the other hand, $S2_{\mathrm{raw}}$ means the sum charge on all active PMTs. At high energy region with large $S2$s, the ratio of $S2/S2_{\mathrm{raw}}$ plateaued at 1.1387, indicating the bias of the scaling which could be either from geometry or light leakage. We further applied this factor to $S2$, which is denoted as $S2_{\mathrm{scaled}}$, as an estimator for true $S2$ free of ZLE suppression.

In Fig 4.9, the event-by-event ratio of $S2_{\mathrm{scaled}}/S2_{\mathrm{raw}}$ was profiled in each bin in the X-axis and fitted by an F-D function. The p_0 and p_1 of the F-D function are -11.0 ± 0.6 PE and 10.8 ± 0.5 PE, respectively.

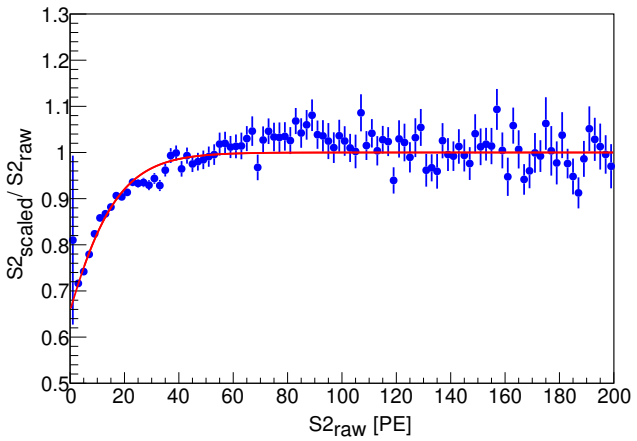

Figure 4.9: The overall ZLE efficiency normalized to $S2_{\mathrm{raw}}$.

Based on this, the inefficiency at 40 PE for $S2$ signals is less than 1%. The lower cut on $S2_{\mathrm{raw}}$ in a regular event was set to 100 PE for DM search data. Therefore, the overall ZLE efficiency on $S2$ has a negligible effect on DM search.

4.3 Reconstruction of horizontal vertex position

One of the main advantages of dual-phase noble gas TPCs is the accessibility of the three-dimensional position of events as discussed in Sec 1.5. The vertex

position information is indispensable during event selection and fiducialization. The vertical position of the event was obtained from the delay time between $S2$ and the $S1$ multiplied by the drift speed of the electron cluster under the specific drift field. The horizontal position in the X-Y plane is reconstructed from the hit pattern of the $S2$ signal on the top PMT array. The algorithm based on the statistical model was developed in PandaX-I. In this section, I will describe a new data-driven algorithm developed in PandaX-II, named PAF, based on a similar statistical model but with various improvements. This new position reconstruction algorithm enlarged the fiducial volume (or exposure) by 20% in the later analysis.

4.3.1 Top PMT array

Two identical arrays of PMTs were placed above and below the TPC respectively to detect scintillation photons in the sensitive volume. 55 3-in PMTs consists of the top PMT array. The distance between the nearest pairs is 81.5 mm from the center to the center. The 12 PTFE panels defined the cross section of the sensitive volume to be a dodecagon, and the minimum distance between PMTs and panels is 41.68 mm. Fig 4.10(a) shows that the top array has six corners with inadequate PMT coverage. A typical hit pattern of an $S2$ signal on the top PMT array is shown in Fig 4.10(b). Both top and bottom 3″ PMTs collect lights from $S2$ signals. Due to the configuration of TPC, $S2$ signals usually happened at about 50 mm below the top PMT array which is much closer than it to the bottom array. Therefore, the hit pattern on the top PMT array is more sensitive to the horizontal position of

$S2$ and is used for position reconstruction.

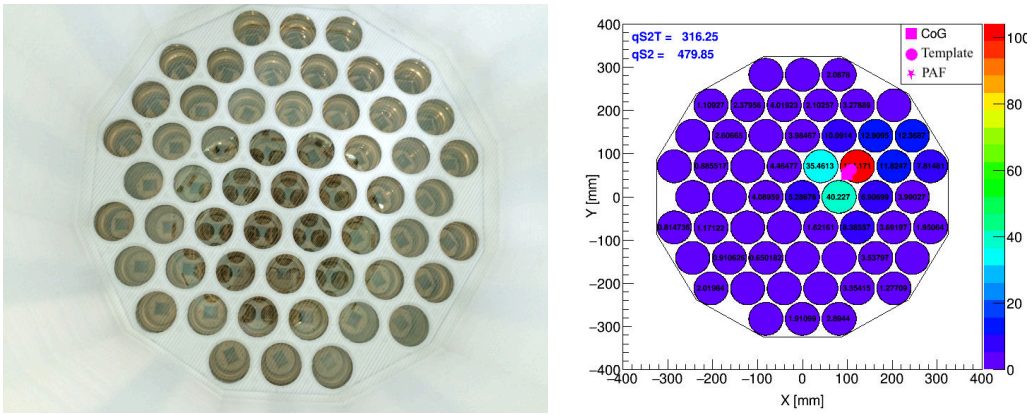

(a) (b)

Figure 4.10: A photo of the top PMT array along with the PTFE panels (a) and a hit pattern of an $S2$ signal on the top PMT array (b).

4.3.2 Events reconstruction methods

The goal of position reconstruction is to find the most likely position $\vec{r} = (x, y)$ for an event given its hit pattern, i.e., the 55 output signal $\{q_i\}$ from the top PMTs. Several methods can be used to infer the best position $\vec{r}$.

Center of gravity

The Center of Gravity (CoG) method is a simple, fast, and robust algorithm for position reconstruction. It reaches a good effect in the central region. The position of an event can be estimated by the weighted average of the light distribution across the PMT array as

$$x = \frac{\sum_i X_i \cdot q_i}{\sum_i q_i}, \quad y = \frac{\sum_i Y_i \cdot q_i}{\sum_i q_i}, \tag{4.3}$$

where (X_i, Y_i) are the coordinates of the i^{th} PMT. However, the CoG position tends to centralize the events especially near the boundary of the TPC. Therefore, we

developed the statistical method for unbiased position reconstruction.

Maximum likelihood

For an event at position $\vec{r}$ with total detected N photons, the probability of the i^{th} PMT detecting n_i photons is well approximated by the Poisson distribution:

$$P_i(n_i) = \frac{\mu_i^{n_i} \cdot \mathrm{e}^{-\mu_i}}{n_i!}, \tag{4.4}$$

where $\mu_i = N\eta_i(\vec{r})$ is the expectation value of the photon number detected by the i^{th} PMT. The expected percentage is $\eta_i(\vec{r})$ for the i^{th} PMT. $\{N, \vec{r}\}$ are the parameters to be inferred by maximizing the likelihood. For a given hit pattern $\{n_i\}$, the likelihood function can be constructed as

$$\ln \mathcal{L} = \sum_i \ln P_i = \sum_i (n_i \ln \mu_i - \mu_i) - \sum_i \ln(n_i!). \tag{4.5}$$

Taking into account that $\mu_i = N\eta_i(\vec{r})$, we can write

$$\ln \mathcal{L}(N, \vec{r}) = \sum_i (n_i \ln(N\eta_i(\vec{r})) - (N\eta_i(\vec{r}))) - \sum_i \ln(n_i!). \tag{4.6}$$

The best estimation of N at given $\vec{r}$ can be obtained straightforwardly by

$$\frac{\partial \ln \mathcal{L}(N, \vec{r})}{\partial N} = \sum_i n_i \frac{\partial \ln N\eta_i(\vec{r})}{\partial N} - \sum_i \eta_i(\vec{r}) = 0, \tag{4.7}$$

i.e.,

$$N = \frac{\sum_i n_i}{\sum_i \eta_i(\vec{r})} = \frac{\mathrm{qS2T}}{P(\vec{r})}, \tag{4.8}$$

where qS2T$= \sum_i n_i$ and $P(\vec{r}) = \sum_i \eta_i(\vec{r})$. By substituting N into Eq 4.6, we have

$$\ln \mathcal{L}(\vec{r}) = \mathrm{qS2T} \sum_i \frac{n_i}{\mathrm{qS2T}} \ln \frac{\eta_i(\vec{r})}{P(\vec{r})} + \sum_i n_i \ln \mathrm{qS2T} - \mathrm{qS2T} - \sum_i \ln(n_i!). \tag{4.9}$$

The maximizing likelihood is now to find $\vec{r}$ such that

$$\nabla \ln \mathcal{L}(\vec{r}) = \mathrm{qS2T} \cdot \nabla \sum_i \frac{n_i}{\mathrm{qS2T}} \cdot \ln \frac{\eta_i(\vec{r})}{P(\vec{r})} = 0. \tag{4.10}$$

Considering qS2T is a constant in each event, and we transfer the problem to that finding the optimistic parameter $\vec{r} = (x, y)$ which minimizing $-\ln \tilde{\mathcal{L}}$ where

$$-\ln \tilde{\mathcal{L}}(\vec{r}) = -\sum_i \frac{n_i}{\mathrm{qS2T}} \ln \frac{\eta_i(\vec{r})}{P(\vec{r})} \tag{4.11}$$

For this statistical model, we developed two different algorithms to obtain the expectation of a hit pattern at a given position $\vec{r}$, i.e., $\{\eta_i(\vec{r})\}$. They are Template and Photon Acceptance Function (PAF) described in detail below.

Template

The Template algorithm is based on the Monte Carlo light simulation to derive $\{\eta_i\}$ as the anticipated hit pattern at all positions in the sensitive region. The simulation took into account geometry and the reflectivity of all materials. It generated the $S2$ signal inside the 5.5 mm gas gap between the gas-liquid surface and the anode plane. And the Rayleigh scattering, absorption length and the reflectivity of the PTFE were optimized to be 40 cm, 2.8 m and 94% according to the RMS (in Fig 4.11(a)) and top-to-bottom ratio (TBR in Fig 4.11(b)) from the charge distribution of $S2$ signals. We divided X-Y planed into certain divisions and derived one template $\eta_i(\vec{r_j})$ for the j^{th} division centering at $\vec{r_j} = (x_j, y_j)$ by averaging the light distribution patterns of all 55 PMTs inside the j^{th} division. We scanned over all divisions and found the position with the minimum $-\ln \tilde{\mathcal{L}}(\vec{r})$ defined in Eq 4.11.

Though the free parameters in MC were tuned to match the hit patterns with real data, the expectation $\{\eta_i(x, y)\}$ is more dispersed than the detected hit pattern

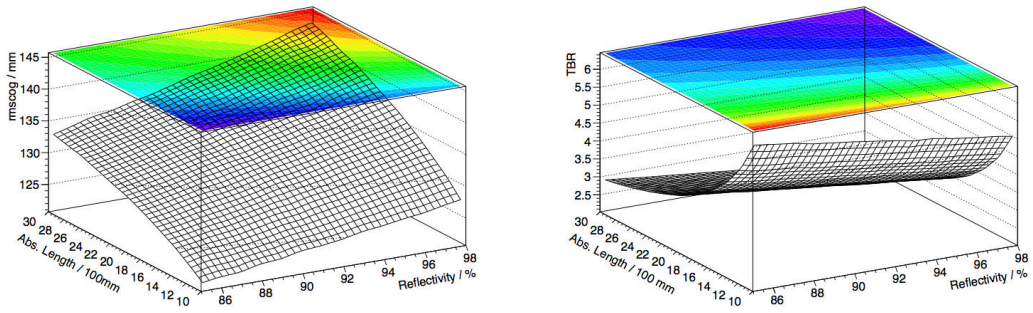

(a) (b)

Figure 4.11: The optimization of the reflectivity of the PTFE and the absorption length according to RMS (a) and TBR (b).

$\{n_i\}$ in general. This discrepancy might arise from the lack of a precise description of light leakage on the top part of TPC in MC. Therefore, a data-driven derivation of the photon acceptance function (PAF), $\{\eta_i(x, y)\}$, was developed.

4.3.3 Photon acceptance function

Compared with Template, PAF is a data-driven algorithm that can avoid the mismatch between the simulated and detected hit patterns. PAFs, $\{\eta_i(\vec{r})\}$, are derived after several iterations of fitting and reconstructing the position of training samples.

The uniformly distributed training samples were selected from Run9 while all top PMTs were well-functional. Due to the cosmogenic excitation, radioactive xenon isotopes were very active at the beginning of Run9. We used 164 keV events from the de-excitation of ^{131}Xe as the samples. They are uniformly distributed in the entire TPC, and they did not suffer from the saturation effect for the relatively

lower energy.

We started from the CoG positions of samples to fit $\{\eta_i^{(0)}(\vec{r})\}$ in the parametric form [103]:

$$\eta(r) = A \cdot \exp(-\frac{a \cdot \rho}{1+\rho^{1-\alpha}} - \frac{b}{1+\rho^{-\alpha}}), \quad \rho = \frac{r}{r_0} \tag{4.12}$$

where r is the distance between the PMT center and $\vec{r}$. And A, r_0, a, b, and α are free parameters. We then reconstructed the position of all events and then used the new positions to derive updated $\{\eta_i^{(1)}(r)\}$. So on and so forth till the convergence criteria truncated the iteration.

Image PMTs

For peripheral PMTs, the isotropic assumption in Eq 4.12, i.e., $\{\eta_i(\vec{r})\}$ is only the function on r, is not valid due to the PTFE reflection. We constructed image components based on the geometrical configuration. The summation of the original and image part is the PAF for the i^{th} PMT, i.e.,

$$\eta_i(\vec{r}) = \tilde{\eta}_i(r) + \hat{\eta}_i(r_{\text{im}}) \tag{4.13}$$

where $\tilde{\eta}$ ($\hat{\eta}$) is the original (image) part as Eq 4.12 and r_{im} is the distance between the event and the center of the image PMT. The location of the image PMTs is shown in Fig 4.12. For green and blue PMTs, image ones have equal distance to the closest PTFE reflection panel as themselves. Red PMTs are near the corners of two PTFE panels, and thus their images are symmetric to the intersection points.

The image parts have the same form as the original ones in Eq 4.12 but smaller weights. We determined the weights of the image parts by fitting the R^2 distribution of the uniform training samples. Fig 4.13 shows two examples of PAF

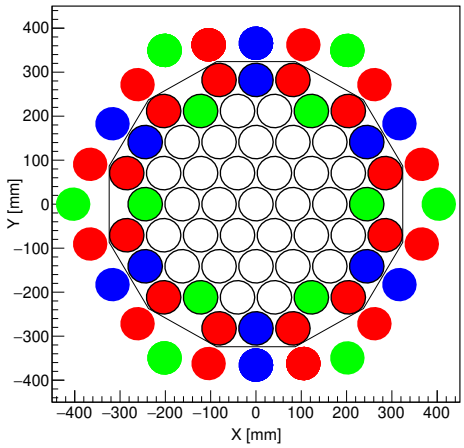

Figure 4.12: The schematic diagram of the positions of image PMTs.

for two peripheral PMTs.

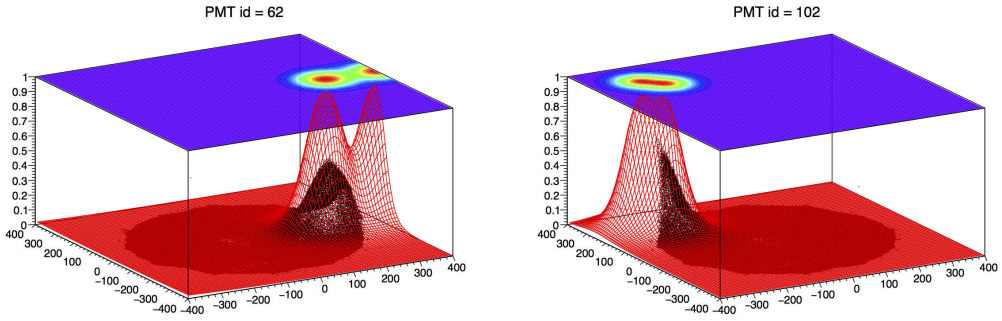

Figure 4.13: The PAFs of PMT62 (left) and PMT102 (right) which are made of the superposition of the original and image parts. The black dots are the distribution of the charge percentage of the specific PMT. PAFs indicated by the red lines were scaled to 1 for better visualization. The contours of PAFs were plotted on the top planes.

4.3.4 Comparison of different algorithms

The reconstruction algorithm based on PAF yields a smoother and more uniform R^2 distribution of training samples than Template and CoG. CoG pushed events to the center of the geometry and Template caused the concentration of events near the closest template's position. Moreover, Template was generated in

polar coordinates, and the concentration caused a comb-like shape R^2 distribution as shown in Fig 4.14.

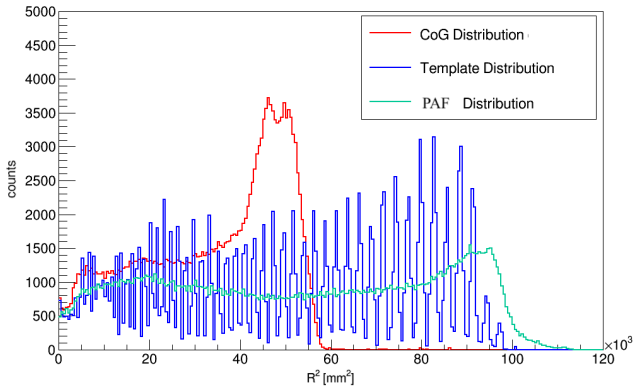

Figure 4.14: The comparison of the R^2 distribution of 164 keV events among the three algorithms.

^{127}Xe events with escaped γ

A lot of events from ^{127}Xe Electron Capture (EC) decay were observed in Run9 (with more details described below in Sec 4.6.3). The EC decay of ^{127}Xe is characterized by γs or conversion electrons and energy deposition of cascade X-rays or Auger electrons [104]. In the peripheral region of the TPC, the high energy γs can escape from the sensitive region and thus leaving the energy deposition of cascade X-rays or Auger electrons as the observable energy. The summation of cascade X-rays or Auger electrons is the binding energy of the captured electron of ^{127}Xe. Therefore, the distribution of these low energy events with escaped γ is simulated in MC as a reference. In PandaX-II, we used K-shell events with 33.2 keV to compare PAF and Template algorithms as shown in Fig 4.15. We select the bulk part in the Z-direction, i.e., with drift time from 36 to 318 μs, to avoid the backgrounds from PMT arrays in the energy selection window.

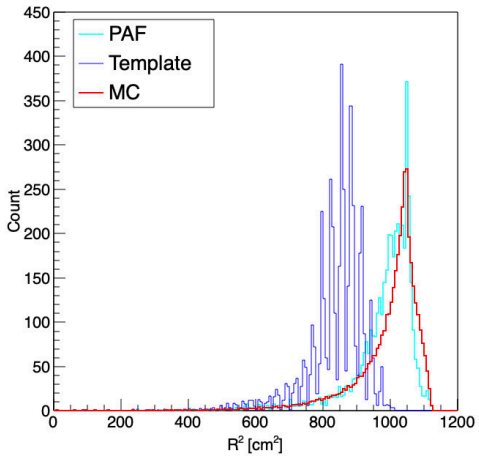

Figure 4.15: The R^2 distribution of 33.2 keV events from ^{127}Xe reconstructed by PAF (cyan) and Template (blue). The R^2 distributions of two sets of events from MC are overlaid as red histograms for comparison.

PAF yielded a similar R^2 distribution of 33.2 events from ^{127}Xe decay with MC compared to Template. PAF extended the distribution of the events to the real boundary of the sensitive volume and thus enlarged the final fiducial volume in later analysis.

Run8 treatment

We had two PMTs misbehaved in Run8. The PAF of each PMT should only depend on the geometry around the PMT and its quantum efficiency. Thus, the PAF obtained from Run9 should be able to apply to data in Run8 directly. We ignore the contribution from those two PMTs in Eq 4.11:

$$-\ln \tilde{L}(\vec{r}) = -\sum_{\substack{i \\ i\neq 71,102}} \frac{n_i}{\mathrm{qS2T}} \ln \frac{\eta_i(\vec{r})}{P(\vec{r})} \tag{4.14}$$

We applied PAF backward to Run8 data and investigated the gate events distribution. Fig 4.16 shows the X-Y distribution of the gate events with drift time in (1.8, 3.2) μs.

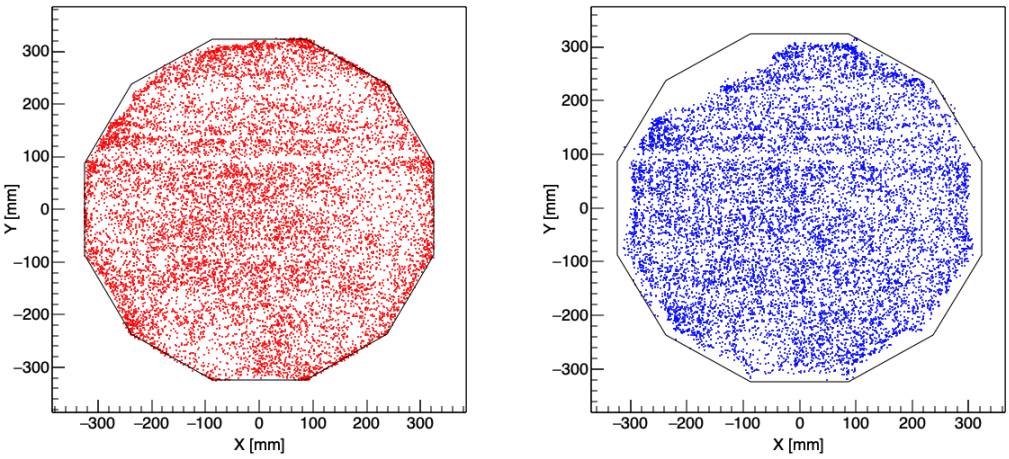

Figure 4.16: The gate events distribution reconstructed by PAF (red) and Template (blue).

The defected position distribution of gate events due to two inhibited PMTs was fixed in PAF rather than Template. We can observe the wires of the gate electrode in the X-direction.

Wall event distribution

The α emitted from ^{210}Po particle deposits its energy in liquid xenon in a track of the sub-millimeter level. This feature can be used to study the performance of the PAF algorithm in the edgy region of the TPC. On the other hand, the horizontal component of the drift field may push the electron cluster inward [105]. We selected the α events from the ^{210}Po decay using their lower $S2$ to $S1$ ratio and energy compared to the bulk α events (see in Fig 4.39) and studied the field distortion. Fig 4.17 shows the azimuthal distribution of ^{210}Po α events using three algorithms for position reconstruction. All three algorithms have consistent azimuthal distributions.

We looked into the radial distribution to the depth of these α events on each

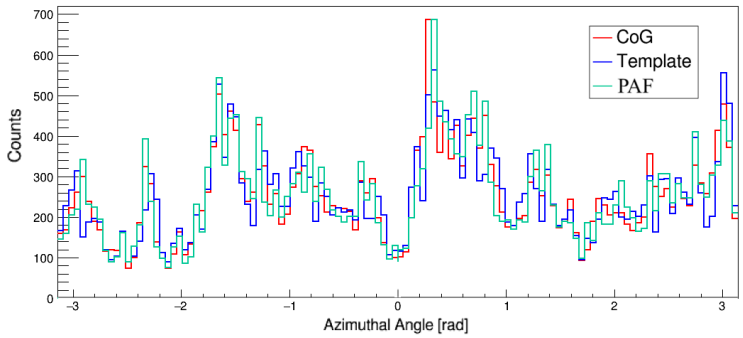

Figure 4.17: The azimuthal distribution of ^{210}Po α events using different reconstruction algorithms.

one of the 12 PTFE reflection panels as shown in Fig 4.18.

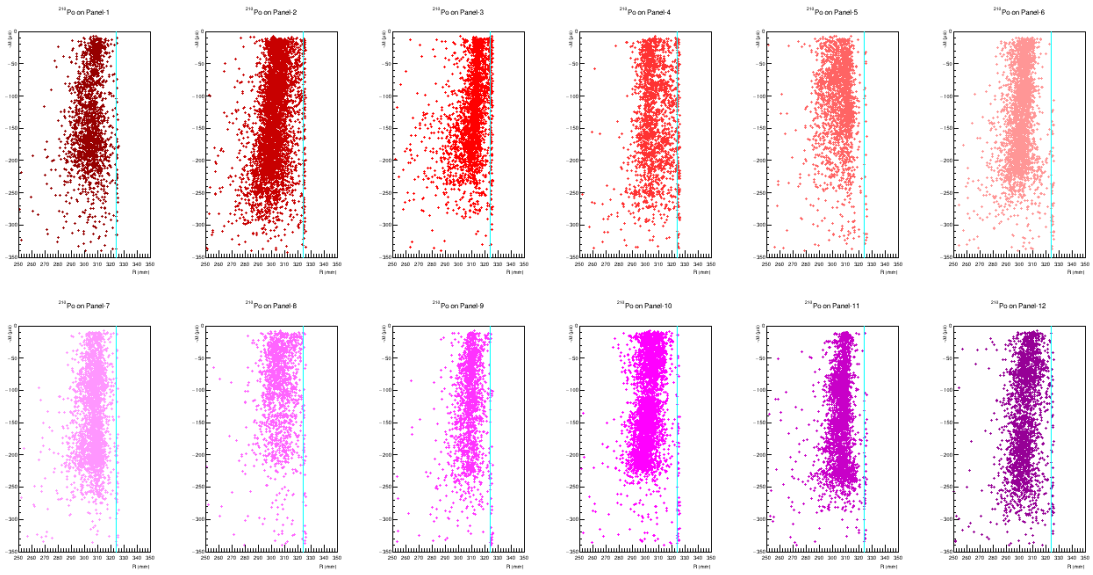

Figure 4.18: The radial distance of the α events from the ^{210}Po plate-out in each PTFE panel. The solid cyan lines indicate the position of the PTFE wall at R = 324 mm.

By averaging the radial distribution of the α events of 12 panels, we observed a total radial distribution indicating the field distortion. Following the same procedure, the field distortion was slightly worse in Run10. Both the overall radial distribution of Run9 and Run10 are shown in Fig 4.19.

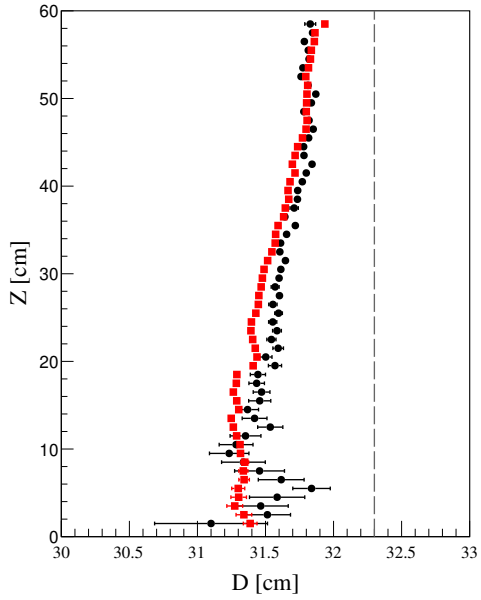

Figure 4.19: The distribution of the distance to PTFE panels of plated-out ^{210}Po α events in Run9 (black circle) and Run10 (red square). The dashed gray line indicates the PTFE panels located at $D = 32.4$ cm. A small slant of the "wall" was observed, indicating the magnitude of the field distortion.

4.4 Uniformity correction

Uniformly distributed mono-energetic events were used to produce a uniformity correction for the $S1$ and $S2$ signals. In this section, I will describe the algorithm for the uniformity correction. A three-dimensional correction map was produced for $S1$. For the $S2$ signals, the vertical uniformity correction was obtained by fitting $S2$ dependence on the drift time using the electron lifetime as an exponential decay constant τ. The $S2$ distribution in the horizontal plane was used to produce a two-dimensional correction map the in X-Y plane.

In Run8, we used the 164 keV γs from the decay of ^{131m}Xe (with 11.84-day half-life time) which was produced by inelastic neutron scattering during the calibration

runs. In Run9, we had large statistics of the 164 keV γs due to the cosmogenic activation during the transportation between CJPL and Shanghai for the distillation campaign. In Run10, we used the 236 keV γs from the ^{129m}Xe (with 8.88-day half-life time) instead for larger statistics.

Fig 4.20 shows the Light Yield (LY) and Charge Yield (CY) mapping in Run9 and Run10. There is negligible dependence on the γ energy of the mappings in the fiducial volume. A hot spot can be observed in CY mapping indicating the larger amplification in the center of the TPC which possibly due to the deformation of the anode or the gate electrodes.

4.4.1 $S2$ correction

The electron attenuation length in Run9 and Run10 is shown in Fig 2.16. We usually applied a preliminary correction to the events with $S1 < 1,000$ PE and $S2 < 100,000$ PE. Polynomials are used to fit the dependence of $S1$ and the $S2$ profile on R and S1 profile on Z. An exponential was used for fitting the Z dependence of $S2$ profile. After the preliminary correction, we selected the mono-energetic events of 164 or 236 keV as the samples. The Z dependence of $S2$ of sample events was fitted by an exponential again which provided the electron lifetime, or the electron attenuation length as shown in Fig 4.21.

We corrected the $S2$ in Z according to their electron lifetime derived in each run period.

The X-Y plane was then partitioned into blocks as shown in Fig 4.22. In each

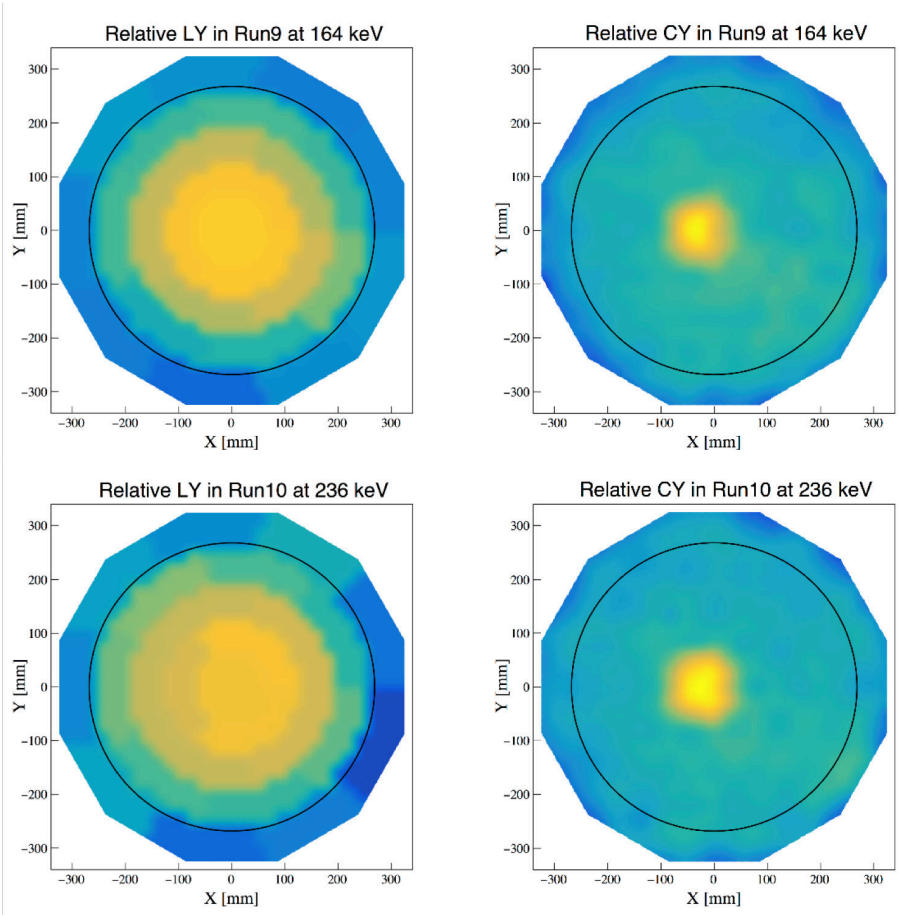

Figure 4.20: Relative LY (left) and CY (right) mappings in Run9 using 164 keV events (top) and in Run10 using 236 keV (bottom). The color representation was logarithmic. The left plots are projections of three-dimensional LY mappings in the X-Y plane. The solid black lines indicate the fiducial volume ($R^2 < 72000$ mm^2) region in both mappings.

block, the Z-corrected S2 spectrum was fitted by a Gaussian to get the mean. A two-dimensional histogram with 25 bins in both X and Y from -340 to 340 mm was filled using the mean values in blocks. The histogram was smoothed six times which gave the final CY correction mapping as shown in Fig 4.20.

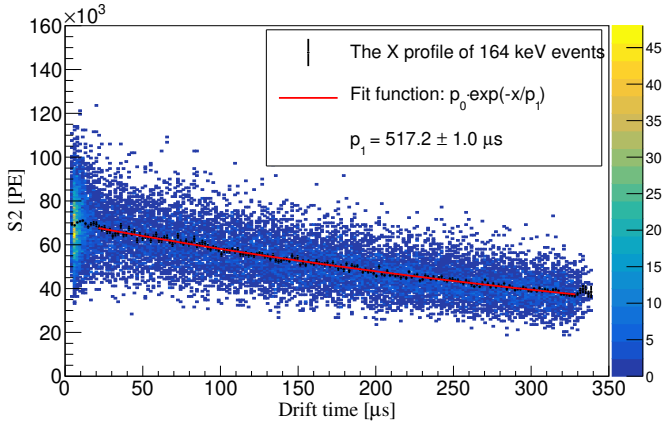

Figure 4.21: An example of the exponential fitting of an electron lifetime in Run9.

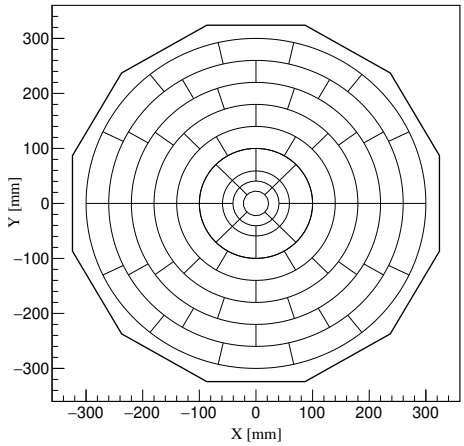

Figure 4.22: The partition in the X-Y plane for the $S2$ correction. The blocks in the center are finer due to the hot spot.

4.4.2 $S1$ correction

In the LY mapping study, we used a three-dimensional partition of the entire sensitive volume of TPC. The volume was divided into 6 slabs vertically and 25 blocks in each slab as shown in Fig 4.23.

A three-dimensional histogram was generated from -340 to 340 mm in X-Y and 0 to 360 μs for Z with 32 bins respectively. For each bin, the content was

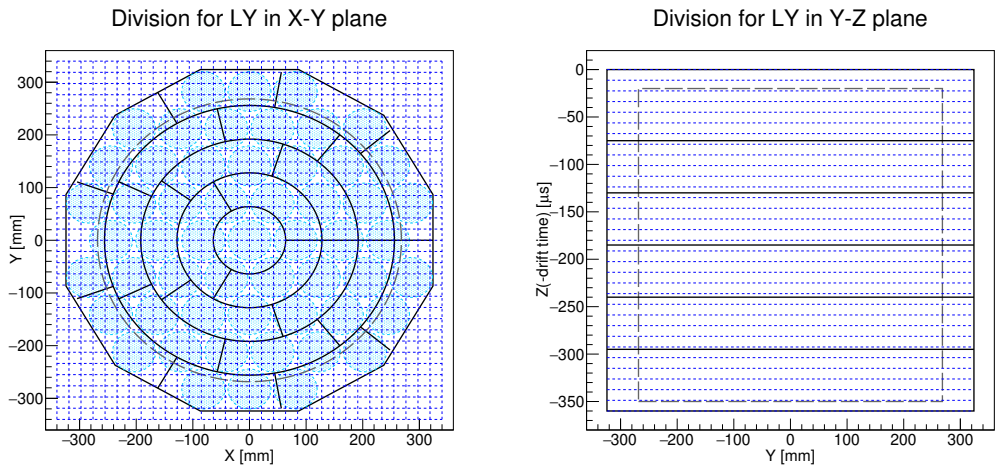

(a) (b)

Figure 4.23: The three-dimensional division of the active volume for $S1$ correction. The solid black lines in black define the partition, i.e., the boundaries of blocks or slabs. The gray dashed lines indicate the FV. The azure circles stand for PMTs. The blue dashed lines indicating bin division of the LY mapping.

assigned using the value of the block where the bin center located. The histogram was then refined four times into mapping with the same range but 512 bins in X, Y, and Z. The bin contents of those refined histograms were assigned using the predefined interpolation function of the "TH3" class in ROOT which produced the LY mappings as shown in Fig 4.20.

4.4.3 Improvement of $S1$ correction

The study of α events indicated that the mapping in Fig 4.20 was not smooth enough crossing the blocks. Fig 4.24(a) shows the dependence on Z of the original $S1$ signals from mostly α events before uniformity correction. A broad band can be observed, and the deeper $S1$s are larger. The $S1$ decreased for events with drift

time bigger than 250 μs due to the signal saturation in FADC and PMT. After the correction, the board band splits into three bands which are α events from ^{222}Rn, ^{218}Po/^{212}Bi/^{220}Rn, and ^{216}Po. The zigzag-shape indicates the non-smoothness of the LY correction map which leads to a reduced resolution on the alpha energy spectrum.

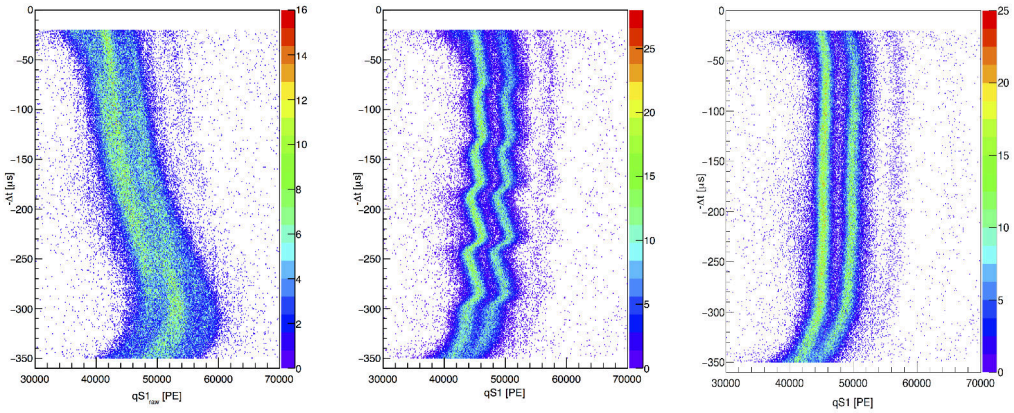

(a) (b) (c)

Figure 4.24: The vertical dependence of α bands before (a) and after (b) applying the original LY correction and the same bands using the improved LY mapping (c).

The interpolation process described above only smoothed the refined bins crossing the boundaries of blocks. The smooth transition only happened in a narrow range near the edges of blocks in Fig 4.25.

I improved the smooth procedure by introducing the Fourier series to calculate for $LY(\phi)$ in each ring of each slab. And then I calculated the LY by linear interpolation in R and Z respectively as shown in Fig 4.26.

The Fourier series is calculated to the 4th order for LY in each R ring (R_i) in

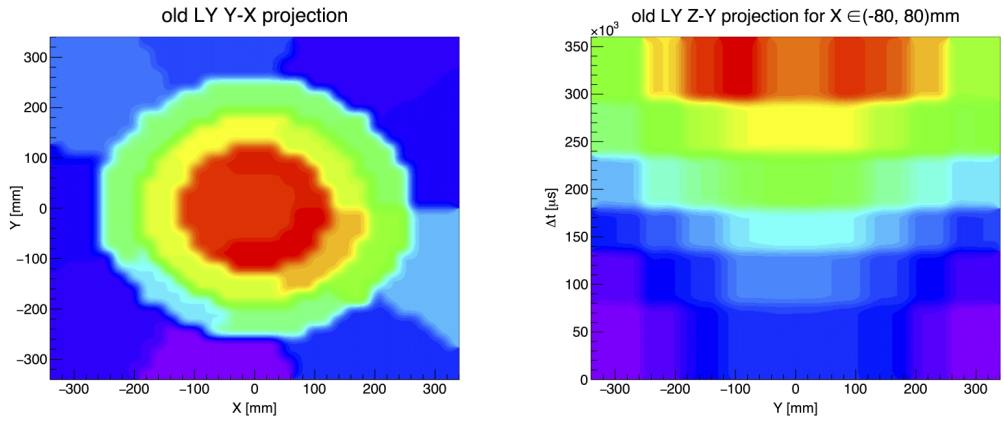

(a) (b)

Figure 4.25: The X-Y projection of the old LY mapping (a) and Z-Y projection for events with $-80 < x < 80$ mm (b).

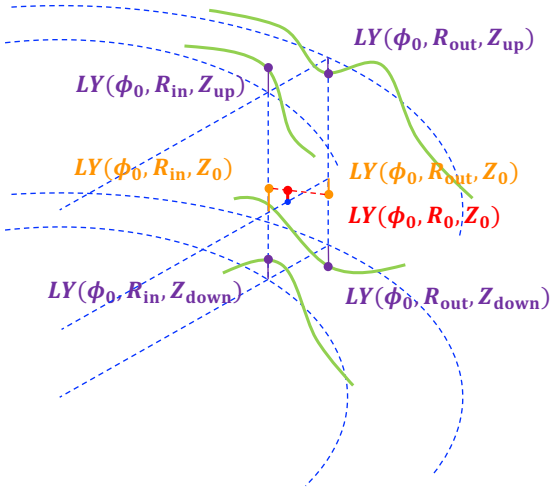

Figure 4.26: A schematic diagram of linear interpolation in R and Z. The LY at the red point is derived by a linear interpolation of the LY at two orange points which each is linear-interpolated from the LY at two yellow points above and below it.

each Z_j slab, i.e.,

$$LY^{R_i,Z_j}(\phi) = \frac{a_0^{R_i,Z_j}}{2} + \sum_{n=1}^{4}[a_n^{R_i,Z_j}\cos(n\phi) + b_n^{R_i,Z_j}\sin(n\phi)], \tag{4.15}$$

where

$$\begin{cases} a_n^{R_i,Z_j} &= \frac{1}{\pi}\int_{-\pi}^{\pi} f^{R_i,Z_j}(x)\cos(nx)\mathrm{d}x \\ b_n^{R_i,Z_j} &= \frac{1}{\pi}\int_{-\pi}^{\pi} f^{R_i,Z_j}(x)\sin(nx)\mathrm{d}x \end{cases} \tag{4.16}$$

for $n = 0$, 1, 2, 3, and 4. $f^{R_i,Z_j}(x)$ is the piece-wise function of the values of blocks. Fig 4.27 shows the Fourier series of outer four rings in the top and bottom slabs. Histograms represent $f^{R_i,Z_j}(x)$ in rings and the red lines are their Fourier series.

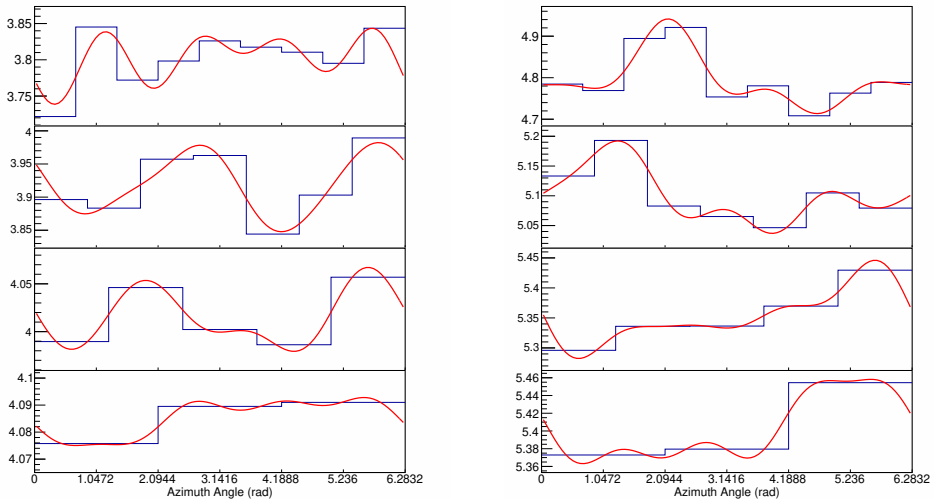

(a) (b)

Figure 4.27: The Fourier series of outer four rings in the top (a) and bottom (b) slabs.

After interpolation in R and Z, LY mapping is given in Fig 4.28, and the α bands are shown in Fig 4.24(c). Compared to Fig 4.25, improved LY mapping has much smoother transitions between blocks.

The new LY correction mapping improved the energy resolution for α peaks by 24 and 29% for ^{222}Rn and ^{218}Po respectively as shown in Fig 4.29.

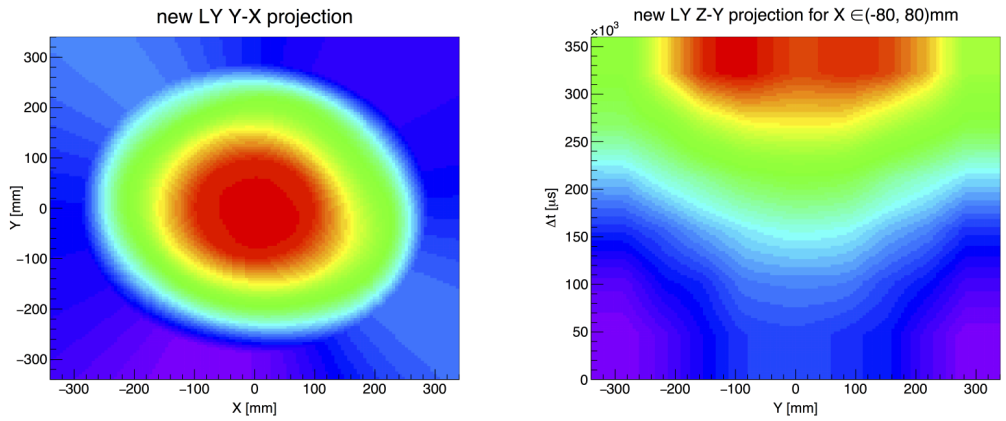

(a) (b)

Figure 4.28: The X-Y projection (a) and Z-Y projection for events with $-80 < x < 80$ mm (b) of the improved LY mapping.

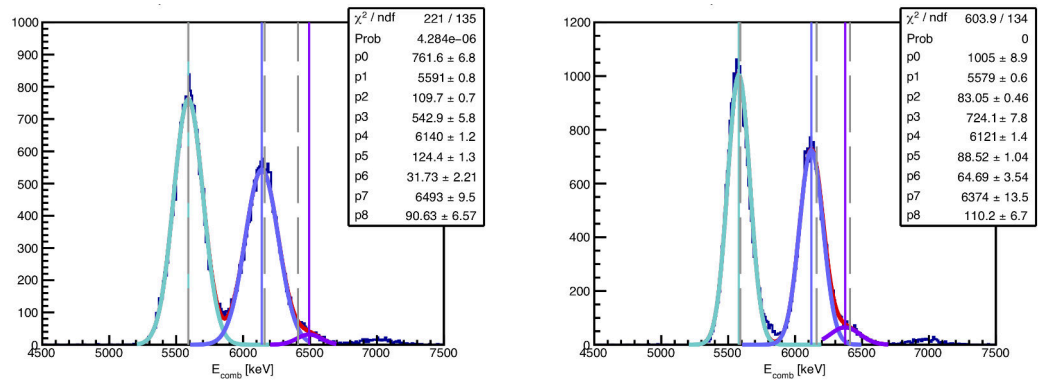

(a) (b)

Figure 4.29: The α peaks within the fiducial volume using old (a) and improved (b) LY corrections. The blue histogram is data. The red curve is fitting using three Gaussians. Individual Gaussians are given in cyan, blue and violet representing α events from ^{222}Rn, ^{218}Po/^{212}Bi, and ^{220}Rn.

4.5 Energy reconstruction

The deposited energy of every event can be reconstructed using the combined energy formula

$$E_{ee} = W \cdot (\frac{S1}{\text{PDE}} + \frac{S2}{\text{SEG} \cdot \text{EEE}}), \tag{4.17}$$

where W is 13.7 eV as the work function standing for the average energy needed to produce a quantum of a xenon scintillation photon or an escaped electron. PDE is the detection efficiency of the photons of $S1$s. EEE represents the extraction efficiency of the escaped electrons in the gas-liquid interface. And SEG stands for the average amplification of a single electron in the gas gap via electroluminescence after extraction.

In the PandaX-II data analysis, SEG was determined by fitting the spectrum of the small $S2$ signals. Random small $S2$s were selected with requirements on time, width, number of active PMTs and top-bottom ratio. The spectrum of small $S2$s

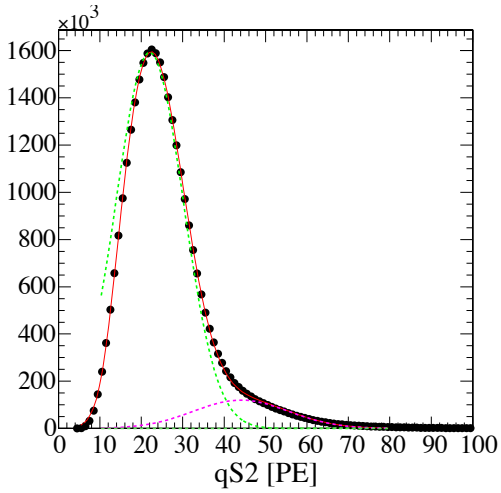

Figure 4.30: The fitting (solid red curve) of the spectrum of small $S2$s (black histogram) by a Fermi-Dirac function and two Gaussians. Green dashed curve is the single-electron Gaussian, and the magenta one is the double-electron Gaussian.

was fitted with double Gaussian or a Fermi-Dirac with double Gaussians as shown in Fig 4.30. The Fermi-Dirac represents the inefficiency araising from selection criteria or a pulse identification algorithm. The gap window of clustering hits among all PMTs was varied to derive the systematic error on the SEG. The fitted SEG value is 22.3 $\pm$ 0.5 PE/e$^-$ with time variation during Run10 taking into account. The final SEG value is 23.9 $\pm$ 0.5 PE/e$^-$ taking the ZLE efficiency into account.

We used χ^2-fit to minimize the residual between the fitted and true energies of various peaks.

$$\chi^2 = \sum_{i=1} \frac{(\mu_i - E_i)^2}{\delta^2_{\mu_i}} \tag{4.18}$$

where i rolls over various peaks, and μ_i is the combined energy of the i^{th} peak and E_i is the true energy from the database. δ_{μ_i} is the uncertainty of the i^{th} peak.

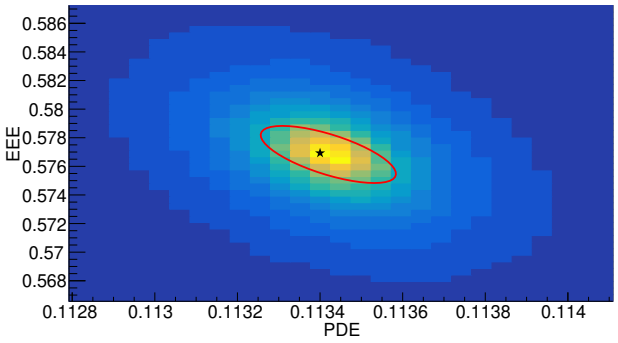

Figure 4.31: The PDE and EEE combined scan with $1/\chi^2$ as the weight. The black stars represent the best fits, and the red ellipse correspond to the 1σ contours used to determine the uncertainties.

The 40 and 80 keV were not taken for χ^2 calculation due to the ZLE bias in Run10. Instead, 408.2 keV from ^{127}Xe and 5.91 MeV α from ^{222}Rn were used for χ^2 minimization. The minimum χ^2 reached 2.7938 at 0.1134 as PDE and 0.5769 as EEE. The final PDE and EEE in Run10 are 0.1134 ± 0.0046 and 0.5769 ± 0.0187,

respectively.

The fittings of various peaks are shown in Fig 4.32. The energy reconstruction was using Eq. 4.17 for the low energy part in DM data, namely 164 keV peak from ^{131}Xe, 202.8 keV peak from ^{127}Xe associating with observable binding energies of different shells. The 236 keV events from 202.8 keV γ accompanied with 33.2 keV K-shell binding energy of ^{127}I are partially affected by the saturation of PMTs. For higher energy ranges in DM, Co, and Cs runs, $S2_{\mathrm{Bottom}}$ was scaled by a constant factor as the total $S2$ in Eq. 4.17. The scaling factor from $S2_{\mathrm{Bottom}}$ to S2 was determined to be 3.465 using low energy events. The solid red curve in each pad in

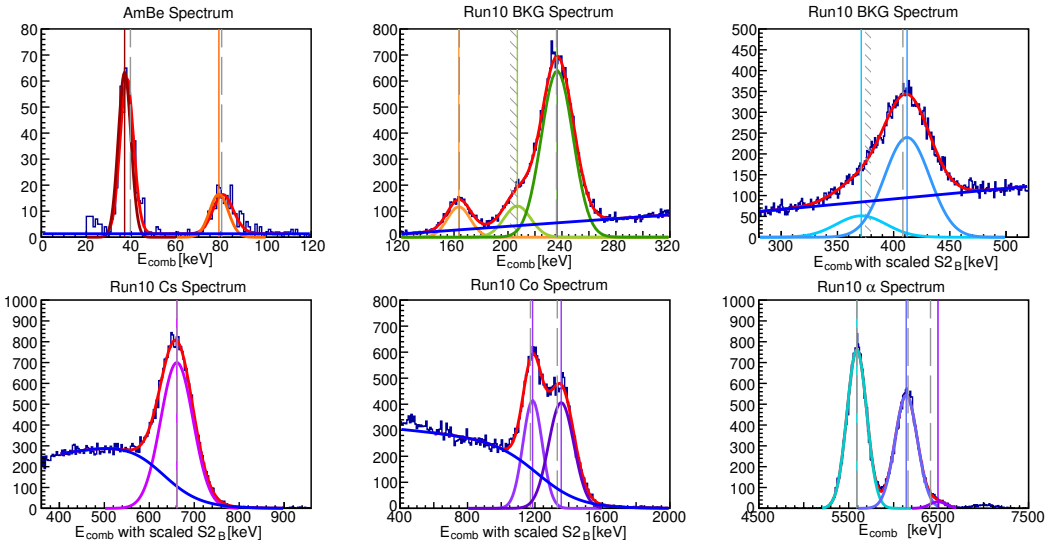

Figure 4.32: Energy reconstruction of mono-energy peaks in Run10. The top-left pad is the low energy spectrum of the AmBe run. The rest two top pads are the energy spectrum in the DM data. The bottom-left two pads are the energy spectrum in Cs and Co data. The bottom-right pad is the α spectrum in Run10. Except for the top-left two following the Eq. 4.17 as the energy scale, other spectrums in higher energy regions were using scaled $S2_{\mathrm{Bottom}}$ to avoid the saturation effect of $S2$s in the top PMTs. See text for details.

Fig 4.32 is the fitting curve with a background function and multiple Gaussians of the blue histogram. The gray dashed lines or shaded areas indicate the true energy

of peaks. The blue curves stand for background shape in those spectrums where are made of one order polynomial or an additional horizontally flipped Fermi-Dirac for the Compton plateau. The other colored curves are Gaussians indicating energy peaks and the vertical lines with the same color are showing the mean them. Note that in the top-left pad, the 40 and 80 keV are not pure ER events but mixed with 1.17 and 2.23 keVee respectively indicated from MC.

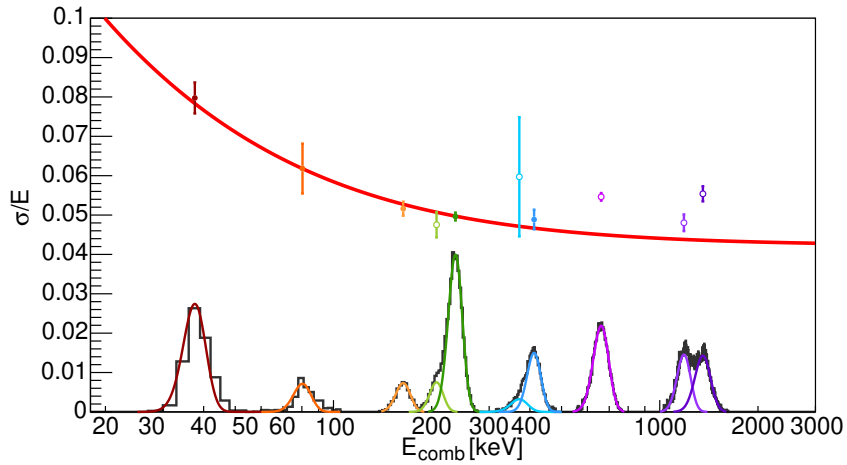

Figure 4.33: Energy resolution vs. E_{comb} in Run10 overlaid with the ER peaks in the data: 39.6 keV (n, ^{129}Xe*), 80.2 keV (n, ^{131}Xe*), 164 keV (^{131m}Xe), 236 keV (^{129m}Xe), 203, 375, and 408 keV (^{127}Xe), 662 keV (^{137}Cs), and 1173 and 1332 keV (^{60}Co). Spectra are scaled for visual clarity and fitted with multiple Gaussians. The data points represent the energy resolution corresponding to the fitted Gaussians with the same color. The solid red line represents the fit in the form of $\sigma/E = p_0/E + p_1$. Open circles are not included in the fit since they are not mono-energy peaks.

The energy resolutions of those energy peaks are shown in Fig 4.33. The energy resolution was also fitted by $\sqrt{p_0/E + p_1}$, and p_0 (p_1) is 0.088 ± 0.079 ($2.09 \pm 0.36 \times 10^{-3}$), i.e., the high energy resolution of the PandaX-II detector in Run10 reaches 4.57%.

4.6 Intrinsic background analysis

The background analysis is essential in rare event search experiments. Intrinsic ER backgrounds are from those radioactive sources uniformly distributed in the liquid xenon producing ER events. The discrimination power of low energy ER events from NR events, i.e., ER events with ($\log_{10}(S2/S1)$, $S1$) above the NR median, is about 99.6% in PandaX-II. In another word, 0.4% of ER events with downward fluctuated $S2/S1$ ratio could either be misidentified as the NR events from WIMPs or weaken the sensitivity. Krypton and radon and ^{127}Xe contributed to this type of background.

^{85}Kr β decays (half-life 10.72 y) into ^{85}Rb with a 99.563% probability of single β emission and 0.434% $\beta-\gamma$ delayed-coincident emission. The low energy portion of the β spectrum contributed to the ER background. In background analysis, the concentration of ^{85}Kr was estimated by identifying $\beta-\gamma$ delayed-coincident events. The Kr level was also crossed checked by offline gas sample measurement using the technique from [106].

The low energy events of β emitters in Rn progenies (mainly ^{214}Pb and ^{212}Pb) contribute to the ER background. The radon level in LXe can be evaluated by identifying $\beta-\alpha$ and $\alpha-\alpha$ coincidence events or fitting the α spectrum. ^{222}Rn was estimated by the ^{214}Bi-^{214}Po events. ^{220}Rn was determined by the ^{212}Bi-^{212}Po and ^{220}Rn-^{216}Po events. A depletion in the activities of progenies was found along both decay chains possibly due to the attachment of ions on the electrodes. Therefore, we used the result from $\beta-\alpha$ coincidence events as the activities of the β emitters

for the background analysis purpose.

^{127}Xe was produced by cosmic ray during the surface distillation campaign in early 2016. It decayed via electron capture (EC) to ^{127}I creating characteristic ER energy deposition in the detector. In the WIMP search region, M-shell and L-shell vacancies of ^{127}I can produce 1.1 keV and 5.2 keV ER events in the detector respectively and contribute to the background. The ^{127}Xe level was evaluated by the 33 keV K-shell events (following EC).

In this section, I will describe the analysis on the Kr level in Run8. The study on the Rn level in Run8 will be discussed as well. In the end, I will present the analysis of the ^{127}Xe level in Run9.

4.6.1 ^{85}Kr

An air leak likely introduced the krypton in xenon during the previous fill and recuperation cycle. ^{85}Kr is a β-emitter existing at an abundance of $\sim 2 \times 10^{-11}$ in the natural Kr in the atmosphere. The decay scheme of ^{85}Kr is shown in Fig 4.34 [107]. The β decay has a Q-value of 687.0 keV and a relatively long half-life

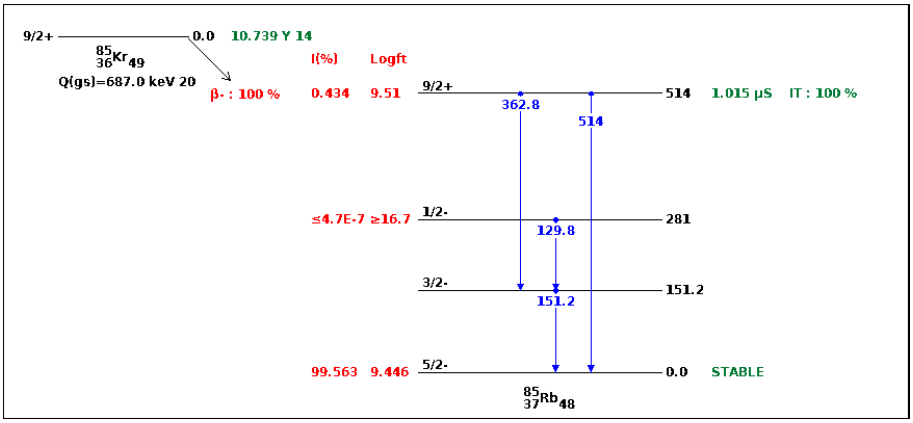

Figure 4.34: Decay scheme of ^{85}Kr Source: NNDC [107].

time of 10.756 y. The low energy portion of its continuous β spectrum contributes to the ER background in the WIMP search energy window. The most significant branch is to the ground state of ^{85}Rb (99.563%) emitting a single β and the second significant branch (0.434%) is to β-decay into ^{85m}Rb (end-point energy 173.4 keV) and subsequently de-excite into ^{85}Rb emitting a 514 keV γ with a half-life time of 1.015 μs. The second branch produces a β-γ coincidence signal and is used to calculate the krypton level in the data.

Data selection criteria (cuts) for β-γ events are summarized in Tab 4.2, including expected acceptance from MC.

Table 4.2: Selection cuts for ^{85}Kr candidate events. $tS1$ is the time of the $S1$ signal in our 1000 μs waveform window. The first two cuts require the timing of $S1$ in the trigger window.

Variable	Selection window	Acceptance
$tS1_\beta$	(480, 510) μs	
$tS1_\gamma$	(480, 520) μs	
β energy	(20, 200) keV	77.34%
γ energy	(314, 714) keV	94.3%
Delay Time between $S1$s	(0.3, 10) μs	92.18%
	Combined Cut	63.76%

Fig 4.35 shows a typical waveform of 85Kr β-γ coincidence event with delay time of 1.78 μs, $S1_\beta$ = 272.0 PE, $S1_\gamma$ = 1789.9 PE, $S2_\beta$ = 1.7×10^4 PE; and $S2_\gamma$ = 1.3×10^5 PE. In general, the $S2$(s) of the γ may overlap, above or behind the $S2$ of the β due to the penetration depth in a different direction and possible energy depositions in multiple sites. Therefore, the energy cuts in Tab 4.2 were applied on S1 only to avoid ambiguity on the reconstructed energy for γ multiple scattering

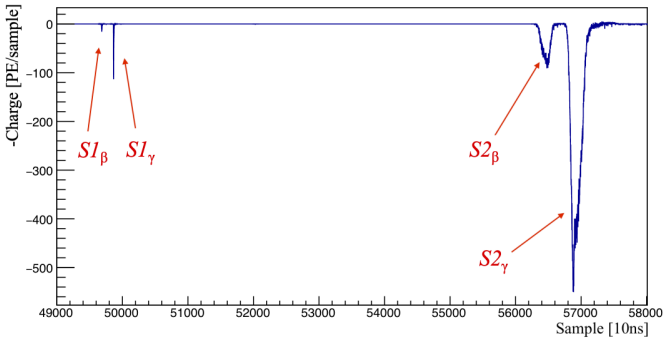

Figure 4.35: A typical waveform of ^{85}Kr β-γ coincidence events.

events. 184 out of the 203 events were found with at least one $S2$ ($>$ 800 PE) to reconstruct the horizontal position. The ratio is consistent with the ratio between the active volume and the reversed field region below the cathode. A top-bottom asymmetry (TBA), defined as

$$\mathrm{TBA} = \frac{S1_{\mathrm{top}} - S1_{\mathrm{bottom}}}{S1_{\mathrm{top}} + S1_{\mathrm{bottom}}}, \tag{4.19}$$

for the $S1$s is used to indicate the vertical distribution. From Fig 4.36(a) a good correlation between the βs and γs is shown. The drift time is defined using the time delay between the $S1_\gamma$ and the biggest $S2$. The drift time and the TBAs for these events are also in good agreement as in Fig 4.36(b). We use the drift time for the fiducial volume cut as $r^2 < 60000$ mm^2 and 20 μs $<$ drift time $<$ 346 μs.

Finally, 121 of 183 events are found in the 306 kg FV, as illustrated in Fig 4.37.

The mole fraction of krypton in xenon is calculated as

$$\frac{[\mathrm{Kr}]}{[\mathrm{Xe}]} = \frac{N_{\beta-\gamma} \cdot \frac{\tau}{T}}{I_{\beta-\gamma} \cdot A_{\mathrm{comb}} \cdot \frac{[^{85}\mathrm{Kr}]}{[\mathrm{Kr}]} \cdot \frac{m_{\mathrm{Xe}}}{M_{\mathrm{Xe}}} \cdot \mathcal{N}_A} \tag{4.20}$$

where [Kr]/[Xe] is the Kr concentration in Xe in mol/mol. $N_{\beta-\gamma}$ is 121 after the fiducial volume (FV) cut. T is 417.24 h for the analysis data in Run8 and τ is

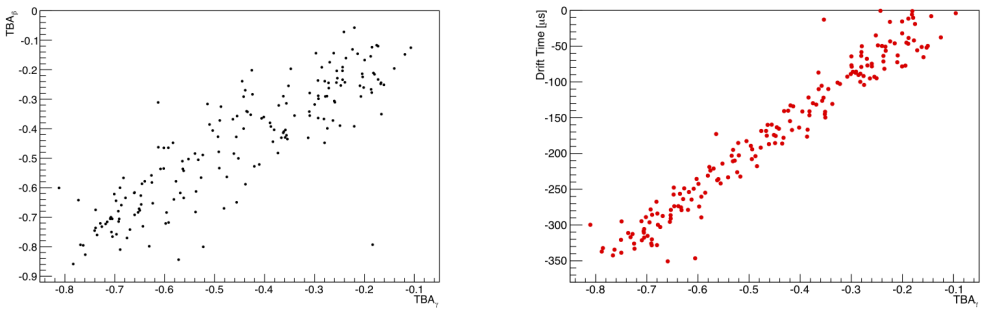

(a) (b)

Figure 4.36: The correlation between TBA, $(S1_{\text{top}}\text{-}S1_{\text{bottom}})/S1$, of βs and γs (a) and the correlation between drift time and TBA_γ (b) of 184 coincidence events.

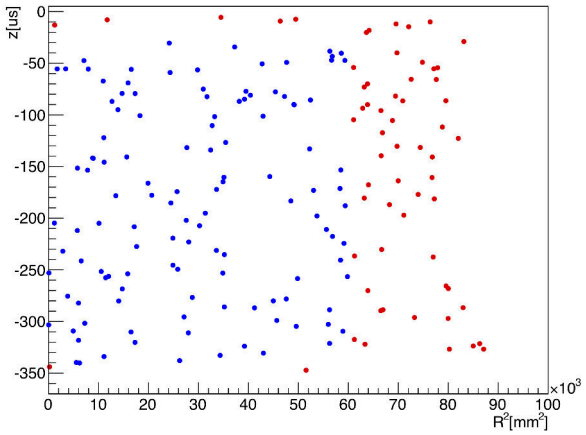

Figure 4.37: The vertex distribution of ^{85}Kr β-γ coincidence events. Events in blue (red) are in (out of) the FV.

215.479 y calculated from the decay half-life time and ln2. $I_{\beta-\gamma}$ is the branching ratio of β-γ coincidence as 0.434%. A_{comb} is the combined acceptance of cuts as 63.76%. $[^{85}\text{Kr}]/[\text{Kr}]$ is taken to be 2×10^{-11} as ^{85}Kr in nature Kr. m_{Xe} is 306 kg, and M_{Xe} is 131.293 g/mol. $\mathcal{N}_A$ is the Avogadro number. This calculation leads to a Kr mole fraction of 507 ± 46 parts per trillion (ppt).

4.6.2 Rn and its progenies

^{238}U and ^{232}Th decay chains are shown in Fig 4.38. When they decay into ^{222}Rn and ^{220}Rn, Rn can emanate from the surface of the detector materials and mix with LXe. The Rn progenies with β decays contribute to the ER background.

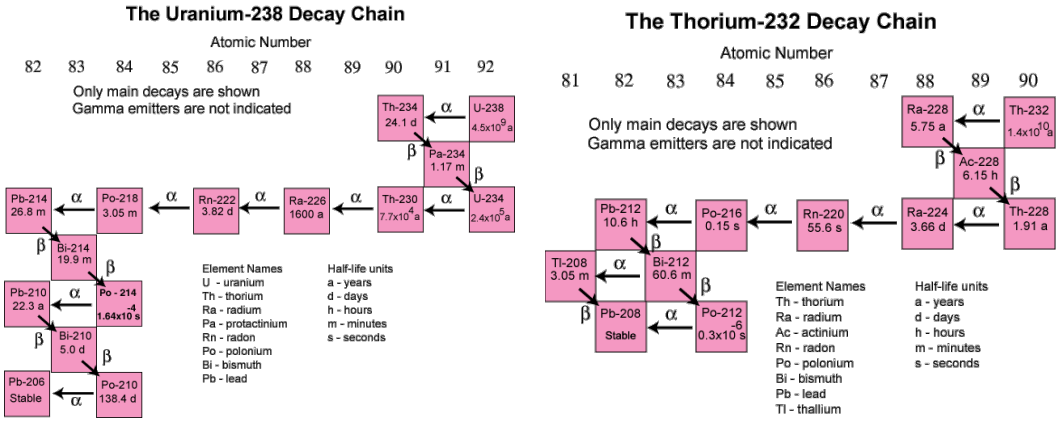

(a) (b)

Figure 4.38: The decay chains of ^{238}U and ^{232}Th. Source: U.S. Geological Survey (USGS).

For all single scatter events in parameter space ($\log_{10}(S2/S1)$, $S1$) in the dark matter search data (Fig 4.39), different clusters of α events can be identified for large $S1$ and small $S2/S1$. For background analysis, we only use bulk α events.

The radon levels are determined from the data using the following methods. For the ^{222}Rn level, β-α coincidence events from ^{214}Bi-^{214}Po are identified. For the ^{220}Rn level, we use β-α coincidence events from ^{212}Bi-^{212}Po. Besides, α-α coincidence events from ^{220}Rn-^{216}Po can also be identified. Moreover, the radon in LXe can be detected making use of characteristic αs in the decay chain. Pulse shape cuts were developed for $S1$s from α. A single-α analysis was performed by fitting the α

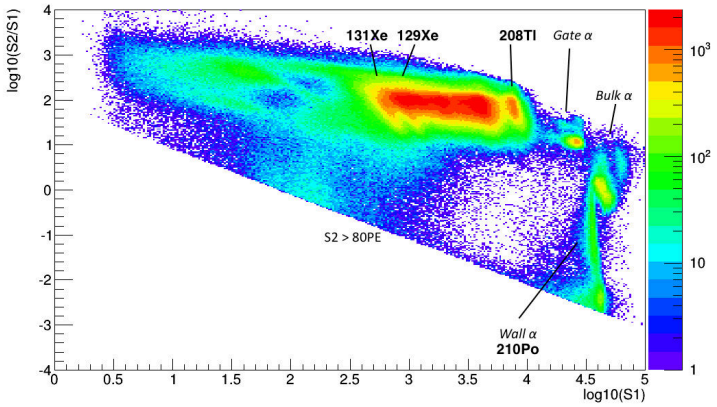

Figure 4.39: $\log_{10}(S2_{\mathrm{raw}}/S1_{\mathrm{raw}})$ vs. $S1_{\mathrm{raw}}$ for all single-scatter events from the dark matter search data, with α clusters indicated. Subscript "raw" on $S1$ and $S2$ indicates the signal before uniformity correction.

spectrum to calculate the rate of Rn isotopes and their progenies.

^{214}Bi-^{214}Po coincidence events

After emitting a β with a maximum energy of 3.272 MeV, ^{214}Bi decays into ^{214}Po which has 164.3 μs half-life time proceeding to an α decay with a Q-Value 7.84 MeV. Within our 1 ms data taking window, a typical waveform is shown in Fig 4.40.

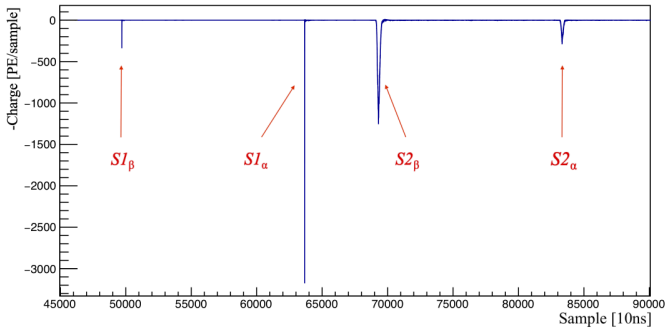

Figure 4.40: A typical waveform of a ^{214}Bi-^{214}Po β-α coincidence event.

We applied the cuts listed in Tab 4.3 to select the coincidence events. According to the MC simulation, the acceptance of the combined cuts is 86.14%. After

Table 4.3: Selection cuts for ^{214}Bi-^{214}Po β-α candidate events

Variable	Selection window	Acceptance
β-α delay time	(3, 500) μs	86.60%
β energy	(50, 4000) keV	97.92%
α energy	>3 MeV	98.43%
	Combined Cut	86.14%

the coincidence and energy cuts, 5934 events were selected. More cuts were applied to the candidates to remove the random coincidence events and considered without inefficiency. Firstly, a cut was developed on the TBA_β vs. TBA_α to ensure β and α are close vertically as in Fig 4.41(a). The cluster towards the bottom is due to the saturation of $S1$ in the bottom PMTs when α is too close to the cathode.

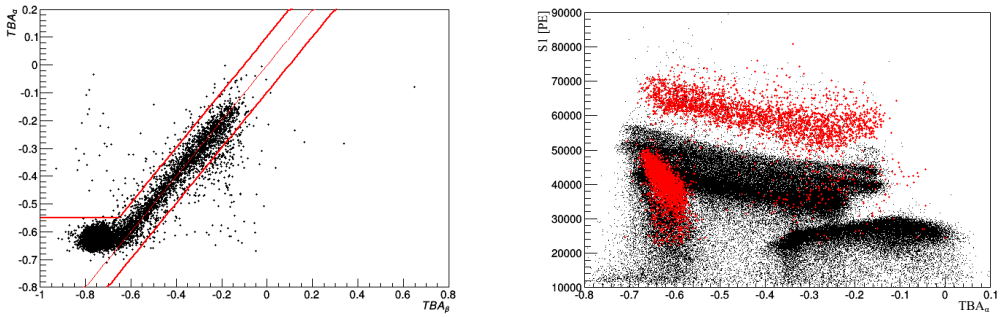

(a) (b)

Figure 4.41: TBA_α vs. TBA_β cut (red lines) on the ^{214}Bi-^{214}Po β-α coincidence candidates (a). Raw $S1$ signal versus TBA of α events (b).

α events closed to the cathode wires also suffer from severe field non-uniformity and optical shadowing effects. As illustrated in Fig 4.41(b) that there is a separate cluster with suppressed $S1$ closed to the cathode. The black spots are all α events passing the pulse shape cuts. The red spots are the 7.81 MeV α from ^{214}Po events

identified from the coincidence analysis.

The delay time distribution of the coincidence events is fitted to be 231.1 ± 6.9 μs, which is in good agreement with $\tau_{1/2} = 164.3$ μs, i.e., $\tau = 237.0$ μs as shown in Fig 4.42.

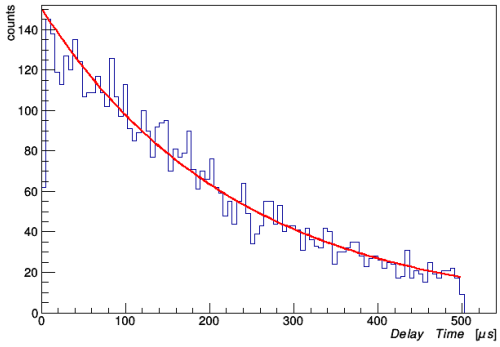

Figure 4.42: The exponential fitting of the distribution of the delay time between the $S1$s of β-α.

Second, to avoid the largest $S2$ being incorrectly associated with β, we also required that the drift time (depth) of the identified β be consistent with its TBA, illustrated in Fig 4.43(a)). Finally, the FV cut is applied to the β events, as shown in Fig 4.43(b).

The energy spectra for the β and α in FV are shown in Fig 4.44. The energy of β was reconstructed by the combined energy formula, and the α energy was restored from $S1$-only to avoid ambiguity due to mispairing of $S2$.

The double peak structure in the α energy spectrum was again due to those close-to-cathode events that cannot be removed by the loose FV cut. We didn't remove them for a more conservative calculation.

The selected events after each sequential cut are summarized in Tab 4.4. The

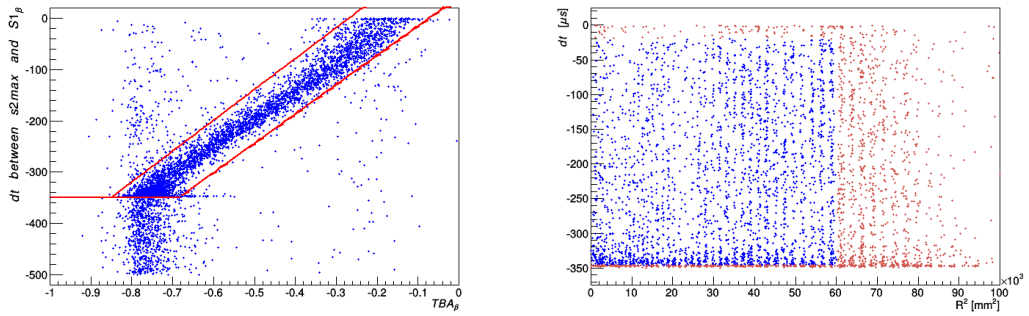

(a) (b)

Figure 4.43: Delay time between the largest $S2$ and $S1_\beta$ vs. TBA_β (a) and the vertex distribution of β events inside (blue) and outside (red) the FV (b). The red lines indicate the depth-TBA cuts.

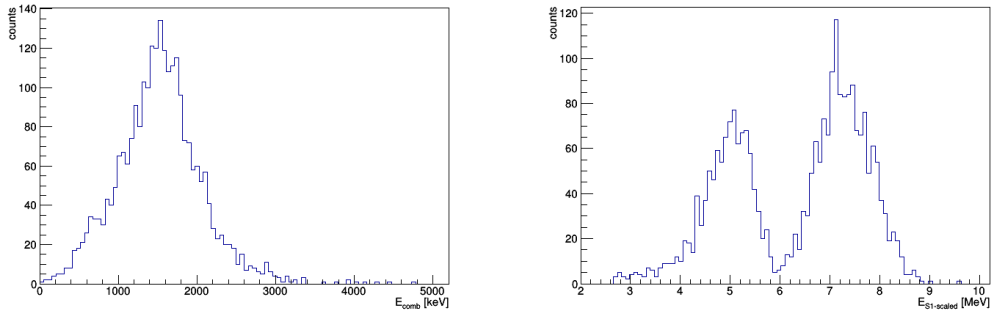

(a) β energy (b) α energy

Figure 4.44: The energy spectrum of β (a) and α (b) events in the FV.

Table 4.4: ^{214}Bi-^{214}Po β-α events surviving sequential high-level cuts.

Cuts	Number of events left
coincidence and energy	5934
TBA β-α	5593
depth-TBA_β	4325
FV	2595

activity of ^{222}Rn from ^{214}Bi-^{214}Po coincidence analysis was 2.01 mBq, i.e.,

$$2595 \div 86.14\% \div 99.98\% \div (417.25 \text{ h}) = 2.01 \text{ mBq}, \tag{4.21}$$

in which 99.98% is the branching ratio from ^{214}Bi to ^{214}Po. The ^{222}Rn level in 306 kg FV is 6.57 μBq/kg.

^{212}Bi-^{212}Po coincidence events

Similar to the analysis of ^{214}Bi-^{214}Po coincidence events, the ^{212}Bi via a β decay produces an α emitter ^{212}Po with a 0.3 μs half-life time. The endpoint of ^{212}Bi β is 2.25 MeV, and the Q-Value of the α particle from ^{212}Po is 8.78 MeV. The ^{212}Bi-^{212}Po β-α delayed coincidence signals can be used to derive the activity of ^{220}Rn in the LXe. A waveform of a typical ^{212}Bi-^{212}Po event is shown in Fig 4.45.

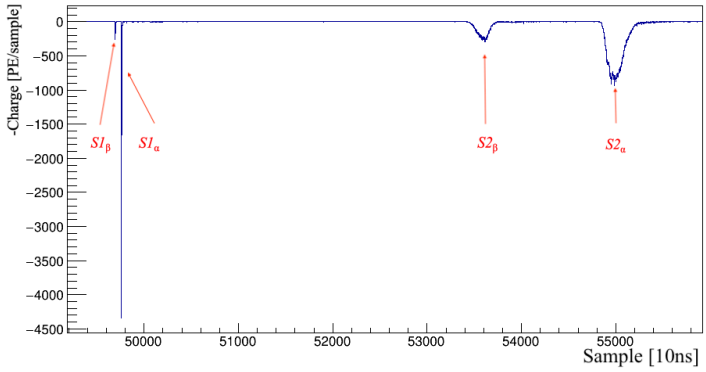

Figure 4.45: A typical waveform of a ^{212}Bi-^{212}Po β-α event.

The coincidence event selection cut based on the delay time and the energy of two signals summarized in Tab 4.5. There are 233 candidates after the coincidence

Table 4.5: Selection cuts for ^{212}Bi-^{212}Po β-α candidate events and their efficiencies from the MC

Variable	Selection window	Acceptance
β-α delay time	(0.3, 3) μs	49.82%
β energy	(50, 3000) keV	98.08%
α energy	>3 MeV	99.99%
	Combined Cut	48.85%

cuts with a good correlation of TBA between the α and β events. The exponential constant of the distribution of the delay time of two s1 signals was fitted to be 447.3±50.1 μs agrees the expected mean-life time of $\tau = \tau_{1/2}/\ln 2 = 432$ ns.

Similar to that in the ^{214}Bi-^{214}Po analysis, we applied depth-TBA cut by requiring consistency between the β drift time and its TBA. The FV cut is then used to select the final candidates, as shown in Fig 4.46.

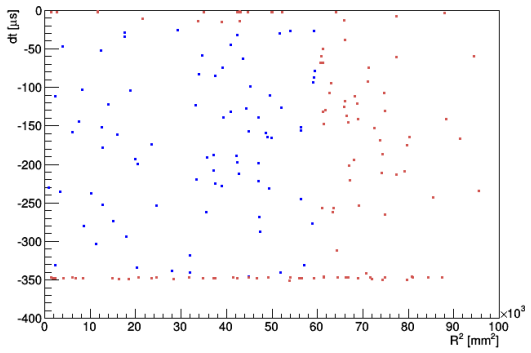

Figure 4.46: The vertex distribution of β events from ^{212}Bi-^{212}Po coincidence inside (blue) and outside (red) the FV.

The selected events after each sequential cut are summarized in Tab 4.6. The

Table 4.6: ^{212}Bi-^{212}Po β-α events surviving sequential high-level cuts.

Cuts	Number of events left
coincidence and energy	233
TBA β-α	233
depth-TBA$_\beta$	202
FV	78

final rate of the ^{220}Rn from the ^{212}Bi-^{212}Po coincidence analysis is 0.1655 mBq, i.e.,

$$78 \div 48.85\% \div 64.06\% \div (417.25 \text{ h}) = 0.1655 \text{ mBq}, \tag{4.22}$$

in which 64.06% is the branching ratio from ^{212}Bi to ^{212}Po.

^{220}Rn-^{216}Po coincidence events

^{220}Rn emit 6.41 MeV α and decay into ^{216}Po with 0.14 s half-life, which then α-decay into ^{212}Pb with Q-Value of 6.91 MeV. There are 3008 events found in total with the cuts defined in Tab 4.7. There are 1776 events after applying the depth-TBA cuts.

Table 4.7: Selection cuts for ^{220}Rn-^{216}Po α-α candidate events and their efficiencies from the MC.

Variable	Selection window	Acceptance
α-α delay time	(1 ms, file length)	99.52%
^{220}Rn α energy	(3.2, 10) MeV	99.91%
^{216}Po α energy	(3.6, 12) MeV	99.99%
	Combined Cut	99.42%

A 3.4 mm cut was applied to the vertical depth of the two αs, followed by a 100 mm cut on $|\,\Delta\vec{r}\,|$ in the X-Y plane. A charge ratio between the two $S1$s between 1.028 to 1.128 is applied.

The delay time distribution of the two α events is shown in Fig 4.47(a). The fitted decay time is significantly less than the expected value $\tau = \tau_{1/2}/\ln 2 = 0.202\ s$. The main reason for the discrepancy may be due to the low efficiency of finding correlated α events with long delay times. The FV cut is illustrated in Fig 4.47(b). The selected events after each sequential cut are summarized in Tab 4.8.

The rate of ^{220}Rn from ^{220}Rn-^{216}Po analysis is 0.126 mBq, i.e.,

$$188 \div 99.42\% \div (417.25\ \text{h}) = 0.126\ \text{mBq}. \tag{4.23}$$

single-α analysis

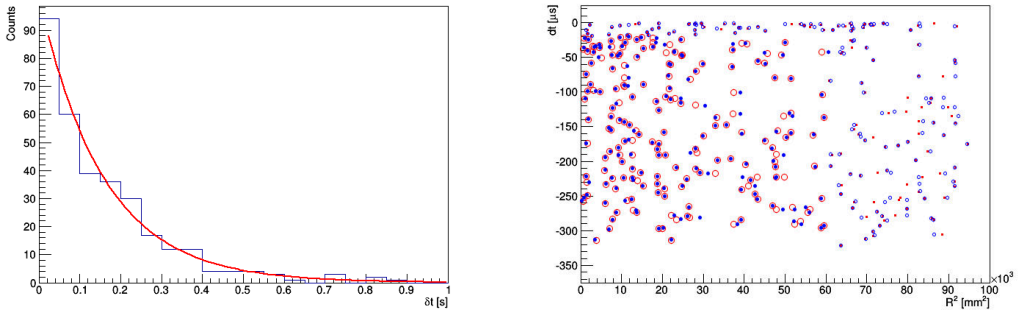

(a) (b)

Figure 4.47: The delay time distribution of the two α events (a). Vertex distribution of the ^{220}Rn-^{216}Po events (b). The blue points (red circles) refer to the first (second) α events in the FV and the red points (blue circles) show the first (second) α events outside the FV.

Table 4.8: ^{220}Rn-^{216}Po α-α events after sequential high-level cuts.

Cuts	Number of events left
coincidence and energy	3008
depth-TBA$_\beta$	1776
Δz	393
$\mid \Delta\vec{r} \mid$	329
$S1$ charge ratio	324
FV	188

Rn and some of its progenies are α emitters. Therefore, another way to estimate the Rn activity is to evaluate αs. We use $S1$ to scale the energy of αs, and the depth-TBA cut is applied to select α events with consistent drift time and TBA. After the FV cut, the spectrum of the final corrected energy is displayed in Fig 4.48. Multi-gaussian fitting was performed on the spectrum with centroids constrained to the expected energy of each type of α.

The integral of the Gaussian is used to estimate the rate, as summarized in Tab 4.9. For comparison, the Rn activities calculated from the delayed-coincidence

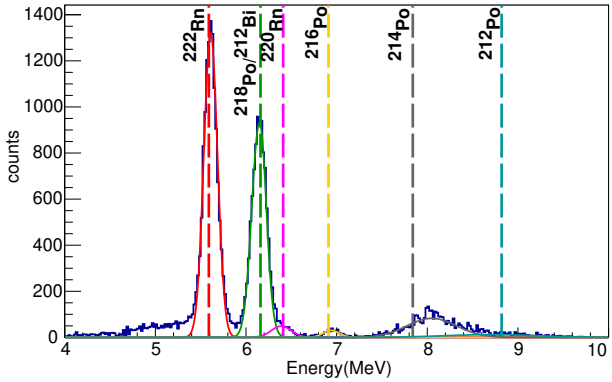

Figure 4.48: The energy spectrum of α events in the FV. Different colors indicate Multi Gaussians, and the dashed lines indicate the expected energy.

analysis are also listed in Tab 4.9.

Table 4.9: Rate of Rn decay in the FV estimated based on different decay chains. The ^{210}Po is not used to estimate the ^{222}Rn activity since it is out of secular equilibrium due to its long half-life time.

Chain	Isotope	Q-value (MeV)	fitted E (MeV)	activity (mBq)
U	^{222}Rn	5.59	5.60±0.09	6.507
	^{218}Po	6.16	6.11±0.11	4.673
	^{214}Bi-^{214}Po			2.01
	^{214}Po	7.84	7.97±0.26	1.476
Th	^{220}Rn	6.41	6.47±0.08	0.353
	^{220}Rn-^{216}Po			0.1655
	^{216}Po	6.91	6.89±0.14	0.175
	^{212}Bi	6.21	6.16±0.04	0.205
	^{212}Bi-^{212}Po			0.126
	^{212}Po	8.82	8.89±0.48	0.012

We observed a depletion along both decay chains. We note that the slow drift of charged ions towards the electrodes is a strong physical reason which leads to this depletion, as shown in [108]. Since in the dark matter region, the dominating β background is ^{214}Pb and ^{212}Pb, we chose the rates obtained from the nearby decay of ^{214}Bi-^{214}Po and ^{212}Bi-^{212}Po as the final Rn activities in the FV, 2.01 mBq of ^{222}Rn

and 0.166 mBq of ^{220}Rn in Run8.

4.6.3 ^{127}Xe

During the krypton distillation campaign in early 2016, 1.1 ton of xenon was exposed to about one month of sea level cosmic ray radiation. The neutron capture of ^{126}Xe produced ^{127}Xe, which then decayed via EC (ε-decay) to ^{127}I with a half-life time of 36.4 d. The EC created characteristic ER energy deposition in the detector as shown in Fig 4.49 from [104]. A ^{127}Xe nucleus captured an electron (a K-shell one in Fig 4.49) and converted into a ^{127}I in an excited state. The excited ^{127}I nucleus de-excited subsequently through the emission of one or more gamma rays or internal conversion electrons. The vacancy of the electron shell was filled by outer orbital electron and the ^{127}I atom emitted cascade x-rays or Auger electrons.

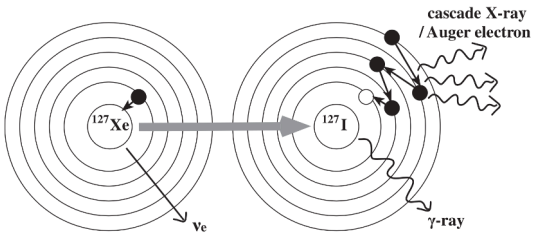

Figure 4.49: The schematic diagram of ^{127}Xe EC decay to ^{127}I [104].

The ^{127}Xe concentration was identified by the 33 keV K-shell x-ray (following EC), with a decay rate of about 1.1 ± 0.3 and 0.1 ± 0.03 mBq/kg at the beginning and end of Run9, respectively. As shown in Fig 4.50, the integrated event rate from 18 to 49 keVee was used to calculate the ^{127}Xe level. The red curve is the exponential fitting with half-life time 35.74 ± 0.03 d which consistent with the expected half-life

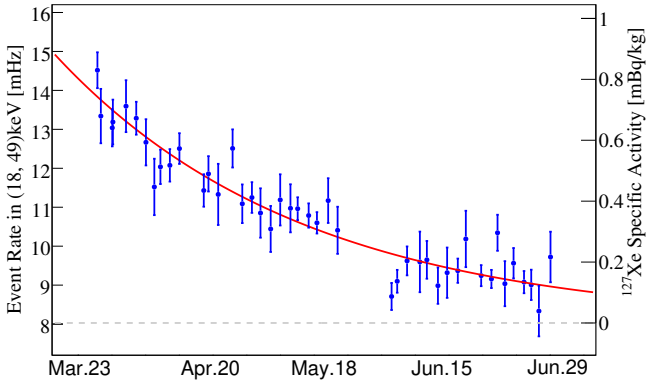

Figure 4.50: The evolution of the ^{127}Xe level during Run9.

time 36.4 d. The gray dashed line indicates the other background contribution in the same energy window.

In the low-energy region, M-shell and L-shell vacancies of ^{127}I can produce 1.1 keV and 5.2 keV ER events in the detector, respectively. The background was estimated to be 0.37 ± 0.05 mDRU below 10 keVee based on the MC calculations by scaling the measured K-shell x-ray rate, in good agreement with 0.42 ± 0.08 and 0.40 ± 0.13 mDRU obtained from the spectrum fit and time-dependence fit of the low energy events as shown in Fig 4.51.

4.6.4 Summary of intrinsic background

After Run8, we had a surface and an underground distillation campaign before Run9 and Run10 which lead to a Kr level of 44.5 ± 6.2 ppt and 6.6 ± 2.2 ppt, respectively. Following similar approaches with improvements, we carried out the analysis of the Rn levels in Run9 and Run10. We use the β-α coincidence events from ^{214}Bi-^{214}Po and ^{212}Bi-^{212}Po in U and Th chains as the estimator of Rn levels.

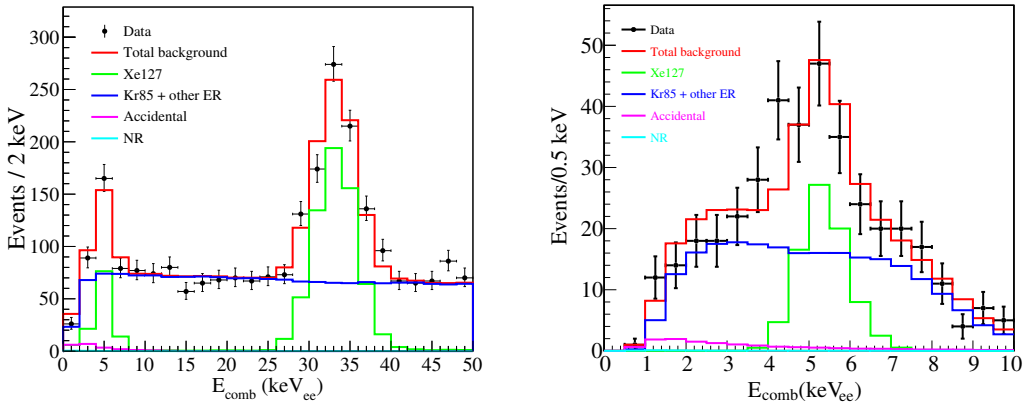

(a) (b)

Figure 4.51: Combined energy spectrum from 0 to 50 keV (a) and 0 to 10 keV with DM search window cuts on $S1$ and $S2$ (b) in Run9.

The specific Rn levels are derived by scaling the xenon mass of the FV in each run set. ^{127}Xe was generated after Run8 and less than a quarter fresh xenon was introduced in Run10. The contribution of Kr, Rn, and ^{127}Xe in Run8, 9, and 10 are summarized in Tab 4.10.

Table 4.10: The contribution to low energy ER background from Kr, Rn, and ^{127}Xe in Run8, 9, and 10 in mDRU.

Source	Run8	Run9	Run10
^{85}Kr	11.7	1.19	0.73
^{222}Rn	0.06	0.13	0.12
^{220}Rn	0.02	0.01	0.02
^{127}Xe	0	0.42	0.02

All these levels are used as inputs of background in the profile likelihood function for the limit calculation.

4.7 Limit calculation for WIMP-nucleon SI interactions

In general, DM direct search experiments present the upper limit on the parameter space of the interaction cross section and the mass of the WIMP particle. In this section, I will outline the method of limit calculation in PandaX-II. With certain exposure of the data, we calculate the acceptance function to the nuclear recoil energy and the hypothetical DM event rate at any given mass. The acceptance curve can be converted to the DM mass using the NR model. The combination of the exposure, acceptance and event rate yields the total expected DM events. Using profile likelihood fitting based on the final candidates from the experiment together with the predicted background, we set the limit for the DM events and convert it into the limit for the cross section at any mass.

4.7.1 Background and signal modeling

The background consists of three main parts: accidental, ER and neutron background. The accidental background from a random coincidence of isolated $S1$ and $S2$ is estimated random trigger runs. The spectrum of isolated $S1$s and $S2$s are used to generate PDFs.

The detector response nuclear recoil events are calibrated using data from an AmBe source. Custom software is developed based on Geant4 for MC simulation on the distribution of NR and ER events. This simulation began with the detector field configuration and then proceeded to the photon or electron productions and fluctuations based on the Noble Element Simulation Technique (NEST) framework

[80]. It also incorporated the measured S1 and S2 spatial non-uniformity, double PE emissions, ZLE efficiency, and the requirement on the number of fired PMTs be greater than three. A tuning on a single parameter $\alpha = N_{\rm ex}/N_{\rm i}$, the ratio of the initial excitation to ionization, was performed in the NEST model, to match the 2D distribution in ($S1$, $S2$) between AmBe data and simulation of NR events. The NR detection efficiency was then obtained by comparing the data and the simulation.

We exploited the injection of tritiated methane, a technique pioneered by LUX collaboration [109], for the ER calibration. The distribution of 7500 low energy ER events in $\log_{10}(S2/S1)$ vs. $S1$ is shown in Fig 4.52, with AmBe events overlaid. A tuning on α and a recombination fluctuation parameter for ER was performed on the NEST-based simulation, to match the median and width of the tritium band. The ER detection efficiency was then extracted which in agreement with that for NR.

The tuned NR response model and its detection efficiency were used to create the probability density functions (PDFs) for DM signals as well as the neutron background. The tuned NEST-based ER model was used to produce ER background PDFs for ^{127}Xe, tritium, and others (^{85}Kr, radon, and detector instrumental γ) as shown in Fig 4.53.

The recoil energy spectra for different dark matter masses are employed in the simulation. Charge cuts of the search window and detection efficiencies are applied to calculate the acceptance curve in Fig 4.54.

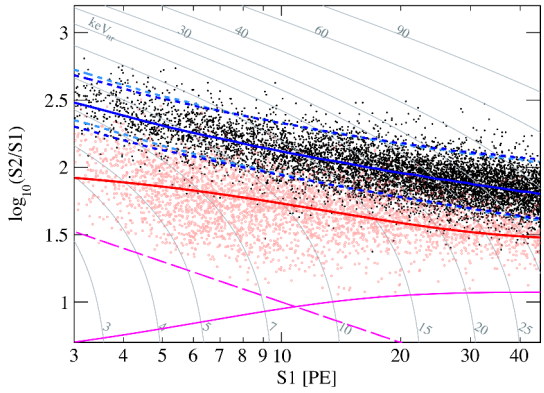

Figure 4.52: Tritium (solid black dots) and AmBe data (open red circles) in $\log_{10}(S2/S1)$ vs. $S1$. For comparison, the median (Run9 and 10 averaged, solid blue), 10% quantile, and 90% quantile (Run9, dashed blue, Run10, light dashed blue) of the ER background PDFs are overlaid. The solid red line is the median of the AmBe events. The dashed and solid magenta curves are the 100 PE selection cut for $S2$, and the 99.99% NR acceptance curve from the MC calculation, respectively. The gray curves represent the equal energy curves in nuclear recoil energy (keVnr).

4.7.2 Final candidate events in Run10

After applying the FV and energy range cut, from 3 to 45 PE for $S1$, from 100 (raw) to 10,000 PE for $S2$, there are 177 final candidate events. The distribution of $\log_{10}$(S2/S1) vs. $S1$ of these events is shown in Fig 4.55.

4.7.3 Profile likelihood fitting

We constructed an un-binned likelihood function as

$$\begin{aligned}\mathcal{L}_{\text{pandax}} = \quad & \text{Poiss}(N_{\text{meas}}|N_{\text{fit}}) \times \\ & \prod_{i=1}^{N_{\text{meas}}} \left(\frac{N_{\text{DM}}(1+\delta_{\text{DM}})P_{\text{DM}}(S1^i, S2^i)}{N_{\text{fit}}} + \sum_b \frac{N_b(1+\delta_b)P_b(S1^i, S2^i)}{N_{\text{fit}}} \right) \\ & \times \left[G\left(\delta_{\text{DM}}, \sigma_{\text{DM}}\right) \prod_b G\left(\delta_b, \sigma_b\right) \right].\end{aligned} \tag{4.24}$$

N_{DM} and N_{b} are the numbers of WIMP, and background events with their

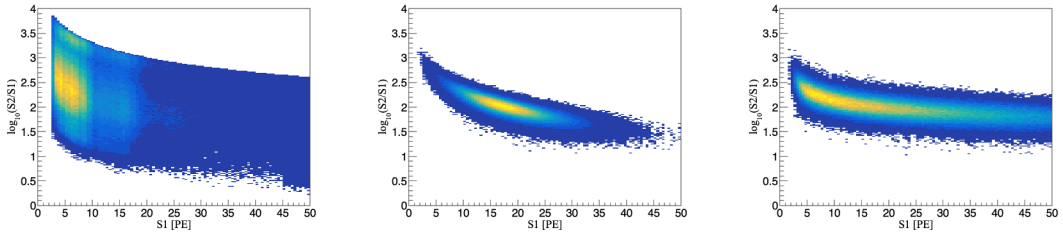

(a) Accidental background (b) 5.2 keV events from ^{127}Xe (c) tritium ER background

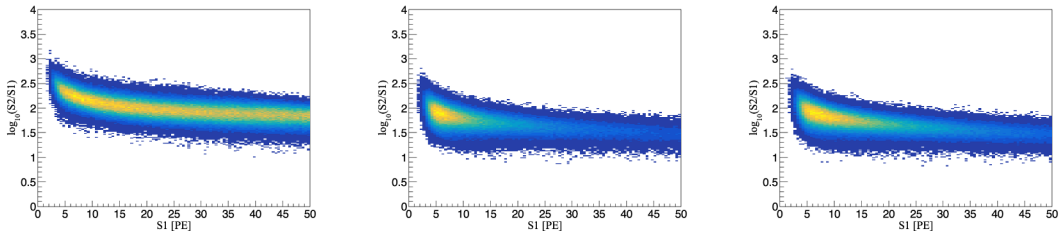

(d) Other ER background (e) neutron background (f) 1 TeV DM

Figure 4.53: The PDFs of ER background from accidental (a), ^{127}Xe (b), tritium (c) and other sources with relatively flat spectrum in low energy region (d) in Run10. The PDFs of neutron background (e), as well as the signal from DM with 1 TeV (f), are shown. All PDFs have taken the detector efficiencies of $S1$ and $S2$ into account.

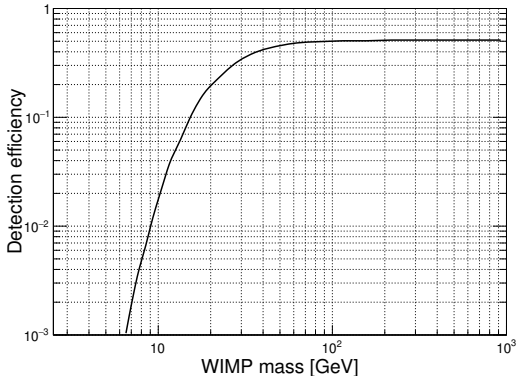

Figure 4.54: The detection efficiency to different WIMP mass in Run10.

corresponding PDFs $P_{\rm DM}(S1, S2)$ and $P_{\rm b}(S1, S2)$. The subscript "b" represents five background components including accidental neutron and three ER sources as shown in Fig 4.53. The δ_b and σ_b are the common nuisance normalization parameters

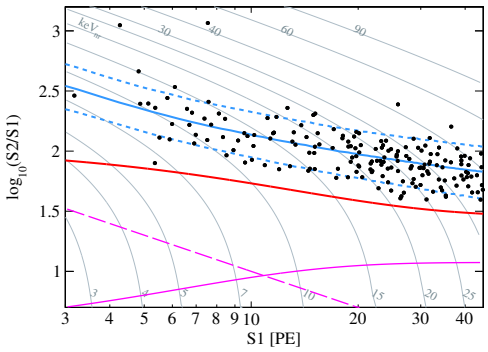

Figure 4.55: The $\log_{10}$(S2/S1) vs. $S1$ distribution of final candidates in the DM search data in Run10, overlaid with the corresponding median, 10% and 90% quantile of the ER background PDFs. The red curve is the NR median from the AmBe calibration.

and fractional systematic uncertainties, respectively, and $G(\delta_b, \sigma_b)$ is the Gaussian penalty term. The CL_s technique [110, 111] can be used to set the exclusion limit on the WIMP-nucleon cross section by considering the background uncertainty.

4.8 Theoretical interpretations of PandaX-II data

In Sep. 2017, we reported the SI WIMP search results using the data with an exposure of 54-ton-day from the PandaX-II experiment. For all WIMP masses between 5 GeV/c^2 and 10 TeV/c^2, the best fit cross section was always zero, and the best fit nuisance parameters were all within 1σ of the nominal values. The test statistic in CL_s was calculated at different WIMP masses and scattering cross sections for the data and compared to those obtained from a large number of toy Monte Carlo calculations produced and fitted using the same signal hypotheses [112]. The final 90% C.L. limit is shown in Fig 4.56, together with limits from PandaX-II 2016 [113], LUX [114], and XENON1T [115]. The strongest limit is set to be

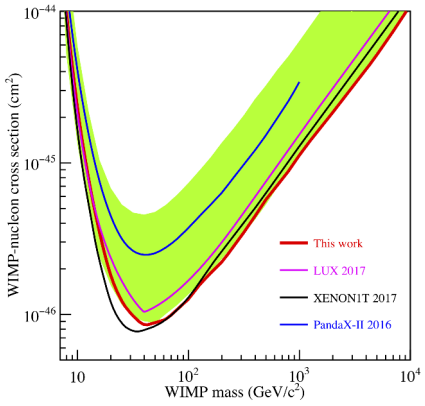

Figure 4.56: The 90% C.L. upper limits versus m_χ between 7 GeV/c^2 and 10 TeV/c^2 for the spin independent WIMP-nucleon elastic cross sections from the combined PandaX-II Run9 and Run10 data (red), overlaid with that from PandaX-II 2016 (blue), LUX 2017 (magenta), and XENON1T 2017 (black). The green band represents the 1σ sensitivity band.

8.6×10^{-47} cm^2 at the WIMP mass of 40 GeV/c^2. This limit is about a factor of 3 more constraining than our previous results [113].

We presented PandaX-II constraints on other theoretical models as well. We searched for nuclear recoil signals for DM models with a light mediator using PandaX-II data with an exposure of 54-ton-day [116]. We applied our results to constrain self-interacting DM models with a light mediator mixing with SM particles and set strong limits on the model parameter space for MD mass ranging from 5 GeV to 10 TeV. We also presented limits on spin-dependent WIMP interactions using PandaX-II data [117, 118]. In addition to standard axial spin-dependent scattering, we considered vector-axial vector interferences, interactions generated by WIMP magnetic and electric dipole moments, and tensor interactions [118]. We reanalyzed PandaX-II data to determine constraints as a function of the WIMP mass and isospin coupling and obtained WIMP-nucleon cross section bounds of 1.6×10^{-41} cm^2 and 9.0×10^{-42} cm^2 for neutron-only spin-dependent and tensor coupling, respec-

tively. PandaX-II has reached a sensitivity sufficient to probe a variety of candidate interactions at the weak scale.

Chapter 5: Summary and outlook

Ample evidence supports the existence of dark matter from astrophysical and cosmological observations. WIMPs are a generic type of DM candidates favored by many theories beyond the Standard Model of particle physics. Many experiments are carried out or under construction to detect DM particle in different approaches, i.e., collider, indirect, and direct searches. WIMP direct detection experiments are designed to detect the nuclear recoil in the scattering of galactic WIMPs off target nuclei. The signal rate depends on the local density and velocity distribution of WIMPs in the Milky Way, the WIMP mass, and the interaction cross section of the target nuclei. In the past decade, the sensitivity of WIMP direct detection experiments using so-called dual-phase xenon time projection chamber technology has improved by four orders of magnitude in a wide range of WIMP mass above 5 GeV/c^2. However, no substantial evidence for their signals is found. This technology allows for a relatively straightforward scaling-up to large monolithic detectors and improvement on the sensitivity. The mass of the detectors has increased by more than 1000 times, and the background levels have been reduced from 0.6 DRU [119] to 0.2 mDRU [120] over the past decade. Experiments using dual-phase xenon TPC technology are preparing their next stage multi-ton detectors. The self-shielding of

liquid xenon will provide a lower background and larger surface-volume ratio for a larger detector after successfully overcoming technical difficulties and suppressing intrinsic backgrounds. The experiments searching for lighter WIMPs in the range of a few GeV/c^2 using different detection technologies are lowering their threshold and increasing their exposure. In the next decade or so, these experiments will push the sensitivity in spin-independent WIMP-nucleon interaction to the irreducible neutrino background and scan an ample parameter space predicted by theoretical models. New technology is needed to suppress the neutrino background while remaining the sensitivity like directional detection.

On the other hand, physicists are exploring other dark matter candidates like Axion and the sterile neutrino. However, no positive signals have shown up so far. Numbers of experiments are planning to improve their sensitivity for these candidates.

In this dissertation, I described the PandaX-II experiment, one of the representative experiments using the dual-phase xenon TPC for DM direct detection. PandaX project since 2012 has been gone through two generations of detectors. PandaX-II is the first ton-scale xenon DM detector and achieved the lowest background level of 0.8×10^{-3} event/kg/day/keV at the time. Compared to other dual-phase xenon detectors, we drift electrons by applying bias voltages on the electrodes which producing a stronger uniform electric field at a strength about 400 V/cm. After running for more than three years, more than 97% of PMTs perform stably. PandaX-II has produced leading limits on dark matter-nucleon spin-independent and spin-dependent scattering cross sections in 2016 and 2017. I outlined the re-

sult of the WIMP-nucleon SI cross section with a 54-ton-day exposure data from PandaX-II which achieved a minimum limit as 8.6×10^{-47} cm^2 at the WIMP mass of 40 GeV/c^2. Theoretical interpretations of PandaX-II data in terms of various DM models have also been presented.

PandaX collaboration is going forward in preparation for the next stage experiment, PandaX-4T. The design of the PandaX-4T experiment is briefly described in [121]. PandaX-4T will be hosted at B-2 Hall in CJPL-II. The collaboration is working on the infrastructure and the development of subsystems. PandaX-4T TPC will feature a cylindrical shape with 1.2 m in both diameter and height which contains in total of 6 t xenon with a sensitive target of 4 t. The schematic diagrams of the PandaX-4T TPC are shown in Fig 5.1(a). The goal of PandaX-4T is to reach a sensitivity of 1×10^{-47}cm^2 with less than 2 background events in a two-year exposure [121].

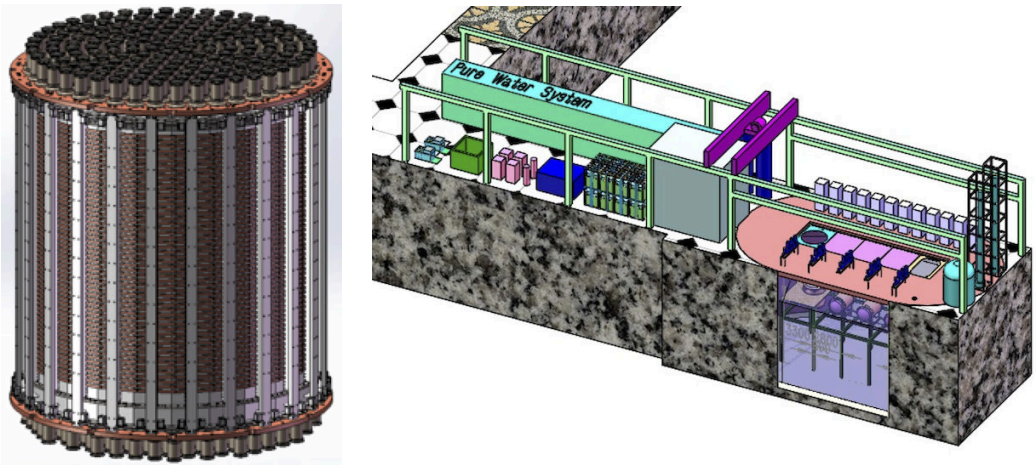

(a) (b)

Figure 5.1: A diagram for PandaX-4T TPC (a) and preliminary layout of the PandaX-4T experiment in Hall-B (b).

The race of building the most sensitive detector searching for WIMPs is getting more competitive. XENON collaboration is constructing their next multi-tone experiment, XENONnT, which expected to commission in late 2019. LUX-ZEPLIN (LZ) collaboration is building a detector with about 10 tons of LXe in total which scheduled to start in 2020. These experiments, along with PandaX-4T, all have similar time scale and sensitivity projections.

Tab 5.1 summarizes the scale and limits of generations of dual-phase xenon TPC experiments.

Table 5.1: The evolution of the minimum limits on the WIMP-nucleon SI cross section of dual-phase xenon TPC experiments and the goal of next-generation multi-ton experiments.

Detector	Year	Target Mass (kg)	Limit (cm^2)
XENON10	2008	14	4.5×10^{-44}
ZEPLIN-III	2011	12	3.9×10^{-44}
XENON100	2012	62	2.0×10^{-45}
PandaX-I	2014	120	1.0×10^{-44}
LUX	2016	370	1.1×10^{-46}
PandaX-II	2016	580	8.6×10^{-47}
XENON1T	2017	2000	4.1×10^{-47}
PandaX-4T	future	~4000	$\sim 6 \times 10^{-48}$
XENONnT	future	~6000	$\sim 10^{-48}$
LZ	future	~7000	$\sim 10^{-48}$

The search for dark matter is far from over. Consistent results for WIMP search from direct, indirect and collider approaches must be achieved for any discovery. With multi-ton experiments, we hope to explore more parameter space of WIMPs predicted by theoretical models in the next decades and answer the questions surrounding dark matter.

Bibliography

[1] F. Zwicky. Die Rotverschiebung von extragalaktischen Nebeln. *Helvetica Physica Acta*, 6:110–127, 1933.

[2] Y Akrami, F Arroja, M Ashdown, J Aumont, C Baccigalupi, M Ballardini, AJ Banday, RB Barreiro, N Bartolo, S Basak, et al. Planck 2018 results. i. overview and the cosmological legacy of planck. *arXiv preprint arXiv:1807.06205*, 2018.

[3] Gianfranco Bertone and Dan Hooper. History of dark matter. *Rev. Mod. Phys.*, 90:045002, Oct 2018.

[4] Yang Huang, X-W Liu, H-B Yuan, M-S Xiang, H-W Zhang, B-Q Chen, J-J Ren, Chun Wang, Yong Zhang, Y-H Hou, et al. The milky way's rotation curve out to 100 kpc and its constraint on the galactic mass distribution. *Monthly Notices of the Royal Astronomical Society*, 463(3):2623–2639, 2016.

[5] A. H. Broeils, K. G. Begeman, and R. H. Sanders. Extended rotation curves of spiral galaxies: dark haloes and modified dynamics. *Monthly Notices of the Royal Astronomical Society*, 249(3):523–537, 04 1991.

[6] John A Peacock, Shaun Cole, Peder Norberg, Carlton M Baugh, Joss Bland-Hawthorn, Terry Bridges, Russell D Cannon, Matthew Colless, Chris Collins, Warrick Couch, et al. A measurement of the cosmological mass density from clustering in the 2df galaxy redshift survey. *Nature*, 410(6825):169, 2001.

[7] *From quantum foam to galaxies: formation of the large-scale structure in the Universe*. `http://cosmicweb.uchicago.edu/index.html`.

[8] W. Tucker, P. Blanco, S. Rappoport, L. David, D. Fabricant, E. E. Falco, W. Forman, A. Dressler, and M. Ramella. 1e 0657-56: A contender for the hottest known cluster of galaxies. *The Astrophysical Journal*, 496(1):L5–L8, mar 1998.

[9] Douglas Clowe, Anthony Gonzalez, and Maxim Markevitch. Weak-lensing mass reconstruction of the interacting cluster 1e 0657-558: Direct evidence for the existence of dark matter. *The Astrophysical Journal*, 604(2):596–603, apr 2004.

[10] M. Markevitch, A. H. Gonzalez, D. Clowe, A. Vikhlinin, W. Forman, C. Jones, S. Murray, and W. Tucker. Direct constraints on the dark matter self-interaction cross section from the merging galaxy cluster 1e 0657-56. *The Astrophysical Journal*, 606(2):819–824, may 2004.

[11] N Aghanim, Y Akrami, M Ashdown, J Aumont, C Baccigalupi, M Ballardini, AJ Banday, RB Barreiro, N Bartolo, S Basak, et al. Planck 2018 results. vi. cosmological parameters. *arXiv preprint arXiv:1807.06209*, 2018.

[12] Scott Dodelson and Lawrence M Widrow. Sterile neutrinos as dark matter. *Physical Review Letters*, 72(1):17, 1994.

[13] AA Aguilar-Arevalo, BC Brown, L Bugel, G Cheng, JM Conrad, RL Cooper, R Dharmapalan, A Diaz, Z Djurcic, DA Finley, et al. Significant excess of electronlike events in the miniboone short-baseline neutrino experiment. *Physical review letters*, 121(22):221801, 2018.

[14] A. Aguilar, L. B. Auerbach, R. L. Burman, D. O. Caldwell, E. D. Church, A. K. Cochran, J. B. Donahue, A. Fazely, G. T. Garvey, R. M. Gunasingha, R. Imlay, W. C. Louis, R. Majkic, A. Malik, W. Metcalf, G. B. Mills, V. Sandberg, D. Smith, I. Stancu, M. Sung, R. Tayloe, G. J. VanDalen, W. Vernon, N. Wadia, D. H. White, and S. Yellin. Evidence for neutrino oscillations from the observation of $\overline{\nu}_e$ appearance in a $\overline{\nu}_\mu$ beam. *Phys. Rev. D*, 64:112007, Nov 2001.

[15] Alexey Boyarsky, M Drewes, T Lasserre, S Mertens, and O Ruchayskiy. Sterile neutrino dark matter. *Progress in Particle and Nuclear Physics*, 2018.

[16] Steven Weinberg. A new light boson? *Phys. Rev. Lett.*, 40:223–226, Jan 1978.

[17] F. Wilczek. Problem of strong p and t invariance in the presence of instantons. *Phys. Rev. Lett.*, 40:279–282, Jan 1978.

[18] R. D. Peccei and Helen R. Quinn. CP conservation in the presence of pseudoparticles. *Phys. Rev. Lett.*, 38:1440–1443, Jun 1977.

[19] Leanne D Duffy and Karl van Bibber. Axions as dark matter particles. *New Journal of Physics*, 11(10):105008, oct 2009.

[20] P. SIKIVIE. Dark matter axions. *International Journal of Modern Physics A*, 25(02n03):554–563, 2010.

[21] David JE Marsh. Axion cosmology. *Physics Reports*, 643:1–79, 2016.

[22] N Du, N Force, R Khatiwada, E Lentz, R Ottens, LJ Rosenberg, Gray Rybka, G Carosi, N Woollett, D Bowring, et al. Search for invisible axion dark matter with the axion dark matter experiment. *Physical review letters*, 120(15):151301, 2018.

[23] V Anastassopoulos, S Aune, K Barth, A Belov, H Bräuninger, Giovanni Cantatore, JM Carmona, JF Castel, SA Cetin, F Christensen, et al. New cast limit on the axion–photon interaction. *Nature Physics*, 13(6):584, 2017.

[24] Z Ahmed, DS Akerib, S Arrenberg, CN Bailey, D Balakishiyeva, L Baudis, DA Bauer, J Beaty, PL Brink, T Bruch, et al. Search for axions with the cdms experiment. *Physical review letters*, 103(14):141802, 2009.

[25] K Abe, K Hieda, K Hiraide, S Hirano, Y Kishimoto, K Kobayashi, S Moriyama, K Nakagawa, M Nakahata, H Ogawa, et al. Search for solar axions in xmass, a large liquid-xenon detector. *Physics Letters B*, 724(1-3):46–50, 2013.

[26] E Aprile, F Agostini, M Alfonsi, K Arisaka, F Arneodo, M Auger, C Balan, P Barrow, L Baudis, B Bauermeister, et al. First axion results from the xenon100 experiment. *Physical Review D*, 90(6):062009, 2014.

[27] SK Liu, Q Yue, KJ Kang, JP Cheng, HT Wong, YJ Li, HB Li, ST Lin, JP Chang, JH Chen, et al. Constraints on axion couplings from the cdex-1 experiment at the china jinping underground laboratory. *Physical Review D*, 95(5):052006, 2017.

[28] DS Akerib, S Alsum, C Aquino, HM Araújo, X Bai, AJ Bailey, J Balajthy, P Beltrame, EP Bernard, A Bernstein, et al. First searches for axions and axionlike particles with the lux experiment. *Physical review letters*, 118(26):261301, 2017.

[29] Changbo Fu, Xiaopeng Zhou, Xun Chen, Yunhua Chen, Xiangyi Cui, Deqing Fang, Karl Giboni, Franco Giuliani, Ke Han, Xingtao Huang, et al. Limits on axion couplings from the first 80 days of data of the pandax-ii experiment. *Physical review letters*, 119(18):181806, 2017.

[30] Stephen P Martin. A supersymmetry primer. In *Perspectives on supersymmetry II*, pages 1–153. World Scientific, 2010.

[31] Geraldine Servant and Tim MP Tait. Is the lightest kaluza–klein particle a viable dark matter candidate? *Nuclear Physics B*, 650(1-2):391–419, 2003.

[32] Andreas Birkedal, Andrew Noble, Maxim Perelstein, and Andrew Spray. Little higgs dark matter. *Physical Review D*, 74(3):035002, 2006.

[33] Gerard Jungman, Marc Kamionkowski, and Kim Griest. Supersymmetric dark matter. *Physics Reports*, 267(5-6):195–373, 1996.

[34] Jonathan L Feng. Dark matter candidates from particle physics and methods of detection. *Annual Review of Astronomy and Astrophysics*, 48:495–545, 2010.

[35] Bing-Lin Young. A survey of dark matter and related topics in cosmology. *Frontiers of Physics*, 12(2):121201, 2017.

[36] M. A. Deliyergiyev. Recent Progress in Search for Dark Sector Signatures. *Open Phys.*, 14(1):281–303, 2016.

[37] Morad Aaboud, Georges Aad, Brad Abbott, Ovsat Abdinov, Baptiste Abeloos, SH Abidi, OS AbouZeid, NL Abraham, Halina Abramowicz, Henso Abreu, et al. Search for dark matter in association with a higgs boson decaying to two photons at s= 13 tev with the atlas detector. *Physical Review D*, 96(11):112004, 2017.

[38] *Dark Matter Summary Plots from CMS for LHCP and EPS 2017*, 2017. `https://twiki.cern.ch/twiki/pub/CMSPublic/PhysicsResultsEXO/DM-summary-plots-Jul17.pdf`.

[39] Julio F. Navarro, Carlos S. Frenk, and Simon D. M. White. A universal density profile from hierarchical clustering. *The Astrophysical Journal*, 490(2):493–508, dec 1997.

[40] Jaan Einasto. On the construction of a composite model for the galaxy and on the determination of the system of galactic parameters. *Trudy Astrofizicheskogo Instituta Alma-Ata*, 5:87–100, 1965.

[41] B Holl, M Audard, K Nienartowicz, G Jevardat de Fombelle, O Marchal, N Mowlavi, G Clementini, Joris De Ridder, DW Evans, LP Guy, et al. Gaia data release 2-summary of the variability processing and analysis results. *Astronomy & Astrophysics*, 618:A30, 2018.

[42] O Adriani, GC Barbarino, GA Bazilevskaya, R Bellotti, M Boezio, EA Bogomolov, M Bongi, V Bonvicini, S Bottai, A Bruno, et al. Time dependence of the electron and positron components of the cosmic radiation measured by the pamela experiment between july 2006 and december 2015. *Physical review letters*, 116(24):241105, 2016.

[43] G Ambrosi, Q An, R Asfandiyarov, P Azzarello, P Bernardini, B Bertucci, MS Cai, J Chang, DY Chen, HF Chen, et al. Direct detection of a break in the teraelectronvolt cosmic-ray spectrum of electrons and positrons. *Nature*, 552(7683):63, 2017.

[44] M Aguilar, D Aisa, A Alvino, G Ambrosi, K Andeen, L Arruda, N Attig, P Azzarello, A Bachlechner, F Barao, et al. Electron and positron fluxes in primary cosmic rays measured with the alpha magnetic spectrometer on the international space station. *Physical review letters*, 113(12):121102, 2014.

[45] M Aguilar, D Aisa, B Alpat, A Alvino, G Ambrosi, K Andeen, L Arruda, N Attig, P Azzarello, A Bachlechner, et al. Precision measurement of the proton flux in primary cosmic rays from rigidity 1 gv to 1.8 tv with the alpha magnetic spectrometer on the international space station. *Physical Review Letters*, 114(17):171103, 2015.

[46] M Aguilar, L Ali Cavasonza, B Alpat, G Ambrosi, L Arruda, N Attig, S Aupetit, P Azzarello, A Bachlechner, F Barao, et al. Antiproton flux, antiproton-to-proton flux ratio, and properties of elementary particle fluxes in primary cosmic rays measured with the alpha magnetic spectrometer on the international space station. *Physical review letters*, 117(9):091103, 2016.

[47] M Ackermann, A Albert, Brandon Anderson, WB Atwood, Luca Baldini, G Barbiellini, D Bastieri, K Bechtol, R Bellazzini, E Bissaldi, et al. Searching for dark matter annihilation from milky way dwarf spheroidal galaxies with six years of fermi large area telescope data. *Physical Review Letters*, 115(23):231301, 2015.

[48] H Abdallah, A Abramowski, F Aharonian, F Ait Benkhali, AG Akhperjanian, E Angüner, M Arrieta, P Aubert, M Backes, A Balzer, et al. Search for dark matter annihilations towards the inner galactic halo from 10 years of observations with hess. *Physical review letters*, 117(11):111301, 2016.

[49] B Bartoli, P Bernardini, XJ Bi, Z Cao, S Catalanotti, SZ Chen, TL Chen, SW Cui, BZ Dai, A D'Amone, et al. Search for gamma-ray emission from the sun during solar minimum with the argo-ybj experiment. *arXiv preprint arXiv:1901.04201*, 2019.

[50] Maryon Ahrens, Christian Bohm, Jonathan P Dumm, Chad Finley, Samuel Flis, Klas Hultqvist, Erin O'Sullivan, and Christian Walck. Search for neutrinos from decaying dark matter with icecube: Icecube collaboration. *European Physical Journal C*, 78(10), 2018.

[51] Pei-Hong Gu and Xiao-Gang He. Electrophilic dark matter with dark photon: From dampe to direct detection. *Physics Letters B*, 778:292 – 295, 2018.

[52] Andrew Fowlie. Dampe squib? significance of the 1.4 tev dampe excess. *Physics Letters B*, 780:181 – 184, 2018.

[53] Alessandro Cuoco, Michael Krämer, and Michael Korsmeier. Novel dark matter constraints from antiprotons in light of ams-02. *Phys. Rev. Lett.*, 118:191102, May 2017.

[54] Ming-Yang Cui, Qiang Yuan, Yue-Lin Sming Tsai, and Yi-Zhong Fan. Possible dark matter annihilation signal in the ams-02 antiproton data. *Phys. Rev. Lett.*, 118:191101, May 2017.

[55] M Aguilar, L Ali Cavasonza, G Ambrosi, L Arruda, N Attig, P Azzarello, A Bachlechner, F Barao, A Barrau, L Barrin, et al. Towards understanding the origin of cosmic-ray positrons. *Physical Review Letters*, 122(4):041102, 2019.

[56] S. Ting. *The AMS Experiment, talk given at the AMS Day at CERN*, Apr 2015. `https://indico.cern.ch/event/381134/contributions/900588/attachments/759341/1041607/Ting_2015_April_AMS_DaysCERN.pdf`.

[57] JD Lewin and PF Smith. Review of mathematics, numerical factors, and corrections for dark matter experiments based on elastic nuclear recoil. *Astroparticle Physics*, 6(1):87–112, 1996.

[58] Teresa Marrodán Undagoitia and Ludwig Rauch. Dark matter direct-detection experiments. *Journal of Physics G: Nuclear and Particle Physics*, 43(1):013001, dec 2015.

[59] Bing-Lin Young. A survey of dark matter and related topics in cosmology. *Frontiers of Physics*, 12(2):121201, Oct 2016.

[60] Mark W. Goodman and Edward Witten. Detectability of certain dark-matter candidates. *Phys. Rev. D*, 31:3059–3063, Jun 1985.

[61] Yonit Hochberg, Yue Zhao, and Kathryn M. Zurek. Superconducting detectors for superlight dark matter. *Phys. Rev. Lett.*, 116:011301, Jan 2016.

[62] F. J. Kerr and D. Lynden-Bell. Review of galactic constants. *Monthly Notices of the Royal Astronomical Society*, 221(4):1023–1038, 08 1986.

[63] MT Ressell and DJ Dean. Spin-dependent neutralino-nucleus scattering for a 127 nuclei. *Physical Review C*, 56(1):535, 1997.

[64] P Toivanen, M Kortelainen, J Suhonen, and J Toivanen. Large-scale shell-model calculations of elastic and inelastic scattering rates of lightest supersymmetric particles (lsp) on i 127, xe 129, xe 131, and cs 133 nuclei. *Physical Review C*, 79(4):044302, 2009.

[65] Ciaran A. J. O'Hare. Dark matter astrophysical uncertainties and the neutrino floor. *Phys. Rev. D*, 94:063527, Sep 2016.

[66] Philipp Grothaus, Malcolm Fairbairn, and Jocelyn Monroe. Directional dark matter detection beyond the neutrino bound. *Phys. Rev. D*, 90:055018, Sep 2014.

[67] E Aprile and T Doke. Liquid xenon detectors for particle physics and astrophysics. *Reviews of Modern Physics*, 82(3):2053, 2010.

[68] James William Rohlf. Modern physics from aalpha to z0. *Modern Physics from aalpha to Z0, by James William Rohlf, pp. 664. ISBN 0-471-57270-5. Wiley-VCH, March 1994.*, page 664, 1994.

[69] *National Nuclear Data Center, information extracted from the NuDat 2 database*. http://www.nndc.bnl.gov/nudat2/.

[70] L. Baudis, G. Kessler, P. Klos, R. F. Lang, J. Menéndez, S. Reichard, and A. Schwenk. Signatures of dark matter scattering inelastically off nuclei. *Phys. Rev. D*, 88:115014, Dec 2013.

[71] Tadayoshi Doke, Akira Hitachi, Jun Kikuchi, Kimiaki Masuda, Hiroyuki Okada, and Eido Shibamura. Absolute scintillation yields in liquid argon and xenon for various particles. *Japanese Journal of Applied Physics*, 41(Part 1, No. 3A):1538–1545, mar 2002.

[72] Akira Hitachi. Properties of liquid xenon scintillation for dark matter searches. *Astroparticle Physics*, 24(3):247 – 256, 2005.

[73] Elena Aprile, Alexander I Bolozdynya, Aleksey E Bolotnikov, and Tadayoshi Doke. *Noble gas detectors*. John Wiley & Sons, 2006.

[74] R. E. Huffman, J. C. Larrabee, and Y. Tanaka. Rare gas continuum light sources for photoelectric scanning in the vacuum ultraviolet. *Appl. Opt.*, 4(12):1581–1588, Dec 1965.

[75] A. Lyashenko, T. Nguyen, A. Snyder, H. Wang, and K. Arisaka. Measurement of the absolute quantum efficiency of hamamatsu model r11410-10 photomultiplier tubes at low temperatures down to liquid xenon boiling point. *Journal of Instrumentation*, 9(11):P11021–P11021, nov 2014.

[76] *SAES Pure Gas, Inc.* http://www.saespuregas.com/Products/Gas-Purifier/PS4-MT50.html.

[77] JB Albert, M Auger, DJ Auty, PS Barbeau, E Beauchamp, D Beck, V Belov, C Benitez-Medina, J Bonatt, M Breidenbach, et al. Improved measurement of the $2\nu\beta\beta$ half-life of ^{136}xe with the exo-200 detector. *Physical Review C*, 89(1):015502, 2014.

[78] MJ Berger, JH Hubbell, SM Seltzer, J Chang, JS Coursey, R Sukumar, DS Zucker, and K Olsen. Xcom: Photon cross sections database, nist standard reference database 8 (xgam). *URL http://physics. nist. gov/PhysRefData/Xcom/Text/XCOM. html*, 2010.

[79] David R. Nygren. Origin and development of the tpc idea. *Nuclear Instruments and Methods in Physics Research Section A: Accelerators, Spectrometers, Detectors and Associated Equipment*, 907:22 – 30, 2018. Advances in Instrumentation and Experimental Methods (Special Issue in Honour of Kai Siegbahn).

[80] M Szydagis, N Barry, K Kazkaz, J Mock, D Stolp, M Sweany, M Tripathi, S Uvarov, N Walsh, and M Woods. NEST: a comprehensive model for scintillation yield in liquid xenon. *Journal of Instrumentation*, 6(10):P10002–P10002, oct 2011.

[81] Kaixuan Ni. *Development of a Liquid Xenon Time Projection Chamber for the XENON Dark Matter Search*. PhD thesis, Columbia U. (main), 2006.

[82] Elena Aprile, CE Dahl, L De Viveiros, RJ Gaitskell, Karl-Ludwig Giboni, J Kwong, P Majewski, Kaixuan Ni, T Shutt, and M Yamashita. Simultaneous measurement of ionization and scintillation from nuclear recoils in liquid xenon for a dark matter experiment. *Physical review letters*, 97(8):081302, 2006.

[83] Wu Yu-Cheng, Hao Xi-Qing, Yue Qian, Li Yuan-Jing, Cheng Jian-Ping, Kang Ke-Jun, Chen Yun-Hua, Li Jin, Li Jian-Min, Li Yu-Lan, et al. Measurement of cosmic ray flux in the china jinping underground laboratory. *Chinese physics C*, 37(8):086001, 2013.

[84] Aldo Ianni. Review of technical features in underground laboratories. *International Journal of Modern Physics A*, 32(30):1743001, 2017.

[85] N. W. Xu, T. B. Li, F. Dai, R. Zhang, C. A. Tang, and L. X. Tang. Microseismic monitoring of strainburst activities in deep tunnels at the jinping ii hydropower station, china. *Rock Mechanics and Rock Engineering*, 49(3):981–1000, Mar 2016.

[86] Xia-Ting Feng, Chuanqing Zhang, Shili Qiu, Hui Zhou, Quan Jiang, and Shaojun Li. Dynamic design method for deep hard rock tunnels and its application. *Journal of Rock Mechanics and Geotechnical Engineering*, 8(4):443 – 461, 2016.

[87] Ke-Jun Kang, Jian-Ping Cheng, Jin Li, Yuan-Jing Li, Qian Yue, Yang Bai, Yong Bi, Jian-Ping Chang, Nan Chen, Ning Chen, et al. Introduction to the cdex experiment. *Frontiers of Physics*, 8(4):412–437, 2013.

[88] XiGuang Cao, Xun Chen, YunHua Chen, XiangYi Cui, DeQing Fang, ChangBo Fu, Karl L Giboni, HaoWei Gong, GuoDong Guo, Ming He, et al. Pandax: a liquid xenon dark matter experiment at cjpl. *Science China Physics, Mechanics & Astronomy*, 57(8):1476–1494, 2014.

[89] John F Beacom, Shaomin Chen, Jianping Cheng, Sayed N Doustimotlagh, Yuanning Gao, Shao-Feng Ge, Guanghua Gong, Hui Gong, Lei Guo, Ran Han, et al. Letter of intent: Jinping neutrino experiment. *arXiv preprint arXiv:1602.01733*, 2016.

[90] Jianmin Li, Xiangdong Ji, Wick Haxton, and Joseph S.Y. Wang. The second-phase development of the china jinping underground laboratory. *Physics Procedia*, 61:576 – 585, 2015. 13th International Conference on Topics in Astroparticle and Underground Physics, TAUP 2013.

[91] Jian-Ping Cheng et al. The China Jinping Underground Laboratory and its Early Science. *Ann. Rev. Nucl. Part. Sci.*, 67:231–251, 2017.

[92] Zhi Zeng, Jian Su, Hao Ma, Hengguan Yi, Jianping Cheng, Qian Yue, Junli Li, and Hui Zhang. Environmental gamma background measurements in china jinping underground laboratory. *Journal of Radioanalytical and Nuclear Chemistry*, 301(2):443–450, Aug 2014.

[93] Z.M. Zeng, H. Gong, Q. Yue, and J.M. Li. Thermal neutron background measurement in cjpl. *Nuclear Instruments and Methods in Physics Research Section A: Accelerators, Spectrometers, Detectors and Associated Equipment*, 804:108 – 112, 2015.

[94] Qingdong Hu, Hao Ma, Zhi Zeng, Jianping Cheng, Yunhua Chen, Shengming He, Junli Li, Manbin Shen, Shiyong Wu, Qian Yue, Jianfeng Yue, and Hui Zhang. Neutron background measurements at china jinping underground laboratory with a bonner multi-sphere spectrometer. *Nuclear Instruments and Methods in Physics Research Section A: Accelerators, Spectrometers, Detectors and Associated Equipment*, 859:37 – 40, 2017.

[95] Q. Du, S.T. Lin, S.K. Liu, C.J. Tang, L. Wang, W.W. Wei, H.T. Wong, H.Y. Xing, Q. Yue, and J.J. Zhu. Measurement of the fast neutron background at the china jinping underground laboratory. *Nuclear Instruments and Methods in Physics Research Section A: Accelerators, Spectrometers, Detectors and Associated Equipment*, 889:105 – 112, 2018.

[96] Mengjiao Xiao. *PandaX-I Experiment for Low-mass Dark Matter Search*. PhD thesis, Shanghai Jiao Tong University, Shanghai, P. R. China, June 2016. `https://static.pandax.sjtu.edu.cn/download/thesis/2016_xiaomengjiao.pdf`.

[97] H Gong, Karl Ludwig Giboni, X Ji, A Tan, and L Zhao. The cryogenic system for the panda-x dark matter search experiment. *Journal of Instrumentation*, 8(01):P01002, 2013.

[98] Haowei Gong. *The PandaX-I Liquid Xenon Dark Matter Direct Detection Experiment: Cryogenic Design, Construction and Experimental Data Analysis*. PhD thesis, Shanghai Jiao Tong University, Shanghai, P. R. China, September 2015. `https://static.pandax.sjtu.edu.cn/download/thesis/2016_gonghaowei.pdf`.

[99] Tao Zhang, Changbo Fu, Xiangdong Ji, Jianglai Liu, Xiang Liu, Xuming Wang, Chunfa Yao, and Xunhua Yuan. Low background stainless steel for the pressure vessel in the pandax-ii dark matter experiment. *Journal of Instrumentation*, 11(09):T09004, 2016.

[100] Shaoli Li, Xun Chen, Karl L Giboni, Guodong Guo, Xiangdong Ji, Qing Lin, Jianglai Liu, Yajun Mao, Kaixuan Ni, Xiangxiang Ren, et al. Performance of photosensors in the pandax-i experiment. *Journal of Instrumentation*, 11(02):T02005, 2016.

[101] `http://www.caen.it/servlet/checkCaenManualFile?Id=12364`.

[102] C. H. Faham, V. M. Gehman, A. Currie, A. Dobi, P. Sorensen, and R. J. Gaitskell. Measurements of wavelength-dependent double photoelectron emission from single photons in VUV-sensitive photomultiplier tubes. *JINST*, 10(09):P09010, 2015.

[103] VN Solovov, VA Belov, D Yu Akimov, HM Araujo, EJ Barnes, AA Burenkov, V Chepel, A Currie, L DeViveiros, B Edwards, et al. Position reconstruction in a dual phase xenon scintillation detector. *IEEE Transactions on Nuclear Science*, 59(6):3286–3293, 2012.

[104] DS Akerib, S Alsum, HM Araújo, X Bai, AJ Bailey, J Balajthy, P Beltrame, EP Bernard, A Bernstein, TP Biesiadzinski, et al. Ultralow energy calibration of lux detector using xe 127 electron capture. *Physical Review D*, 96(11):112011, 2017.

[105] DS Akerib, S Alsum, HM Araújo, X Bai, AJ Bailey, J Balajthy, P Beltrame, EP Bernard, A Bernstein, TP Biesiadzinski, et al. 3d modeling of electric fields in the LUX detector. *Journal of Instrumentation*, 12(11):P11022–P11022, nov 2017.

[106] A. Dobi, C. Davis, C. Hall, T. Langford, S. Slutsky, and Y.-R. Yen. Detection of krypton in xenon for dark matter applications. *Nuclear Instruments and Methods in Physics Research Section A: Accelerators, Spectrometers, Detectors and Associated Equipment*, 665:1 – 6, 2011.

[107] M.B. Chadwick, M. Herman, P. Obložinský, et al. ENDF/B-VII.1 nuclear data for science and technology: Cross sections, covariances, fission product yields and decay data. *Nuclear Data Sheets*, 112(12):2887 – 2996, 2011. Special Issue on ENDF/B-VII.1 Library.

[108] JB Albert, DJ Auty, PS Barbeau, D Beck, V Belov, M Breidenbach, T Brunner, A Burenkov, GF Cao, C Chambers, et al. Measurements of the ion fraction and mobility of α- and β-decay products in liquid xenon using the exo-200 detector. *Physical Review C*, 92(4):045504, 2015.

[109] DS Akerib, HM Araújo, X Bai, AJ Bailey, J Balajthy, P Beltrame, EP Bernard, A Bernstein, TP Biesiadzinski, EM Boulton, et al. Tritium calibration of the lux dark matter experiment. *Physical Review D*, 93(7):072009, 2016.

[110] Thomas Junk. Confidence level computation for combining searches with small statistics. *Nuclear Instruments and Methods in Physics Research Section A: Accelerators, Spectrometers, Detectors and Associated Equipment*, 434(2-3):435–443, 1999.

[111] Alexander L Read. Presentation of search results: the cls technique. *Journal of Physics G: Nuclear and Particle Physics*, 28(10):2693, 2002.

[112] Gary J. Feldman and Robert D. Cousins. Unified approach to the classical statistical analysis of small signals. *Phys. Rev. D*, 57:3873–3889, Apr 1998.

[113] Andi Tan, Mengjiao Xiao, Xiangyi Cui, Xun Chen, Yunhua Chen, Deqing Fang, Changbo Fu, Karl Giboni, Franco Giuliani, Haowei Gong, et al. Dark matter results from first 98.7 days of data from the pandax-ii experiment. *Physical review letters*, 117(12):121303, 2016.

[114] DS Akerib, S Alsum, HM Araújo, X Bai, AJ Bailey, J Balajthy, P Beltrame, EP Bernard, A Bernstein, TP Biesiadzinski, et al. Results from a search for dark matter in the complete lux exposure. *Physical review letters*, 118(2):021303, 2017.

[115] E Aprile, J Aalbers, F Agostini, M Alfonsi, FD Amaro, M Anthony, F Arneodo, P Barrow, L Baudis, Boris Bauermeister, et al. First dark matter search results from the xenon1t experiment. *Physical review letters*, 119(18):181301, 2017.

[116] Xiangxiang Ren, Li Zhao, Abdusalam Abdukerim, Xun Chen, Yunhua Chen, Xiangyi Cui, Deqing Fang, Changbo Fu, Karl Giboni, Franco Giuliani, et al. Constraining dark matter models with a light mediator at the pandax-ii experiment. *Physical review letters*, 121(2):021304, 2018.

[117] Changbo Fu, Xiangyi Cui, Xiaopeng Zhou, Xun Chen, Yunhua Chen, Deqing Fang, Karl Giboni, Franco Giuliani, Ke Han, Xingtao Huang, et al. Spin-dependent weakly-interacting-massive-particle–nucleon cross section limits from first data of pandax-ii experiment. *Physical review letters*, 118(7):071301, 2017.

[118] Jingkai Xia, Abdusalam Abdukerim, Wei Chen, Xun Chen, Yunhua Chen, Xiangyi Cui, Deqing Fang, Changbo Fu, Karl Giboni, Franco Giuliani, et al. Pandax-ii constraints on spin-dependent wimp-nucleon effective interactions. *Physics Letters B*, 2019.

[119] J Angle, E Aprile, F Arneodo, L Baudis, A Bernstein, A Bolozdynya, P Brusov, LCC Coelho, CE Dahl, L DeViveiros, et al. First results from the xenon10 dark matter experiment at the gran sasso national laboratory. *Physical Review Letters*, 100(2):021303, 2008.

[120] XENON Collaboration, E Aprile, J Aalbers, F Agostini, M Alfonsi, L Althueser, FD Amaro, M Anthony, F Arneodo, L Baudis, et al. Dark matter search results from a one ton-year exposure of xenon1t. *Physical review letters*, 121(11):111302, 2018.

[121] HongGuang Zhang, Abdusalam Abdukerim, Wei Chen, Xun Chen, YunHua Chen, XiangYi Cui, BinBin Dong, DeQing Fang, ChangBo Fu, Karl Giboni, et al. Dark matter direct search sensitivity of the pandax-4t experiment. *SCIENCE CHINA Physics, Mechanics & Astronomy*, 62(3):31011, 2019.